Missouri S&T Library and Learning Resources

Scholars' Mine

Doctoral Dissertations | Student Theses and Dissertations

2010

Factors controlling ductility in ultrafine grain aluminum alloys under monotonic and cyclic loading

Partha Sarathi De

Follow this and additional works at: https://scholarsmine.mst.edu/doctoral_dissertations

 Part of the Metallurgy Commons

Department: Materials Science and Engineering

Recommended Citation

De, Partha Sarathi, "Factors controlling ductility in ultrafine grain aluminum alloys under monotonic and cyclic loading" (2010). *Doctoral Dissertations*. 2172.
https://scholarsmine.mst.edu/doctoral_dissertations/2172

This thesis is brought to you by Scholars' Mine, a service of the Missouri S&T Library and Learning Resources. This work is protected by U. S. Copyright Law. Unauthorized use including reproduction for redistribution requires the permission of the copyright holder. For more information, please contact scholarsmine@mst.edu.

FACTORS CONTROLLING DUCTILITY IN ULTRAFINE GRAIN ALUMINUM ALLOYS UNDER MONOTONIC AND CYCLIC LOADING

by

PARTHA SARATHI DE

A DISSERTATION

Presented to the Faculty of the Graduate School of the

MISSOURI UNIVERSITY OF SCIENCE AND TECHNOLOGY

In Partial Fulfillment of the Requirements for the Degree

DOCTOR OF PHILOSOPHY

in

METALLURGICAL ENGINEERING

2010

Approved by:

Rajiv S. Mishra, Advisor

R. Kohser

K. Chandrashekhara

F.S. Miller

K.K. Sankaran

PUBLICATION DISSERTATION OPTION

This dissertation has been prepared in the form of papers for publication. Each paper has been prepared in the style of the journal/proceeding in which it has been published or submitted. Five papers are selected to represent the doctorate work. An "Introduction" section, pages 1-29, is included for presenting a brief background to this dissertation work. Paper I, pages 30-39, has been published in Journal of Testing and Evaluation. Paper-II, pages 40-67, has been prepared for Acta Materialia. Paper III, pages 68-78, has been published in Scripta Materialia. Paper- IV, pages 79-110 has been published in Materials Science and Engineering A. Paper V, pages 111 - 123, has been published in Scripta Materialia.

ABSTRACT

Ultrafine grained (UFG) Al processed by severe plastic deformation (SPD) methods are characterized by high strength and a limited uniform ductility. Friction stir processing (FSP), an offshoot of friction stir welding has emerged as a new technique to produce UFG alloys. FSP-UFG Al alloys show a distinctly different behavior with higher uniform elongation and improved high cycle fatigue life as compared to other SPD processed variants. The objective of this work was to study the microstructural basis for such mechanical behavior in FSP-UFG Al alloys.

To study the mechanical behavior of FSP Al alloys, a subsize bending fatigue and uniaxial tensile test beds were designed. These subsize test systems were validated using commercial alloys for which standard handbook test data are available. A commercial Al-Li alloy in different microstructural conditions was investigated using the subsize fatigue test bed. The results indicated that grain shape, texture, precipitate type and precipitate distribution controlled the high cycle fatigue life.

To understand the mechanical behavior of UFG Al, an Al-Mg-Zn alloy was selected. The subsize high cycle fatigue tests conducted on this alloy show a significant difference in low angle boundary stability compared to their coarse grain counterpart. Key observations on the UFG Al-Mg-Zn alloy include: (a) Fatigue induced room temperature recrystallization. (b) Improved fatigue life at higher stresses (normalized) compared to corresponding coarse grained alloy in T6 condition. (c) Beneficial effect of distributed second phases on fatigue life through enhanced dislocation storage.

Subsize tensile tests conducted on the UFG Al alloy suggests, that dislocation annihilation controls the deformation process. The experimental data indicated that such annihilation mechanisms were active even within the matrix. The role of low angle boundaries with consequent boundary diffusion was found to be significant in this regard. A diffusion based model proposed for UFG Al ductility fits the expected stress-strain trend.

ACKNOWLEDGMENTS

This dissertation would not have been realized without the kind help, support and encouragement from various people. It gives me enormous pleasure to thank them. I would like to thank my advisor, Prof. Rajiv S. Mishra, for guiding me through my research, patiently correcting all my faults, and enabling me to reach the logical conclusion of my studies at Missouri S&T. I would also like to thank Prof. F. S. Miller and Prof. K. Chandrashekhara for their support not only as a committee member but also as a teacher. Without their help, this work may not have been completed. I am ever grateful to all of them for their role in my development.

I would also like to extend my warmest gratitude to my committee members, Prof. R. Kohser and Dr. K.K. Sankaran for their unmitigated help and guidance during my thesis work. My thanks are also due to Jack Jones and Nathaniel Inskip of the Department of Material Science and Engineering for providing me full workshop support during my research work.

It also gives me great pleasure to thank all my friends and colleagues at Missouri S&T. It has not only been a great learning experience, but also an honor to have been part of the Center for Friction Stir Processing.

I would like to dedicate this dissertation to my parents Guru Prasad and Ratna and my sister Bhaswati - they always believed in me and have stood by me throughout my endeavors. This work would not have been possible without their prayers to the Almighty whose benevolence has no bounds and I offer Him my revered salutations.

TABLE OF CONTENTS

Page

LIST OF ILLUSTRATIONS

PAPER I

PAPER II

PAPER V

LIST OF TABLES

1. INTRODUCTION

The role of microstructure on the high cycle fatigue (HCF) and monotonic tensile properties of metals has been the subject of continuing research for the past few decades. Conventionally, most of these research efforts were directed towards single crystal and microcrystalline (MC) metals and alloys (grain size>10 μm) the strengthening theories for which are quite well accepted [1-2]. But, the advent of nanocrystalline and ultrafine grain metals [3] has raised new questions regarding the validity of existing strengthening theories. This has provided a fresh impetus for research in structure property correlation study of nanocrystalline and ultrafine grain metallic materials. Here, the difference between ultrafine and nanocrystalline metals needs a special mention. Conventionally, metals with a grain size in the range of 100 – 1000 nm are classified as ultrafine grain; grain sizes less than 100 nm are considered to be in the nanocrystalline domain.

On the other hand, the influence of processing route on microstructure and property is no less important. For example, consider the tensile property differences between AA2014-T4 extrusions and non-extrusion products (see Table 1.1). A distinct change in yield and ultimate tensile stresses for extrusion and non-extrusion products is apparent. In fact, similar dependence of processing route on ultrafine grain property has also been observed. In the next section the variation in property of UFG Al alloys as a function of its processing route is discussed in more details.

1.1 PROCESSING OF UFG AL ALLOYS

UFG Al synthesis can be broadly divided into four different categories. They are: a) inert gas condensation b) mechanical alloying c) crystallization from amorphous solids and d) severe plastic deformation (SPD). The SPD route again comprises of different processes which includes a) equal channel angular pressing (ECAP) b) high pressure torsion (HPT) c) accumulative roll bonding (ARB) and d) friction stir processing (FSP). Now, UFG Al alloys in general exhibit a combination of high yield/tensile strength and a low uniform ductility. Thus, although the strengths of UFG Al alloys are high their ductility is low compared to their coarse grain

counterparts (Figure 1.1). In fact, this low ductility of UFG alloys has become a hindrance in their practical application.

Table 1.1 Typical tensile properties of AA2014-T4 extrusions and non-extrusion products at different temperatures [4].

Temperature (˚C)		Y.S. (MPa)	T.S. (MPa)	Elongation (%)	G (GPa)
-196	Extrusion	470	585	16	82
	Non-extrusions	380	545	20	82
25	Extrusion	325	440	18	73
	Non-extrusions	290	425	20	73
300	Extrusions	230	330	25	69
	Non-extrusions	220	330	25	69

Again, depending on the UFG processing route adopted, subtle changes in ductility exists. Thus, a comparison of the UFG Al alloys processed using different routes (Figure 1.1) indicates a general reduction in uniform ductility with ECAP processing. In contrast, friction stir processing (FSP) appears to enhance the uniform ductility (e.g. Al4Y4Ni1Co/AA7075). Such positive effect of FSP on uniform ductility has been observed even in UFG Al-Mg alloys [24]. This change in ductility with processing route is of practical significance, for both the FSP and UFG community. Thus, a judicious choice of friction stir welding parameters can lead to a significant gain in the weld joint mechanical property. Similarly, a fundamental understanding of

the FSP microstructure can lead to an optimum UFG alloy design with improved strength and ductility. In the next section a brief review of friction stir welding/processing is presented.

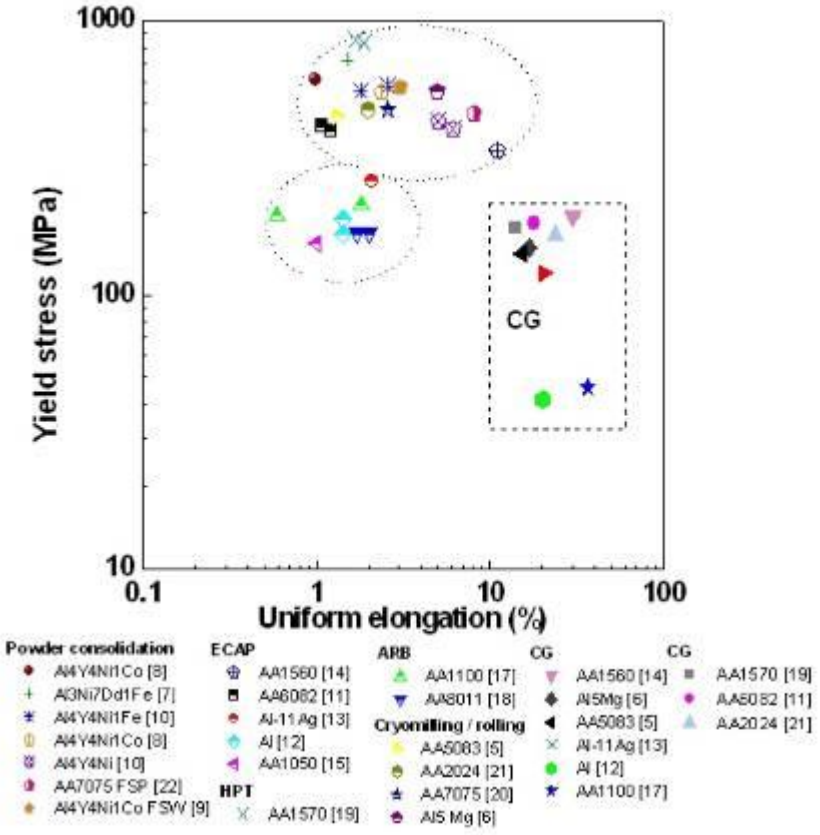

Figure 1.1 The variation of yield stress of different ultrafine grain alloys with respect to their uniform elongation [5 – 23].

1.2 FRICTION STIR WELDING/PROCESSING

Friction stir welding (FSW) is an advanced joining process developed by The Welding Institute (TWI) of UK in 1991[25-26]. In the original process, a non-consumable rotating tool

comprising of an extended flat shoulder region and a pin was inserted into the metal joint and then traversed along the seam. The pieces to be welded being kept fixed with respect to each other during the process. In Figure 1.2 a schematic flow chart of FSW in terms of the principal processes occurring is presented.

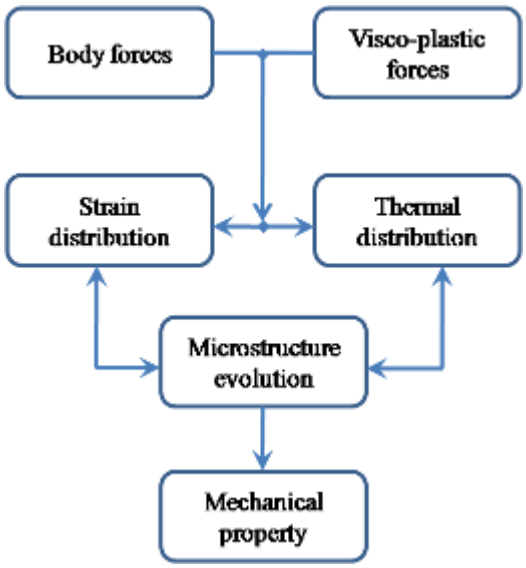

Figure 1.2 Different processes active in FSP/FSW and their mutual interactions.

Friction stir processing (FSP), an offshoot of FSW, was first developed by Mishra et al [27-28] as a tool for localized microstructure modification. The intricacy of the process is however amply illustrated in the wide variation of mechanical properties during FSW/FSP depending on the nature of alloy treated. Thus, FSP of a non heat treatable Al alloy leads to a retention/improvement in the parent mechanical property [29]. On the other hand, heat treatable Al alloys show a reduction in their mechanical strength [29]. This reduction has been associated with the dissolution of strengthening precipitates within the matrix [29]. In Figure 1.3 a schematic diagram of the generalized microstructural evolution process occurring during FSP/FSW is presented.

1.3 THERMO-MECHANICAL PROCESSES IN FSW/FSP

As seen from Figures 1.2 and 1.3, a strong coupling between the microstructural, mechanical and thermal processes during FSW/FSP exists. Considering the thermal process first; a successful thermal model for FSW/FSP would require a heat source model with appropriate boundary conditions. One of the earliest attempts in this regard involved in assigning a coefficient of friction to the pin and shoulder regions of the FSW/FSP tool. The frictional heat generated during FSW/FSP was assumed to be a point/line source of energy [31]. A general heat conduction model was then used, to determine the weld thermal profile. The heat conduction model given as,

$$k\left(\frac{\partial^2 T}{\partial x^2}+\frac{\partial^2 T}{\partial x^2}+\frac{\partial^2 T}{\partial x^2}\right)+\dot{q}=\rho C_p\frac{\partial T}{\partial t} \tag{1}$$

where k the heat conductivity, ρ the density and C_p the specific heat capacity are typically considered to be constants. Now, the assumptions, of a line/point heat source with constant k/C_p, are not valid for FSW/FSP. An accurate modeling therefore requires a consideration of the finite tool dimension combined with the dynamic changes in k and C_p. Consequently, a standalone thermal model for FSW/FSP does not represent the process in its reality.

Determination of the deformation during FSW/FSP is done by two principal approaches. One of the modeling approaches involves the use of computational fluid dynamics (CFD) method. Any flow process can be represented by the continuity and conservation of momentum principles (equation 2 and 3) given as,

$$\frac{\partial\rho}{\partial t}=-\left[\frac{\partial(\rho v_x)}{\partial x}+\frac{\partial(\rho v_y)}{\partial y}+\frac{\partial(\rho v_z)}{\partial z}\right] \tag{2}$$

$$\frac{\partial(\rho\vec{v})}{\partial t}=-\left[\nabla\cdot\vec{\tau}\right]-\left[\nabla\cdot\rho\vec{v}\vec{v}\right]-\nabla P+\rho g \tag{3}$$

Under constant density conditions equations 2 and 3 simplifies to the familiar Navier-Stokes equation. The current FSW/FSP models developed using CFD utilizes this Navier-Stokes formulation [32, 33]. A more accurate modeling approach would however involve a coupling of the thermal and flow equation models (Equations (1 to 3)). This approach has been used by a number of workers the most elaborate of which till date is the one reported by Schmidt and Hattel [34]. It may be clarified here that Schmid and Hattel's model involved a metal deformation based approach where an energy based functional was used to derive the finite element formulation

[34]. In all the modeling initiatives mentioned above, the metal was considered to be a visco-plastic fluid where the flow stress was a function of both strain rate and temperature. A successful solution to the problem therefore requires an accurate description of the flow stress. A popular approach adopted in this regard is the Sellars-Tegart model expressed as [35],

$$\dot{\varepsilon} \exp\left(\frac{Q}{RT}\right) = A(\sinh \alpha\sigma)^n \tag{4}$$

where A, α, n are the microstructural constants, Q the activation energy for deformation. It may be mentioned here that the process modeling approach described above is associated with a number of uncertainties some of which will be discussed next.

As a case in point, consider the flow stress function (equation (4)) first. Flow stress functions are derived from hot deformation experiments conducted under thermal equilibrium at a given temperature. Now, FSW/FSP process consists of a transitory thermal regime combined with a high deformation rate. Thus, a variation in flow stress between hot deformation and FSW/FSP process is expected. The frictional forces controlling the boundary conditions, is another source of variance. As of yet, the frictional forces in FSW/FSP are not clearly understood. This has resulted in the assumption of different frictional conditions by various authors. The adopted frictional force varies from sticking friction (applied stress = frictional stress) to the slipping friction (frictional stress < applied stress) condition. In fact, in some instances Coulomb friction (friction stress limited to ascertain maximum value) was also adopted. The above mentioned outline of thermo-mechanical processes amply illustrates the overall complexity of FSW/FSP. Consequently, understanding the mechanical property during FSW/FSP is an area of prime interest. In the next subsection a brief review of the microstructural processes active during FSW/FSP is presented.

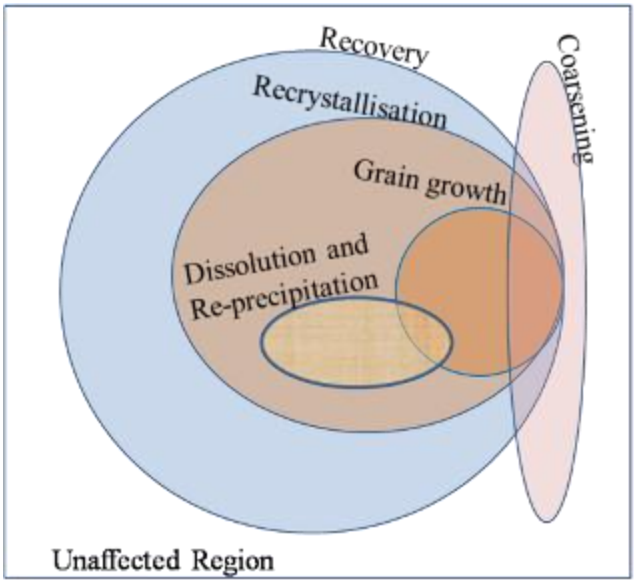

Figure 1.3 The universal process set for microstructure evolution during FSP/FSW with the various subsets. The universal set represents the overall microstructure including weld nugget, thermo-mechanically affected zone, heat-affected zone and parent material.

1.4 MICROSTRUCTURE EVOLUTION DURING FSW/FSP

The microstructure evolution during FSW/FSP can be classified into three different categories. The first category consists of simultaneous recrystallization, resolutionization, precipitation and grain growth and is primarily valid for the weld nugget region. In the second category deformation, precipitation/precipitate growth occurs and is concerned with the thermomechanically affected zone. In the last category precipitation/precipitate growth only is observed. The heat affected zone is an example of this evolution process. The remaining portion of this section discusses the processes active in the weld nugget region only.

As already mentioned, one of the principal phenomena occurring within the weld nugget is recrystallization, which is a combination of two separate processes a) nucleation and b) growth. Now, nucleation for recrystallization differs from the traditional thermodynamics based nucleation where chemical free energy difference is the principal driving force. Thus, discontinuous subgrain growth at sites of high strain energy and orientation gradients is considered to be the principal nuclei source [36]. Consequently, nucleation for recrystallization

strongly depends on the precipitate nature (deformable/non-deformable), size and distributions and is a non-random process. This is in contrast with the precipitate nucleation process (in heat treatable Al alloys) which is thermodynamics based and is random in nature. The simultaneous existence of such random and non-random nucleation processes clearly indicates the complexity of the overall nucleation kinetics during FSW/FSP.

The process of growth during recrystallization/precipitation are however fundamentally different. Thus, growth during recrystallization occurs by grain boundary movement and is controlled by the grain boundary velocity (v) given as,

$$v = M_0 \cdot \exp\left(-Q/RT\right) \cdot P \tag{5}$$

M_0 =coefficient of mobility,

Q = thermal activation barrier and

P = driving pressure.

Solutes, precipitates and textures present can significantly alter this velocity by affecting the grain boundary mobility. The energy stored in the dislocation network distribution $\left(\alpha\rho Gb^2\right)$/subgrain boundaries $\left(3\gamma_0\theta\left(A-\ln\theta\right)/D\right)$ provides the driving pressure (P) for growth. The precipitate growth rate (v_p) on the other hand is controlled by the concentration gradient of diffusing species and is given as,

$$v_p = \frac{D}{r} \cdot \frac{C_m - C_i}{C_p - C_i} \tag{6}$$

Where r is the radius of precipitate, D the diffusivity and C_m and C_p are the diffusing species concentration at matrix and precipitate. The variable C_i is the diffusing species concentration at precipitate/ matrix interface and is obtained from the Gibbs Thomson equation as,

$$C_i = C_{eq} \exp\left(\frac{2\gamma V_m}{rRT}\right) \tag{7}$$

Evidently, depending on the inhomogeneities in growth rate and precipitate resolutionization, a range of precipitate sizes can be obtained. It may be added here that only precipitates larger than a critical size can grow.

Thus, depending on the thermo-mechanical gradients existing in FSW/FSP, a microstructural gradient can develop. In fact, experiments conducted by other investigators show a measurable variation in mean grain size from the shoulder to the pin bottom region [27]. In Figure 1.4, Orientation Imaging Microscopy (OIM) image from three different transverse positions at an area adjacent to the shoulder region and a region ~1 mm below the shoulder region is presented. No perceptible variation in mean grain size at the four different locations was however observed. Therefore, for practical purpose the microstructure within small FSP volumes can be considered to be more or less homogeneous. In the next section an introduction to the principles of OIM along with the rationale behind the choice of OIM parameters for UFG Al characterization is presented.

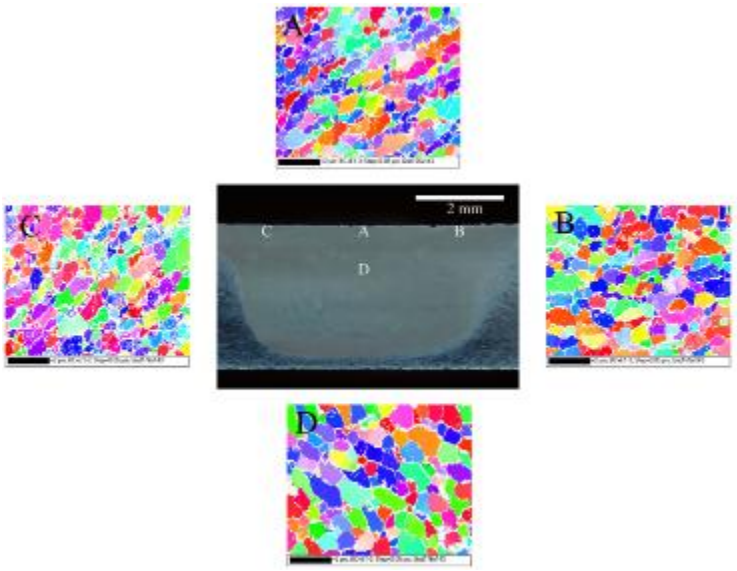

Figure 1.4 Grain distribution at different positions of a FSP AA7075 alloy observed using OIM.

1.5 CHARACTERIZATION OF UFG AL USING OIM

In Figure 1.5 the basic principle and arrangement used in OIM is shown. An incident electron beam interacts elastically with the sample atoms to produce low angle backscattered electrons which diffracts to produce Kikuchi lines. The gnomonic projection of this Kikuchi pattern captured using a video camera, is matched, with the simulated patterns for the given EBSP geometry, to obtain the sample orientation. The EBSP geometry parameter mentioned here specifies the sample/phosphor screen position with respect to the microscope axes and is obtained from the Kikuchi pattern change for a known single crystal at different camera positions.

In Figure 1.6 the operational flow chart for OIM process is presented. As is evident, the accuracy of OIM in determining the orientation is influenced by the ability to produce a representative EBSD pattern followed by its successful digitization. Two principal parameters to measure this accuracy are a) spatial resolution and b) angular resolution. Consequently, a proper choice of microscope operating conditions and image capturing algorithm is of prime significance. The next two subsections discusses the effect of microscope operating conditions and image capturing algorithms on OIM resolution in more details.

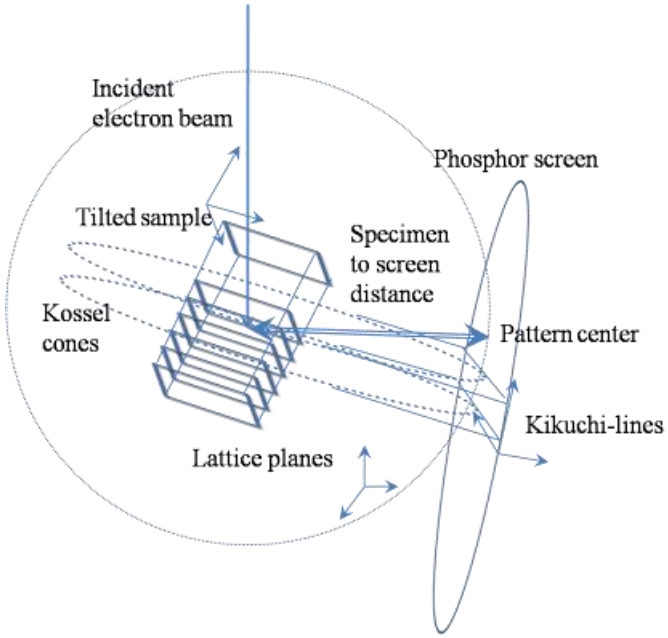

Figure 1.5 The basic principle and the operational setup for OIM.

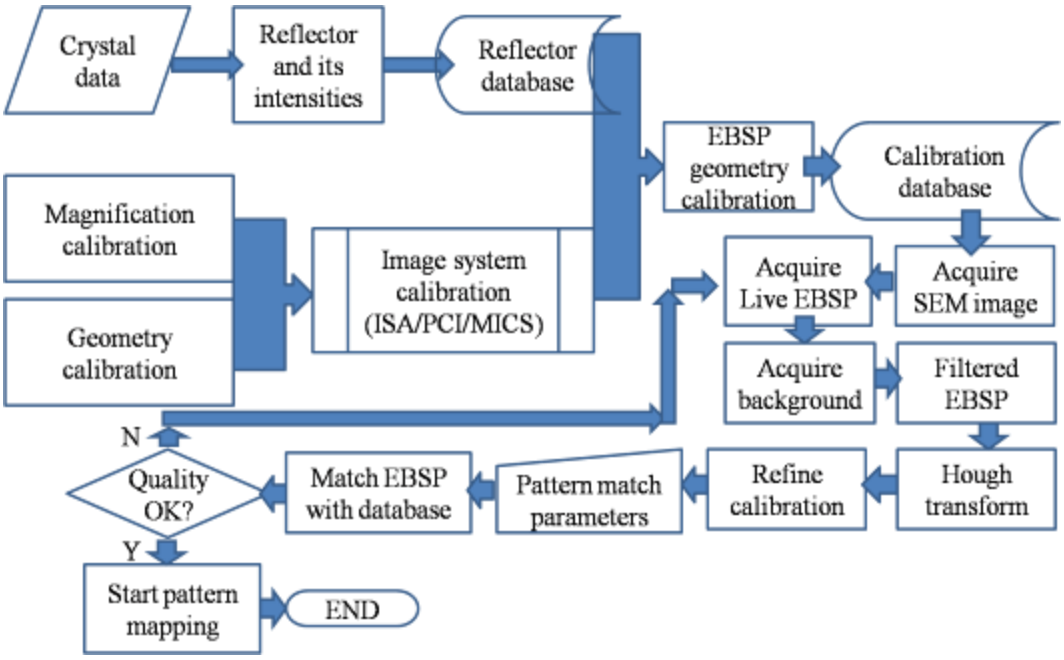

Figure 1.6 Operational flowchart for OIM.

1.5.1 Effect of Operating Conditions on OIM Resolution. To understand the effect of microscopy condition on OIM resolution the effect of tilted sample on interaction volume and emission efficiency of backscattered electron (η) needs further deliberation. Consider the effect of sample orientation on interaction volume first. A common measure for interaction volume is the Kanaya-Okayama range (RKO) where RKO is the electron penetration depth within the sample. For a inclined specimen the RKO is expressed as [37]

$$R_{KO} = \frac{0.0276\, A E_0^{1.67}}{Z^{0.889}\rho}\cos(\theta) \tag{8}$$

where A is the atomic weight (gm/mole), E_0 is the beam energy (keV), Z the atomic number, ρ the density (gm/cm^3) and θ the angle of beam inclination. Thus, an increase in the beam inclination causes a decrease in the electron penetration depth. This interaction volume change is

accompanied by an increase in the electron backscattering efficiency (due to increased forward scattering) given as [37],

$$\eta(\theta) = \frac{1}{(1+\cos\theta)^p} \tag{9}$$

where $p = 9/Z^{1/2}$ for pure elements [37]. Thus, the bulbous interaction volume of a horizontal specimen changes to an elliptical shape at the higher angles (~70˚) used during OIM [38-39]. Consequently, the spatial resolution perpendicular to the tilt axis (L_P) is approximately three times larger compared to the direction parallel to the tilt axis (L_A) [39]. At this point it should be pointed out that although the spatial resolution (as obtained from R_{KO}) for Al is ~100 – 200 nm the actual resolution obtained is much lower. This is due to the intensity difference between overlapping pattern, where the acquiring software successfully analyzes the stronger pattern. It has lead to the concept of effective spatial resolution defined as [39],

$$L_A = \frac{\overline{D}(1-N_S)}{4} \tag{10}$$

where $\overline{D}$ is the average grain size and N_S the fraction of patterns solved. This effective spatial resolution for recrystallised Al in a field emission gun scanning electron microscope (FEGSEM) was found to be ~9 nm (~25 nm for a tungsten filament) and is a function of the probe current and acceleration voltage [39]. Thus, under standard operating conditions, the recommended minimum step size for Al in a FEGSEM was given as ~50 nm [39]. The corresponding accuracy in absolute orientation was found to be ~2˚ [40]. The accuracy in relative orientation measurement using standard pattern transformation (Hough transforms) algorithms was reported as ~1˚ [40]. At this point it should be mentioned that for very small spatial distances (~10 nm), an additional error in orientation measurement occurs at small orientation differences (< 3˚). This is due to the intensity overlap effect from adjacent bands, which actually gets recognized as a new orientation [40].

1.5.2 Effect of Pattern Matching Algorithms on OIM Resolution. A proper choice of pattern matching algorithms and their parameters significantly influences the orientation

measurement accuracy. As already noted (Figure 1.6) background subtraction plays an important role in obtaining a cleaner EBSP pattern. Similarly, EBSP pattern integration over multiple frames effectively reduces the background noise with a consequent rise in EBSP spatial resolution [39]. For a standard FEGSEM microscope with HKL technology software this optimum resolution was obtained at ~8 frames, irrespective of the electron acceleration voltage [39]. However, such multiple frame integration is accompanied by an increase in the computational time required for pattern solving. Consequently 4-5 frame integration was considered to be an optimum choice [39].

The angular resolution of OIM on the other hand is a sensitive function of pattern recognition algorithms. Thus, use of direct pattern shift method compared to the standard Hough transformation results in an increase in the angular resolution at low misorientations [40]. In fact, such direct pattern shift methods are expected to enable EBSD based dislocation microscopy and will be of significant interest in future [41]. The number of Kikuchi lines selected for pattern matching is another significant variable affecting the angular resolution. Thus, with 4-5 band matching, automatic pattern recognition algorithms are capable of achieving an angular precision of less than ~1˚ [42]. Based on all of the above mentioned literature results and existing microscopy conditions the EBSD parameters for UFG Al characterization was selected. A summary of the parameters used are provided in Table 1.2.

Table 1.2 EBSD parameters used for characterizing both ultrafine and coarse grain Al alloys.

Parameter	**Parameter value**	**Parameter**	**Parameter value**
Acceleration voltage	10 kV	Background correction	Dynamic
Emission current	5.5 nA	Time	75 msec
Binning	2	Frame / background	5
Frames integrated	100	Stepsize	50 nm

1.6 MONOTONIC AND CYCLIC DEFORMATION IN AL ALLOYS

As already pointed out, structural metallic materials are classified into three types a) microcrystalline b) ultrafine grain and c) nanocrystalline. A significant change in mechanical behavior with a transition to the ultrafine grain/nanocrystalline regime is observed. To comprehend the origin behind such differences a brief review of the deformation mechanisms active in microcrystalline metals is now presented.

1.6.1 Stress-Strain Behavior – Single Crystal/Microcrystalline Al. The general stress-strain curve of a monotonically loaded single crystal metal is divided into three different stages depending on the micromechanisms active (Figure 1.7). In the initial stage-I uninterrupted dislocation glide on a single slip plane occurs with no perceptible hardening [43]. This is followed by the linearly hardening ($\partial\sigma/\partial\varepsilon \sim E/200 - E/300$) stage-II caused by dislocation pile up, succeeded by the stage-III of progressively reducing hardening rate associated with dynamic recovery [43]. In Figure 1.7b the stress-strain curve of Al single crystals oriented in different crystallographic directions are presented. As may be noted, depending on the orientation difference between tensile and crystallographic axis all or only part of the general stress strain curve is observed.

The stress-strain behavior of a cyclically loaded single crystal is represented by the cyclic stress-strain (CSS) curve. Figure 1.8 shows the general single crystal CSS curve with three different stages (I to III), each with their own typical microstructural and stress-strain characteristics. In Figure 1.8b the CSS curve for an Al single crystal is shown [45]. Quite clearly, the CSS curve of Al has its own unique characteristics. The corresponding microstructural evolution is also notably different. Thus, in single crystal Al persistent slip band (PSB) structure typical of face centred cubic (f.c.c.) metals like Cu/Ni has not been observed. However, despite such subtle variations, the overall microstructural process active during cyclic loading in f.c.c. crystals are considered to be similar in nature.

In Figure 1.9 the monotonic and CSS curves for microcrystalline Al is reproduced. As in the case of single crystal Al oriented in multiple slip direction (K in Figure 1.7b) the polycrystalline stress strain curve is characterized by the absence of a stage-I region. The general curve consists of a small athermal stage-II (initial part where the curves superimpose in Figure 1.9a) followed by an extended stage-III. The microcrystalline CSS curve exhibits a continuously hardening trend (stage-III) unlike the cyclic hardening-softening-hardening trend noted in Al single crystals. Comparison of the microstructural features between microcrystalline and single

crystal Al however shows an overall similarity in the deformation process. The next section discusses the deformation micro-mechanisms in microcrystalline Al alloys in more detail.

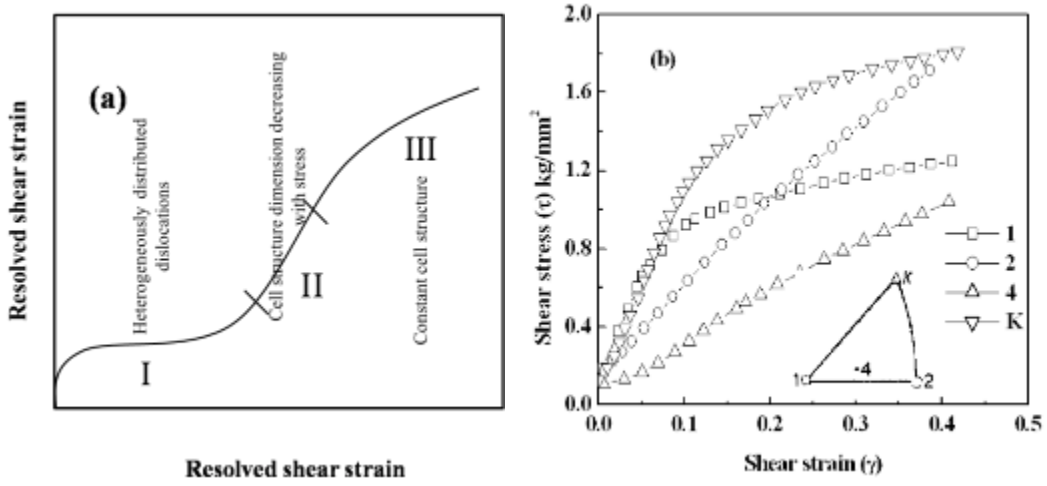

Figure 1.7 a) General single crystal stress strain curve and associated microstructural features b) Stress strain curves of Al single crystals in different crystallographic orientations [44]. Each curve corresponds to a specific crystallographic direction (see inset).

1.6.2 Mechanical Behavior of Microcrystalline Al Alloys. The mechanical behavior of an Al alloy differs significantly from that of single phase pure Al. This is due to the additional resistance from solutes and precipitates on the dislocation movement. Now, any slip dislocation movement is associated with an intrinsic lattice resistance (Peierl's-Nabarro force, $\tau_{P\text{-}N}$) expressed as,

$$\tau_{P-N} \propto G \exp^{-2\pi W/b} \tag{11}$$

where W is the dislocation width and b the burgers vector for dislocation. For pure Al this intrinsic lattice resistance is negligible (see Figure 1.7b) and is a direct consequence of the low Peierl's potential and stress. The presence of solute atoms/forest dislocations creates an additional

interaction increasing the lattice resistance. A common approach to evaluate this interaction involves in assigning a appropriate energy/force profile according to the nature of obstacle. Thus, for dislocation-dislocation forest interaction a rectangular force distance profile has been suggested (Figure 1.10a) [47]. The corresponding resistance force is given as,

$$\tau = \frac{\mu b}{d}\left(\frac{F_{\max}}{\mu b^2}\right)^{3/2}\left(1-\frac{T}{T_0}\right)^{3/2} \tag{12}$$

Where d is the obstacle width, μ the matrix shear modulus and T_0 is the athermal temperature. For dislocation solute interactions a parabolic type force distance profile has been used (Figure 1.10b) [47]. The corresponding resistance stress given as,

$$\tau = \frac{\mu b}{d}\left(\frac{F_{\max}}{\mu b^2}\right)^{3/2}\left(1-\frac{T}{T_0}\right)^{2/3} \tag{13}$$

It may be mentioned here that the above expressions for dislocation-solute and dislocation-dislocation forest interactions (equation 12 and 13) were derived using Friedel's statistics. The basic suppositions for which as [48],

1) Obstacles to the glide are similar shearable point obstacles which are uniformly spaced.
2) The dislocation motion is overdamped and no interactions between different dislocations occur.
3) The bowing of dislocations at obstacles is small and the propagation occurs at steady state.

Unlike in the case of solute atoms/dislocation forests, estimation of dislocation movement resistance by precipitates is complicated by the invalidity of supposition 1 and 2 of Friedel statistics. Moreover, depending on the nature of precipitate present the assumption of shearable obstacles also becomes invalid. Thus, dislocation movement resistance due to precipitate is again classified into two types a) resistance due to shearable precipitates and b) resistance due to non-shearable precipitates (Orowan strengthening). The shearable precipitate resistance again classified as,

a) Chemical strengthening
b) Modulus mismatch strengthening
c) Stacking fault energy mismatch strengthening
d) Lattice mismatch strengthening
e) Order strengthening.

The maximum resistance force in each case is calculated from the basic particle strengthening equation given as,

$$\tau_p b L_c = F_0 \tag{14}$$

Where L_c is the critical length and F_0 is the strength of the obstacle. For non-shearable particles this maximum resistance is given as,

$$\tau_p = \frac{\mu_s b}{L_p} \tag{15}$$

Where L_p is the non-shearable particle spacing.

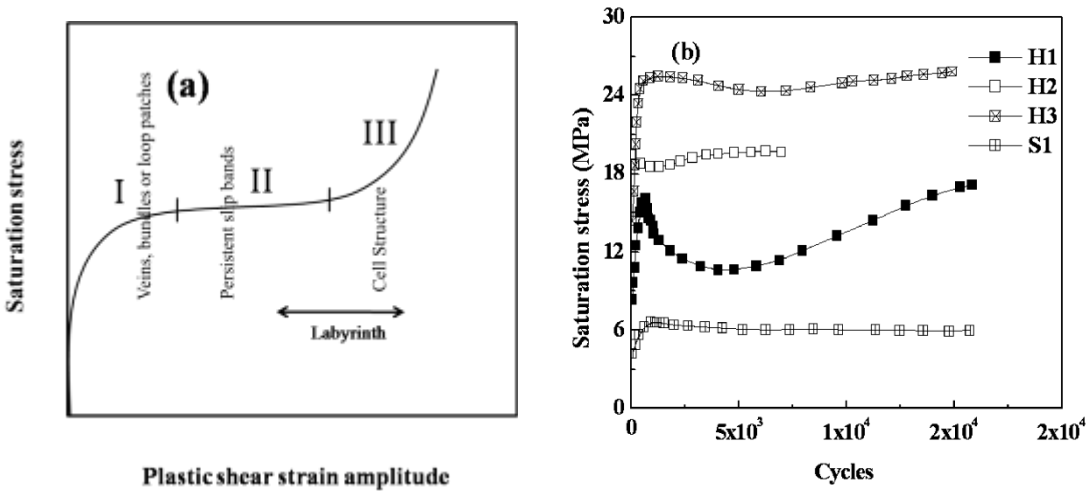

Figure 1.8 a) General cycle stress strain curve with corresponding microstructural features b) Cyclic stress strain curve of Al single crystal [45].

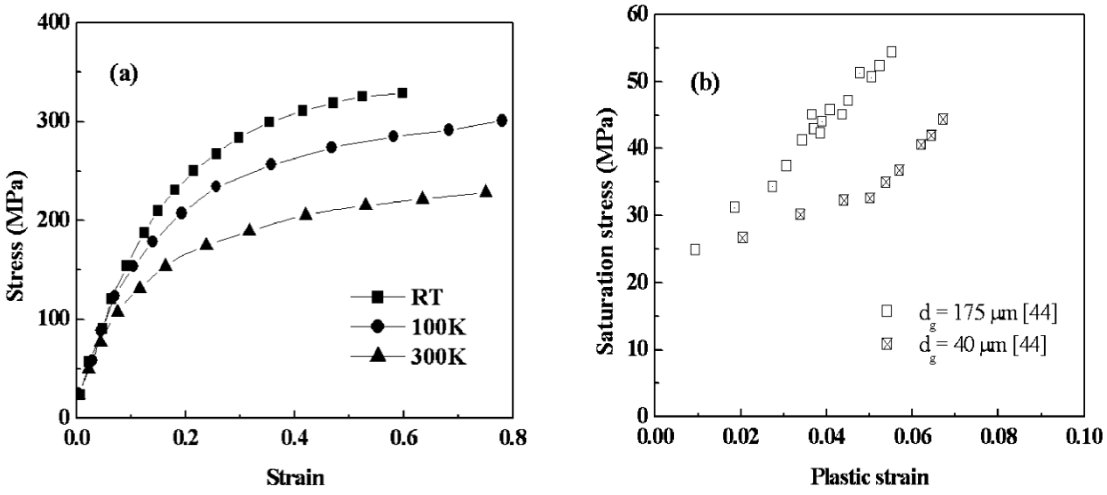

Figure 1.9 a) Monotonic stress strain curve of microcrystalline copper at different temperatures [43]. b) The CSS curve of a commercial purity microcrystalline Al [46].

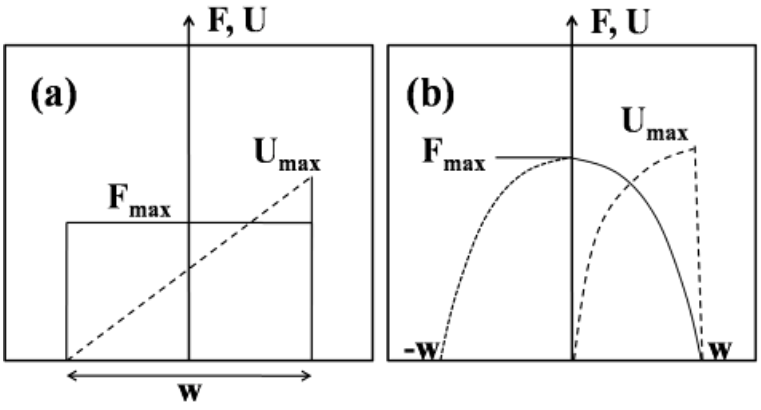

Figure 1.10 Commonly adopted force distance profiles for a) dislocation interaction with dislocation forest [47] b) dislocation interaction with solute atoms [47].

1.6.3 Mechanical Behavior of UFG Al and Al Alloys. As already discussed, in the strengthening mechanisms for microcrystalline alloys, dislocations were considered to move only within the matrix. No dislocation-dislocation or dislocation-grain boundary interactions were considered. Now, any polycrystalline metal can be broadly classified into two distinct regions a) matrix and b) grain boundary. The hypothesis of non-interacting dislocations though valid for microcrystalline metals, is a questionable assumption for ultrafine grain microstructures. To understand the issue further, consider the typical length scale of dislocation movement in Al at room temperatures. At room temperature conditions this is in the range of 1-5 μm (as evidenced from cell size and PSB dimensions – refer to section 1.3.1). This observed length scale of movement is in fact larger than the grain size in ultrafine grain Al (< 1 μm). Consequently, dislocation interaction with grain boundaries and associated strengthening mechanism changes becomes important. This change in strengthening mechanism is amply illustrated in the shift of strength-ductility combinations for UFG Al compared to their microcrystalline counterparts. (see Figure 1.1). The most significant technological issue in this regard pertains to ductility. The remaining part of this section deals with this subject of ductility in more details.

Now, ductility of any metal is determined by its dislocation storage ability. Thus, as long as dislocation storage is homogeneous, a uniform deformation is achieved (e.g. uniform elongation region in a tensile test). Heterogeneous dislocation accumulation on the other hand causes internal notch formation with consequent onset of failure (e.g. non-uniform elongation region in a tensile test). At steady state stress situation the ductility is therefore determined by the following condition

$$\dot{\rho}_{\text{nucleation}} - \dot{\rho}_{\text{annihil}} = \dot{\rho}_{\text{storage}} \tag{16}$$

where $\dot{\rho}_{\text{nucleation}}$ is the dislocation nucleation rate, $\dot{\rho}_{\text{annihil}}$ is the dislocation annihilation rate and $\dot{\rho}_{\text{storage}}$ is the rate of dislocation storage. The low ductility of UFG Al as compared to their coarse grain counterparts therefore indicates a lower dislocation storage rate. In the next section the monotonic ductility aspect of UFG Al is discussed in more details.

1.6.3.1 Monotonic ductility in UFG Al-a review. The common methodology to predict ductility in metallic material has been phenomenological in nature. The approach consists of representing the stress-strain curve of a material in the power law form of Zener-Holloman type expressed as,

$$\sigma = K\varepsilon^{n} \tag{17}$$

where K and n are material constants. At maximum stress this leads to the Considere's criterion for plastic instability given as,

$$\frac{d\sigma}{d\varepsilon} = \sigma \tag{18}$$

Thus, the uniform ductility (ε_u) of a metal is equal to the value of 'n'. It may be observed here that equation (17) is independent of the time variable and shows no rate dependency. The rate dependency of stress-strain curve was expressed for the first time in the phenomenological study of plastic deformation by E.W. Hart [49]. According to this work, the plastic deformation of a face centered cubic metal can be expressed in a differential form as,

$$d\ln\sigma = \frac{\partial \ln\sigma}{\partial\varepsilon} d\varepsilon + \frac{\partial \ln\sigma}{\partial \ln\dot{\varepsilon}} d\left(\ln\dot{\varepsilon}\right) \tag{19}$$

Combining the above equation with the constancy of volume criteria, the condition for plastic deformation instability was obtained as [50]:

$$\frac{\partial \ln\sigma}{\partial\varepsilon} + \frac{\partial \ln\sigma}{\partial \ln\dot{\varepsilon}} < 1 \tag{20}$$

For $\partial \ln\sigma / \partial \ln\dot{\varepsilon}$ ~0, Hart's criteria leads to the Considere's criteria for necking (equation (18)). It may be mentioned here that the derivation of Hart's criterion was restricted to the macroscopic instabilities. Localized instabilities/shear localization on slip planes was not taken into consideration. Consequently, any microscopic instability will lead to a violation of the Hart's criterion.

This inapplicability of Hart's criterion was clearly demonstrated in the experiments on UFG AA6082 alloy where micro-shear banding was observed [11]. Another notable phenomenon for UFG Al/Al alloys was the increase in uniform ductility with a reduction in the strain rate of testing [11, 51]. This increase in ductility was accompanied by a decrease in the flow stress. It may be mentioned here that for UFG Al a slight increase in the strain rate sensitivity

($m = \partial \ln \sigma / \partial \ln \dot{\varepsilon}$) has been observed. Thus, ECAP AA6082 alloy of Sabirov et al [11] exhibited a m value of ~0.029. Similar strain rate sensitivity experiments on UFG, Al-Ni-Y-Co-Sc alloy showed an 'm' value in the range of 0.02 to 0.03 [52]. Till date, no definite explanations for these observations have been obtained. In fact, most of the work on ductility [5-24] and its improvement have been experimental in nature. E. Ma has summarized the different methods available to improve UFG ductility as [53],

a) multimodal grain structure
b) multiphase metals
c) nano-scale twins
d) nano-precipitate dispersion
e) phase transformation

However the micro-mechanisms behind such improvements are still not fully understood. The questions therefore are,

- **Is dislocation storage key to improve UFG Al ductility?**
- **How does grain boundary affect UFG Al ductility?**
- **How does FSP improve UFG Al ductility?**

1.6.3.2 Cyclic deformation in UFG Al-a review. In the previous section UFG Al ductility was discussed from a traditional viewpoint. This approach is effective as it permits an experimental measurement of ductility. But, the influence of uniform ductility on cyclic deformation property is no less important. The significance is clearly demonstrated in the Coffin-Manson's law for low cycle fatigue given as,

$$\frac{\Delta \varepsilon_p}{2} = \varepsilon_f' \left(2N_f\right)^c \tag{21}$$

Where ε_f' and c are known as the fatigue ductility coefficient and exponent respectively. In general, the fatigue ductility coefficient is equated with the true fracture strain of a material, while c is considered to be a material constant. However, despite such phenomenological connections between monotonic and cyclic loading no micromechanical explanation in this regard is available. The remaining part of this section, explores the microstructural complexities associated with UFG Al fatigue further.

As already observed in Figures 1.7b, 1.8b, and 1.9 a fundamental similarity in the monotonic and cyclic micromechanisms of single crystal and microcrystalline Al exists. Thus, in both cases cell structure formation remains the principal damage accumulation method. The fundamental mechanisms for failure are also similar (PSB for cyclic deformation and strain localization for monotonic deformation). In UFG regime, the context however changes in the following two aspects:

a) the sub-micron grain sizes of UFG metals are similar or smaller in length scale than the cell size observed in single crystal or microcrystalline Al alloys, and
b) UFG grain sizes have dimensions comparable to the typical PSB width and wall thickness combined together.

Consequently, significant difference in the damage evolution of a UFG metal (compared to microcrystalline metals) is expected. An example of this is observed in the microstructural changes occurring in a UFG single phase Cu during fatigue. The principal features of which can be summarized as,

a) persistent shear band formation on surfaces [59],
b) occurrence of coarsened cell structure with typical MC fatigue features of vein and PSB formation within the cell structures [60-62], and
c) recrystallisation during fatigue [60-62].

Similar experiments conducted on single phase UFG Al (ECAP route) by Hoppel et al. [63] indicates a grain coarsening tendency with shear band development. However, a more detailed microstructural investigation conducted by Wong et al. [64] on ECAP-processed UFG Al (99.5%), revealed no significant grain coarsening/damage during fatigue. These contradictory results lead to one key question,

- **How is fatigue damage accommodated in UFG Al?**

Again, cyclic deformation experiments on ECAP Al alloys by May et al [51] showed a decrease in fatigue life with an increase in the strain rate. No such strain rate effect on fatigue life has been reported for microcrystalline Al alloys. Moreover, such cyclic fatigue life reduction with strain rate decrease contradicts the effect of increasing uniform ductility with a decrease in the strain rate [11, 51]. In fact, the increase in uniform ductility at lower strain rates is expected to improve the low cycle fatigue life (via Equation 21). This leads to some more interesting questions:

- **How does deformation mechanism in UFG Al vary from the microcrystalline?**
- **How does dislocation annihilation/storage rate affect UFG fatigue life?**

1.7 SCOPE OF CURRENT DISSERTATION

In the previous sections, some basic queries with respect to UFG Al ductility and fatigue were introduced. It may be mentioned here that fatigue and ductility mechanisms in microcrystalline metals is in itself a complex issue. Reduction in grain size into the ultrafine grain regime has introduced further challenges in this understanding. Therefore, an appreciation of the difference in microstructural response between ultrafine grain and microcrystalline Al during fatigue and tensile loading is of particular relevance. The current work is a comprehensive attempt to characterize and understand the changes occurring during fatigue and monotonic testing in a two phase ultrafine grain Al alloy developed using FSP. The dissertation is organized into five papers which are listed as follows:

1. **Subsize fatigue testing**

   In this phase of work, a subsize bending fatigue test capability was developed. This included designing a subsize specimen with its corresponding testing bed. The subsize fatigue testing facility was verified with that of a commercial AA7075 – T6 alloy sheet.

2. **Effect of microstructure on fatigue in microcrystalline Al alloy**

   A rolled Al-Li alloy was examined for it S-N curve characteristics using OIM, STEM and SEM. Effect of ordered precipitate, texture and grain size on crack propagation characteristics and fatigue life was investigated. The effect of FSP on fatigue life and fracture was also dealt with.

3. **Cyclic deformation characteristics in FSP fine grain Al alloy**

   A fine grain (1-3 μm) AA7075 alloy microstructure was produced using FSP. The high cycle fatigue life of the fine grain microstructure was compared to that of a coarser one. A fractography based explanation to the S-N curve changes was presented.

4. **Effect of microstructure on fatigue in FSP, UFG Al alloy**

   A UFG AA7075 alloy (average size ~ 0.5 μm) microstructure was produced using friction stir processing. Its high cycle fatigue life was compared to that of a coarse grain and a fine grained AA7075 alloy. The fatigue life change was explained on the basis of microstructural differences. The stability of UFG microstructure during fatigue was also investigated.

5. **Ductility of FSP, UFG Al alloy**

   The ductility behavior of a two phase, UFG Al alloy was studied with the help of OIM. The stress-strain behavior was modeled using a combination of thermally activated dislocation annihilation mechanism along with dislocation storage at second phase.

1.8 REFERENCES

1. M.A. Meyers, A. Mishra, D.J. Benson, "Mechanical properties of nanocrystalline materials", Prog. in Mater. Sci., 51 (2006), 427-556.
2. R.E. Reed-Hill, R. Abbaschian, "Physical Metallurgy Principles", 3rd Edn., PWS-Kent Publishing company,1992.
3. H. Gleiter, "Nanocrystalline materials", Prog. in Mater. Sci.,33 (1989),223-315
4. J.G. Kaufman, 1999, "Properties of Aluminum alloys", The Aluminum Association Inc and ASM International, 22-23.
5. D.Witkin,B.Q. Han, E.J. Lavernia, Metal Mater. Trans., 37A (2006); 185-194
6. K.M. Youssef, R.O. Scattergood, K.L. Murty, C.C. Koch, Scripta Mater., 54 (2006); 251-256.
7. X.L. Shi, R.S. Mishra, T.J. Watson, Scripta Mater., 52 (2005); 887-891.
8. Y. Wang, X.L. Shi, R.S. Mishra, T.J. Watson, Scripta Mater., 56 (2007); 923-925.
9. Y. Wang, X.L. Shi, R.S. Mishra, T.J. Watson, Scripta Mater., 56 (2007); 971-974.
10. X.L.Shi, R.S. Mishra, T.J. Watson, Mater. Sci. Eng. A., 494 (2008); 247-252.
11. I. Sabirov, Y. Estrin, M.R. Barnett, I. Timokhina, P.D. Hodgson, Scripta Mater., 58 (2008); 163-166.
12. J. May, H.W. Hoppel, M. Goken, Mater. Sci. For., 503-504 (2006); 781-786.
13. Z. Horita, K. Ohashi, T. Fujita, K. Kaneko, T.G. Langdon, Adv. Mater. 17 (2005); 1599-1602.
14. M.V. Markushev, M.Y. Murashkin, Mater. Sci. Eng. A, 367 (2004); 234-242.
15. P.L. Sun, C.Y. Yu, P.W. Kao, C.P. Chang, Scripta Mater., 52 (2005); 265-269.
16. P.L. Sun, E.K. Cerreta, G.T. Gray III, P. Rae, Mater. Sci. Eng. A, 410-411 (2005); 265-268.
17. N. Tsuji, H. Ito, Y. Saito, Y. Minamino, Scripta Mater., 47 (2002); 893-899.
18. H.W. Kim, S.B. Kang, N. Tsuji, Y. Minamino, Mater.Sci. For., 512 (2006); 85-90.
19. R. Valiev, Mater. Sci. For., 584-586 (2008); 22-28.
20. Y.H. Zhao, X.Z. Liao, S. Cheng, E. Ma, Y.T. Zhu, Adv. Mater., 18 (2006); 2280-2283.
21. S. Cheng, Y.H. Zhao, Y.T. Zhu, E. Ma, Acta Mater., 55 (2007); 5822-5832.
22. P.S.De, R.S. Mishra, C.B. Smith, Scripta Mater. 60 (2009); 500-503.
23. R. Kapoor, P.S. De, R.S. Mishra, Mater. Sci. For., 633-634 (2010); 165-177.
24. R.Kapoor, N. Kumar, R.S. Mishra, C.S. Huskamp, K.K. Sankaran Mater. Sci. Eng (A) 527 (2010) 5246-5254.

25. W.M. Thomas, E.D. Nicholas, J.C. Needham, M.G. Murch, P. Templesmith, C.J. Dawes, G.B. patent Application No. 9125978.8 (December 1991).

26. C. Dawes, W. Thomas, TWI Bulletin 6 November/December 1995;124.

27. R.S. Mishra, M.W. Mahoney, S.X. McFadden, N.A. Mara, A.K. Mukherjeee, Scripta Mater. 42 (2000) 163-168.

28. R.S. Mishra, M.W. Mahoney, Mater. Sci. For. 357-359 (2001); 507-514.

29. R.S. Mishra, Z.Y. Ma, Mater. Sci. Eng.(R), 50 (2005); 1-78.

30. Y.S. Sato, H. Kokawa, M.Enmoto, S. Jogan, Metall. Mater. Trans. A 30 (1999); 2429-2437.

31. H.R. Shercliff, P.A. Colegrove, Modeling of Friction Stir Welding, "Mathematical Modeliing of Weld phenomena 6" H.Cerjak, H. Bhadeshia, Ed., Maney Publishing, London, U.K. 2002; 927-974.

32. P. Colegrove, H.R. Shercliff, J. Mater. Process. Technol. 169 (2005); 320-327.

33. R. Nandan, G.G. Roy, T. Debroy, Metall. Mater. Trans. A 37 (2006); 1247-1259.

34. H.Schmidt, J. Hattel, Model. Simul. Mater. Sci. Eng. 13 (2005); 77-93.

35. C.M. Sellars, McG.Tegart, Hot Workability, Inter. Mater. Rev. 17 (1972); 1-24.

36. F.J. Humphreys, M. Hatherly, Recrystallization and related annealing phenomena, Elsevier Science Ltd., 1995.

37. J.I. Goldstein, D.E. Newbury, P. Echlin, D.C. Joy, C. Fiori, E. Lifshin, Scanning Electron Microscopy and X-ray Microanalysis, Plenum Press, 1984.

38. V. Randle, O. Engler, Introduction to Texture Analysis Macrotexture, Microtexture & Orientation Mapping, Gordon and Breach Science Publishers, 2000.

39. F.J. Humphreys, I. Brough, J. of Microscopy 195 (1999); 6-9.

40. I. Brough, P.S. Bate, F.J. Humphreys, Mater. Sci. and tech. 22 (2006); 1279-1286.

41. B.L. Adams, C.J. Gardner, D.T. Fullwood, Solid state Phenom. 160 (2010); 3-10.

42. N.C.K. Lassen, J. of Microscopy, 181 (1996); 72-81.

43. U.F. Kocks, H. Mecking, Prog. in Mater. Sci. 48 (2003); 171-273.

44. U.F.Kocks, Acta Metall. 6 (1958); 85-94.

45. O. Vorren, N. Ryum, Acta Metall., 36 (1988); 1443-1453.

46. Y. El-Madhoun, A. Mohammed A, M.N. Bassim, Mater. Sci. Eng. A 359 (2003); 220-227.

47. D. Caillard, J.L. Martin, Thermally activated Mechanisms in Crystal Plasticity, Elsevier Ltd., 2003.

48. E. Nembach, Particle Strengthening of Metals & Alloys, John Wiley and Sons, 1997.

49. Hart EW. Acta Metall. 18 (1970); 599-610.

50. Lin LH, Hirth JP, Hart EW. Acta Metall. 29 (1981); 819-827.

51. May J, Amberger D, Dinkel M, Hoppel HW, Goken M, Mater. Sci. Eng. (A) 483-484 (2008); 481-484.

52. A. Dutta, P.S. De, R.S. Mishra, T.J. Watson, Mater. Sci. Eng (A) 513-514 (2009); 239-246.

53. E. Ma, JOM April (2006); 49-53.

54. H. Mughrabi, Mater. Sci. Eng. A 33 (1978) ; 207-223.

55. Z.S. Basinski, S.J. Basinski , Prog. Mater. Sci. 36 (1992); 89-148.

56. C.E. Feltner, Acta Metall. 11 (1963); 817-828.

57. W. Vogel, M. Wilhelm, V. Gerold, Acta Metall. 30 (1982); 21-30.

58. D.J. Duquette, P.R. Swann, Acta Metall. 24 (1976); 241-248.

59. S.R. Agnew, A.Y. Vinogradov, S. Hashimoto, J.R. Weertman, J. Electron Mater. 28 (1999); 1038-1044.

60. S.R. Agnew, J. Weertman, Mater. Sci. Eng. A 244 (1998); 145-153.

61. S. Hashimoto, Y. Kaneko, K. Kitagawa, A. Vinogradov, R.Z. Valiev, Mater. Sci. Forum 312-314 (1999); 593-598.

62. H.W. Hoppel, Z.M. Zhou, H. Mughrabi, R.Z. Valiev, Phil. Mag. A 82 (2002); 1781-1794.

63. H.W. Hoppel, C. Xu, M. Kautz, N. Barta-Schreiber, T.G. Langdon, H. Mughrabi, In: M.J. Zehetbauer, R.Z. Valiev editors. Proceedings of second international conference on nanonmaterials by severe plastic deformation. Winheim: Wiley-VCH (2004); 677-683.

64. M.K. Wong, W.P. Kao, J.T. Lui, C.P. Chang, P.W. Kao, Acta Mater. 55 (2007); 715-725.

PAPER

I. DEVELOPMENT OF A REVERSIBLE BENDING FATIGUE TEST BED TO EVALUATE BULK PROPERTIES USING SUB-SIZE SPECIMENS

P. S. De, C. M. Obermark and R.S. Mishra

Center for Friction Stir Processing, Department of Materials Science and Engineering

University of Missouri, Rolla, MO 65409, USA

ABSTRACT

A non-standard fully reversible bending fatigue test bed of fixed displacement amplitude type was designed. A sub-size sample similar in design to the standard ASTM –B593 sample was used to evaluate the high cycle bend fatigue behavior of 7075-T6 sheet specimens. Fatigue life was determined at four stress levels of 300, 240, 220 and 190 MPa at a stress ratio of -1.

Keywords: Fatigue test method; Sub-size specimen; High cycle fatigue; S-N curve

INTRODUCTION

The fatigue property of metallic materials is critical for many structural applications and can be tested under axial, bending or torsion load conditions. ASTM – B593 [1] is a commonly adopted standard for testing copper- alloy spring materials under completely reversible bending fatigue conditions. This method can also be used to study fatigue properties of new materials under research testing conditions. However, the scope of this standard is limited by the specified sample size and the testing method becomes inapplicable in situations where sufficient material is unavailable either due to processing restrictions or microstructural gradients. Development of new structural materials and processes require a thorough evaluation of mechanical properties, both under static and dynamic conditions. For such instances, development of sub-size testing solutions is desirable to get data for initial screening.

Use of miniature specimens for evaluating tensile, fracture toughness and fatigue properties are already a common practice in the nuclear industry [2]. However, the existing sub-size specimen designs [2] are suitable for fatigue property determination in axial loading conditions only. The objective of this study was to design a bending fatigue type test system to evaluate the fatigue properties from small volumes of materials. This is intended to be used for evaluating relative fatigue properties of materials with microstructural gradients, such as friction stir welded/processed materials where, the processed material volume is small, limiting the use of standard tests to evaluate the welded zone property. Obviously, application of such testing

systems can be extended to other welding and processing techniques. This would be beneficial from both processing and fundamental viewpoints.

Designing of sub-size specimen representative of the bulk material requires the consideration of specimen size effect [3] on the deformation micro-mechanism, which ultimately influences the overall response. For instance, the grain size and number of grains in the cross-section of the specimen will determine whether grain boundary hardening is the controlling factor in the deformation process of an actual specimen [3]. Thus, for the Hall-Petch mechanism to be effective, a minimum number of grains should be available in the specimen volume. The sample size effects in aluminum sheets were recently discussed [3], where the authors showed that for t /d >3, flow stress of the metal is independent of t/d, where t is the specimen thickness and d is the grain size. Specimen geometry is another important consideration to prevent notch/stress raiser effects capable of influencing the results.

Design of a sub-size specimen can be classified as [2], (a) a specimen similar in geometry to standard specimen but smaller in size, or (b) a specimen of non standard geometry developed specifically for a particular application. For a comprehensive discussion on mechanical property measurement and the influence of specimen size and geometry, the reader is referred to an excellent review article by Hyde et al [2].

In this study, the designed system was used to generate the stress (S) – life (N) data for a 1 mm thick 7075-T6 sheet material. The testing system comprised of a crank and lever arrangement and testing was done until failure. All fatigue data presented in this paper were evaluated in accordance with the guideline prescribed in ASTM E739 -91 (2004) [4,5].

SPECIMEN DESIGN

The design of the sub-size fatigue specimen used is shown in Fig. 1 and is a hybrid version of Krouse type sheet or strip fatigue specimen [1]. Straight line portion of the specimen contour makes an angle of 13° with the horizontal axis with the specimen gripped at the widest part (hatched region in Fig. 1) through a flat gripper surface to minimize the chances of stress raisers. Point of application of force on the specimen is near to point A where the two straight lines drawn along the edges intersect, thus simulating the bending situation in a cantilever beam [1]. The maximum bending stress can be calculated using the Eq. (1)

$$S = 6PL / bd^2 \quad (1)$$

where, S is the desired bending stress in N/m^2, P is the force in N, L is the distance between axis of point of load application and point of stress calculation in meters, b is the width of the

specimen at the distance L from point of load application in meters and d is the specimen thickness in meters.

EXPERIMENTAL

The testing system comprises of a crank driven by a DC motor (maximum rotational speed 2000 rpm) connected to a lever arrangement which transforms the rotary motion to a linear oscillatory motion as shown in Fig. 2. During testing, the specimen is placed in a fixed supported cantilever position, with a concentrated oscillatory force being applied very near to point A (Fig. 1).

Mini fatigue specimens were face milled from 1.25 mm thick 7075-T6 aluminum alloy sheets using a mini-CNC machine at a feed-rate of 1 mm/minute. All the specimens were machined in the rolling direction of the sheet. The flat surfaces of the specimen were kept in as-received condition, while the edges were kept in as milled condition. Specimens were tested for high cycle fatigue life at four different stress amplitudes (S_a) of 300, 245, 220 and 190 MPa, with a stress ratio(R) of -1 in all cases. All the experiments were tested at a frequency of 25 Hz. Six specimens were tested at each stress level in compliance with the recommended practice for statistical analysis of linear S-N curve [5] except for the one performed at 190 MPa stress level. All the samples were tested until the fatigue crack has propagated throughout the sample. Failure detection was done using a snap-action switch activated by the deflection of load cell on breakage of the test piece.

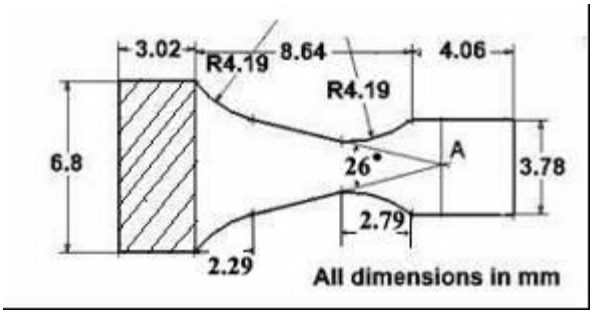

FIG. 1–*Drawing of the sub-size fatigue test specimen (all dimensions are in millimeters). Hatched region is the fixed support portion of cantilever*.

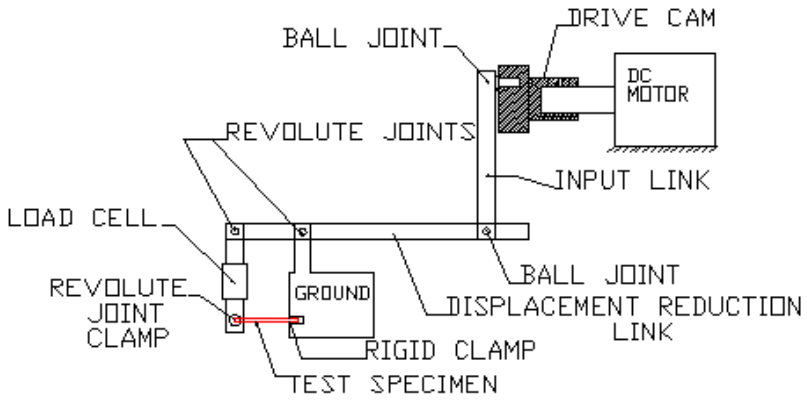

FIG. 2–*Schematic diagram of the fully reversible bending fatigue machine used to test the sub-size specimens.*

RESULTS AND DISCUSSION

Detailed experimental results are presented in Table 1 which also incorporates fatigue life data at 300 MPa fatigue life conducted at a frequency of 10 Hz. This was done to evaluate the influence of testing frequency on fatigue life. The data generated so far does not show any influence of testing frequency on fatigue life at these rates. The specimen fracture surfaces were investigated under low magnification to understand the stress state of system. A sample fracture surface of specimen-2 for the samples subjected to 220 MPa is shown in Fig. 3 as a representative example. The ratchet marks at Region 1 shows that the fatigue crack initiated from intermetallic particles residing on the surface of specimen (Fig. 3(b)). The crack propagated in a distinct stage-I mode identified in Fig. 3(a) as Region 2, which changed to stage-II type crack propagation in Region 3 and final fast fracture (Region 4) exhibiting voids indicative of a ductile failure mode. Higher magnification fractographs from these regions are shown in Figs. 3(b)–3(e). The fracture positions of tested samples were distributed along the straight line segment of the specimen. In some cases the origin of fracture surface could not be definitively identified. This was especially so for samples tested at highest alternating stresses.

The fatigue life of 7075-T6 alloy obtained from this study is compared to the data presented in Ref. [6]. At 255 MPa, the fatigue life for flat sheet specimens under completely

reversed flexure is given as 10^5, which is higher than the estimated value of 240 MPa obtained in this study. In general the mini samples tested by present setup show a reduced fatigue life, as seen from Fig. 4. Following the microstructure based multistage fatigue (MSF) model [7] and the small fatigue crack growth approach discussed by Suresh [8], total fatigue life for 7075 – T6 samples tested, can be divided into four consecutive stages such that

$$N = N_{INC} + N_{MSC} + N_{PSC} + N_{LC} \quad (2)$$

where N_{INC} is the cycles spent on crack incubation at a micro-notch and early crack propagation, N_{MSC} and N_{PSC} are the number of cycles spent on propagation of microstructurally small and physically small cracks, and N_{LC} is the cycles spent on long crack propagation. Microstructurally small and or physically small cracks can propagate at a higher rate depending on the applied stress level compared to linear elastic fracture mechanics (LEFM) compliant long cracks [8,9].

TABLE 1–*Fatigue fracture life (in cycles) of 7075-T6 aluminum alloy specimens.*[1]

S_a (MPa)	**$N_{f,1}$**	**$N_{f,2}$**	**$N_{f,3}$**	**$N_{f,4}$**	**$N_{f,5}$**	**$N_{f,6}$**	**μ_{Nf}**	**σ_{Nf}**
300 (25 Hz)	25699	26405	17107	31793	19487	18556	23174	5706
245 (25 HZ)	101814	98427	112008	95379	106503	76711	85688	12181
220(25 Hz)	151073	177641	112152	147642	167459	119460	145904	25845
190(25 Hz)	272378	179827	217966	246867	-	-	229259	39770
300 (10 Hz)	27410	34739	24586	20606	20931	24947	25536	5195

[1] Here, N_{fi} is the cycles to failure for i'th specimen at S_a stress level. μ_{Nf} is average cycles to failure and σ_{Nf} standard deviation for experiment set done at the particular stress level.

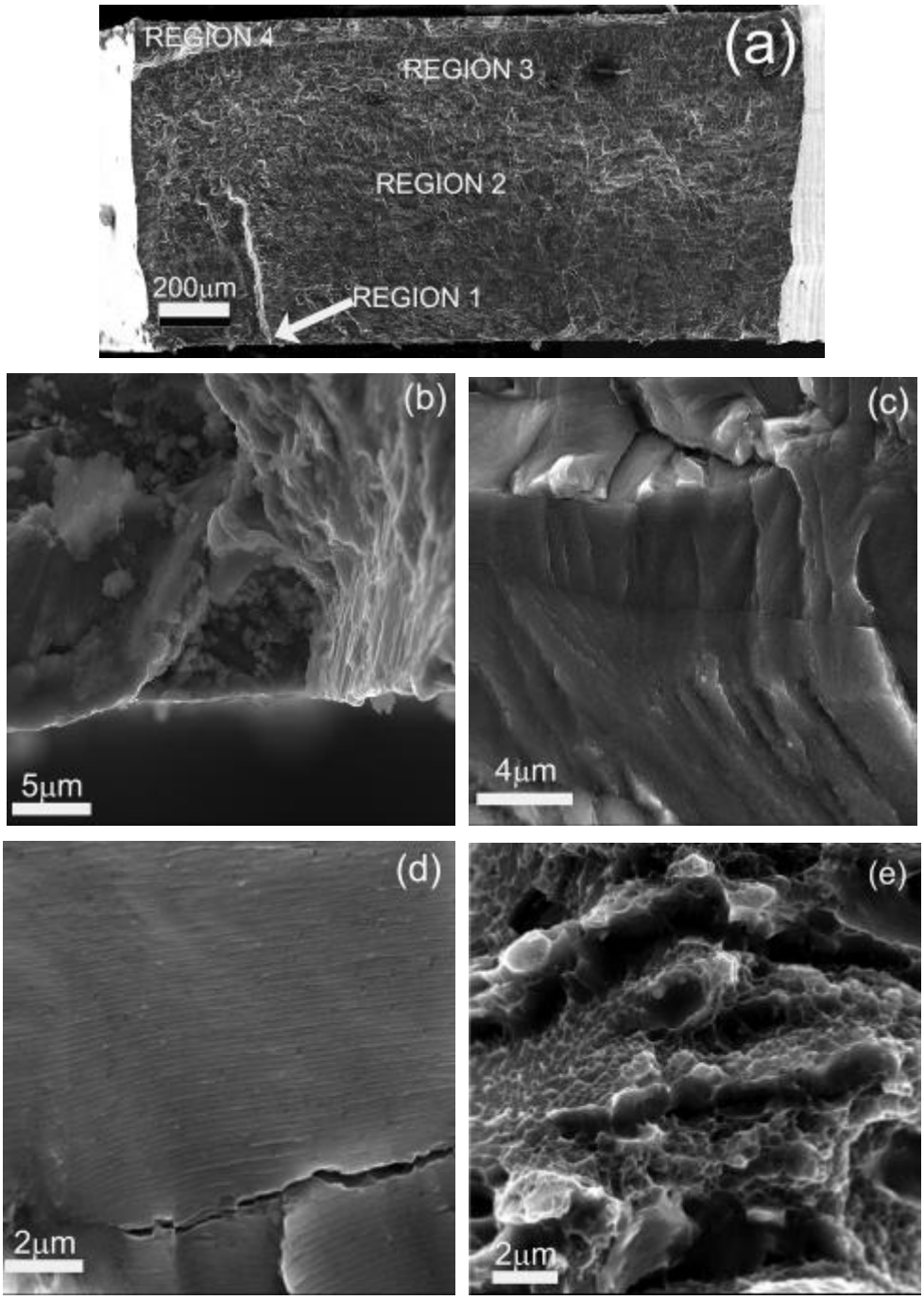

FIG. 3–*Sample SEM image of fracture surface for specimen tested at 220 MPa , 25 Hz. The horizontal specimen surface in this figure was non-milled, while the shorter edge was milled. Higher resolution images of Regions 1 – 4 show (b) crack initiation, (c) stage –I crack propagation, (d) stage – II crack propagation and (e) overload failure region.*

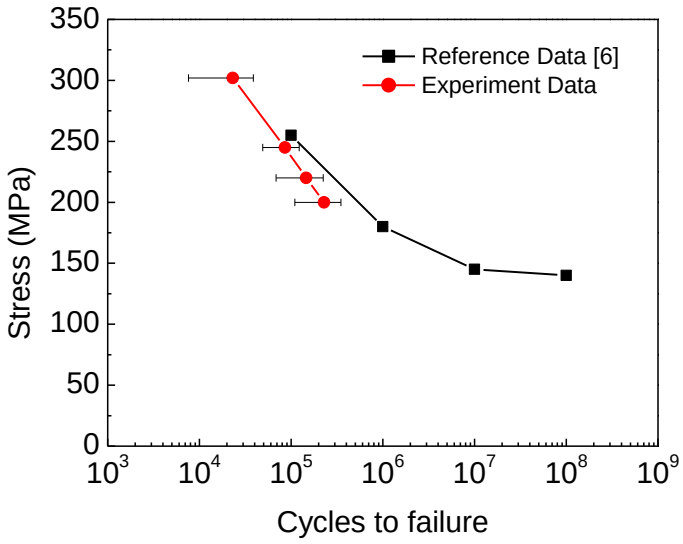

FIG. 4–*S-N curve of 7075–T6 sample tested. Current data are compared with the completely reversed bending fatigue life data from Ref. [6] at a 99% confidence level.*

Assuming that the number of cycles to incubate a fatigue crack does not change with specimen size, the total life cycle spent in the propagation of short crack (i.e. N_{MSC} and N_{PSC}) in sub-size samples would be lower because of the shorter dimension through which the short crack would grow. In addition, the N_{LC} part of the total fatigue life is expected to come down. Thus, these effects will reduce the total sample life. It may be noted that the physically small crack regime can extend from 300 to 800 μm [7], and thus can consume a substantial cross-section of the sub-size specimen. However, the fact that current results are in the same order of magnitude comparable to the results of standard specimens suggests that sub-size specimens can be useful for comparative investigations of fatigue life.

SUMMARY

A completely reversible fatigue test bed with sub-size specimen was developed to evaluate the S-N behavior of 7075-T6 aluminum alloy. Sub-size specimen design was a hybrid version of Krouse type test specimen as discussed in ASTM B593. The sub-size specimens gave

lower life compared to the handbook values, but can serve as a useful tool to generate comparative fatigue data.

Acknowledgements

The authors would like to gratefully acknowledge Professor K. Krishnamurthy and the REU team for putting together the mini-fatigue test bed and the financial support of the National Science Foundation under Grant Numbers EEC-0139117 for the REU program and DMI-0523022 for the undergraduate student supplement.

REFERENCES

[1] ASTM B593 -96 (Reapproved 2003) "Standard Test Method for Bending Fatigue Testing for Copper-Alloy Spring Materials," *Annual Book of ASTM standards*, ASTM International, West Conshohocken, PA, 2004.

[2] ASTM, Standard E468 -90 "Standard Practice for Presentation of Constant Amplitude Fatigue Test Results for Metallic Materials," *Annual Book of ASTM standards*, ASTM International, West Conshohocken, PA, 2004.

[3] ASTM Standard E739 -91 "Standard Practice for Statistical Analysis of Linear or Linearized Stress-Life(S-N) and Strain –Life(ε – N) Fatigue Data," *Annual Book of ASTM standards*, ASTM International, West Conshohocken, PA, 2004.

[4] Janssen, P.J.M., de Keijser, Th. H., Geers, M.G.D., "An Experimental assessment of grain size effects in the uniaxial straining of thin Al sheet with a few grains across the thickness," *Mater. Sci. Eng. A*, Vol. 419, 2006, pp. 238–248.

[5] Hyde, T.H., Sun, W., and Williams, J.A., "Requirements for and use of miniature test specimens to provide mechanical and creep properties of materials: a review," *Int. Mater. Rev.*, Vol. 52, 2007, pp. 213–255.

[6] Kaufman, J.G., *Properties of Aluminum Alloys*, ASM International, Materials Park, OH, 1999. p.297.

[7] Xue, Y., Mcdowell, D.L., Horstmeyer, M.F., Dale, M.H., and Jordan, J.B., "Microstructure – based multistage fatigue modeling of aluminum alloy 7075-T651," *Eng. Fract. Mech.* Vol. 74, 2007, pp. 2810–2823.

[8] Suresh, S., *Fatigue of Materials*, Cambridge University Press, Cambridge, UK, 1998, p. 542

[9] Leis, B.N., Hopper, A.T., Ahmed, J., Broek, D., Kanninen, M.F., "Critical review of the fatigue growth of short cracks," *Eng. Fract. Mech.*, Vol. 23, No. 5, 1986, pp. 883–898.

II. CHARACTERIZATION OF HIGH CYCLE FATIGUE BEHAVIOR OF A NEW GENERATION ALUMINUM LITHIUM ALLOY

P.S.De, R.S. Mishra, J.A. Baumann*

Center for Friction Stir Processing, Department of Materials Science and Engineering

Missouri University of Science and Technology, Rolla, MO 65409

*The Boeing Company, Saint Louis, MO 631666, USA

ABSTRACT

The high cycle fatigue life characteristics of an Al-Li alloy was studied as a function of microstructure. For the parent microstructure, fatigue life decreased with an increase in the grain size. No such effect was however noted at high stresses. This decrease in fatigue life was correlated to the lower crack initiation life arising due to small crack effect. Under multiaxial stress conditions, the alloy exhibited intergranular type of cracking. The cross-linking of intergranular cracks (in T8 condition) caused a further deterioration in fatigue life. Additionally, planar type of slip movements (in T3 condition) in stage-I crack propagation was observed. The slip planarity depended on both the sample texture and the nature of precipitates. Fractographic and textural evidence for this are presented.

Keywords: Aluminum alloys, Fatigue, Fracture

1. INTRODUCTION

The aluminum-lithium alloys constitute a promising group of metallic material – with prospective applications in the aerospace industry. This is chiefly due to its unique combination of low density and high strength. However, the microstructural complexity of these alloys with corresponding deleterious effects on mechanical properties has prevented its widespread use. Consequent research to improve mechanical properties has resulted in newer compositional modifications for this group of alloys. However, no detailed fatigue behavior evaluation for such new alloys exists in current literature. The present work therefore characterizes the high cycle fatigue and ductility behavior of a latest commercially available aluminum-lithium alloy. In the next subsection, a brief background on the precipitates formed in different Al-Li alloys is provided.

1.1 Precipitates in Al-Li alloys

In Al-Li alloys, precipitation hardening (PH) constitutes the principal strengthening mechanism; therefore, the nature and type of precipitates is an area of prime interest. Considering the Al-Li phase diagram first, binary Al-Li alloys consists of grain boundary δ (AlLi) phase with

coherent ordered δ' (Al_3Li) phase distributed within the matrix. Depending on the Li content, ternary Al-Cu-Li alloys are classified into two types. In the first type of alloy with low Li content, (e.g. Li - 1.15% and Cu - 5.15%), partially coherent θ' plates (transition phase of Al_2Cu), T_1 (Al_2CuLi) and T_B ($Al_{7.5}Cu_4Li$) are the principal strengthening phases [1]. For alloys with high Li (e.g. Cu - 2.7% and Li - 2.25%), θ', T_1 and coherent ordered δ' phases form. In ternary Al-Li-Mg system (e.g. Mg: 5.5%, Li 2%), incoherent Al_2LiMg and coherent δ' are the principal phases [1]. For Al-Li-Cu-Mg alloys, precipitation is similar to ternary Al-Cu-Li and is a function of its Cu:Li ratio. Thus, for low Cu:Li (<1.5) S' (Al_2CuMg), T_1 and ordered δ' are the principal precipitating phases [2, 3, 4]. At higher Cu:Li ratios (>2-3) precipitation is restricted to S' and T_1 phases only [2, 3, 4].

1.2 Effect of precipitates on slip and deformation characteristics

As already discussed, depending on the Al-Li composition, a wide variety of precipitating phases exist. This precipitate type variation significantly alters the dislocation slip mechanisms. Depending on slip band appearance or dislocation structure present (in transmission electron microscopy (TEM) experiments), slip in face centered cubic (f.c.c.) alloys is classified into two categories, a) wavy type and b) planar type. Thus for a wavy slip metal, slip bands exhibit a homogeneous structure. For planar slip situation a heterogeneous structure is observed [5]. The TEM observation of monotonically stretched wavy slip metal is characterized by dislocation bundles. While a multipolar dislocation structure with extended dislocation pileups have been noted for planar slip metals [6]. Although, the exact reason behind such differences are not understood at present, short range ordering and clustering are thought to be a determining factor in this regard [6]. Variables like stacking fault energy and yield stress (controlling screw dislocation annihilation distance) were deemed to be of secondary importance [6].

Thus, binary Al-Li alloy with coherent ordered precipitates (δ') exhibits a planar slip tendency [7]. The grain boundary second phase and precipitate free zones (PFZ) contribute to additional strain localization [7]. Such slip heterogeneities have been associated with a low fatigue crack initiation resistance [7]. Similarly δ' and grain boundary second phases (θ', T_1, T_2, β') reduce the fracture toughness values in a Al-Li-Cu-Zr alloy [8]. Identically, δ' precipitates present in Al-Li-Cu-Mg-Zr alloy of the low Cu:Li type, resulted in strain localization during low cycle fatigue [9]. Thus, planar slip in Al-Li alloys is associated with coherent ordered δ' phase and results in an overall degradation in property. As an exception, Khireddine et al [10] however envisaged that slip planarity induced crack bifurcation can result in improved fracture toughness values. Conversely, T/S phases present in Al-Li alloys promotes slip homogenization leading to a

wavy slip characteristics with improved mechanical properties [9]. Here, it needs to be added that as observed in this study, texture plays a critical role in enhancing this slip planarity. The effect have been discussed in more detail later in this paper.

1.3 Effect of texture on deformation during fatigue

The first detailed examination of texture (predominantly {110}<112> and {100}<011> type) and grain size effect on the cyclic stress strain (CSS) life of Al-Li-Cu-Mg alloys was done by Khireddine etal [10]. In this work, samples extracted from the surface of an extruded bar showed a lower CSS life compared to those machined from the core. This CSS life change with sample location was attributed to an increased {111} pole density in the surface samples compared to those from within the core [10]. An additional decrease in CSS life with sample orientation change (from the longitudinal to a transverse direction of rolling) was also reported. The variation was attributed to a grain size effect [10]. Similar deformation texture effect on AA2090 alloy caused a reduced high cycle fatigue life at an orientation 45˚ to the rolling direction [9].

1.4 Multiaxial stresses in bending fatigue

Practical loading conditions though multiaxial in nature, all cyclic deformation work on Al-Li alloys reported till date, were of the uniaxial type. Thus, understanding the effect of multiaxial stress states on Al-Li fatigue is of scientific and technological importance. Depending on the specimen used, multiaxial fatigue testing techniques are classified into two principal types, a) cruciform and b) thin walled tubular kind. Testing such standard multiaxial specimens is however associated with an elaborate equipment requirement. A simpler approach therefore would be to use a bending type fatigue specimen. The remaining part of this section discusses the nature of stresses in a displacement controlled fully reversed bending fatigue sample of the type used in this work [11].

From the structural viewpoint, a displacement controlled fatigue specimen [11] behaves like a cantilever beam bent under point loading (see Fig. 1) where b is the beam width at any section (ab = cd) and ‘h’ the thickness (ad = bc) which is uniform throughout the beam. The first order stress distribution for such conditions can be approximated as [12],

$$s_{11} = -\frac{6Pxy}{bh^3}$$
$$\sigma_y = 0 \qquad (1)$$
$$s_{13} = -\frac{6P}{bh^3}\left(\frac{h^2}{4} - y^2\right)$$

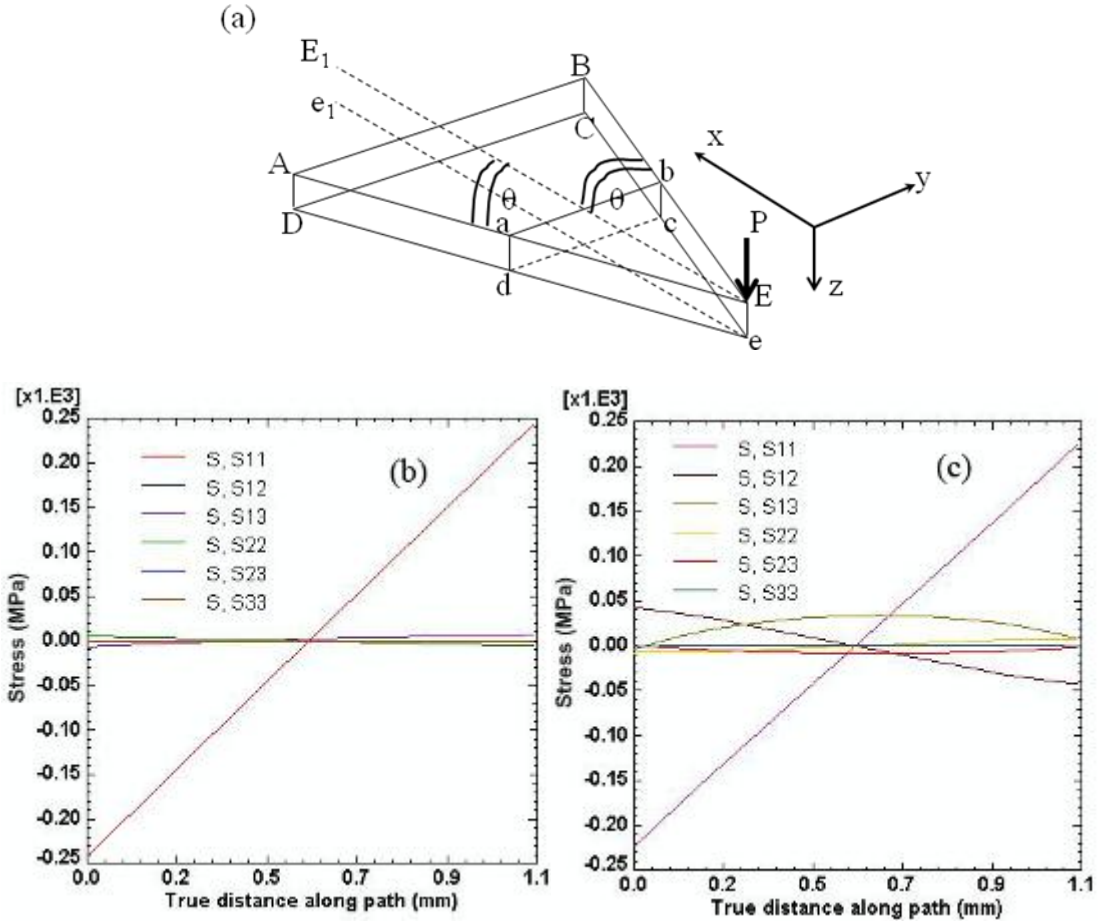

Fig. 1. (a) A schematic of the displacement controlled fatigue specimen under loading shown as a cantilever with a typical rectangular cross-section (abcd) tapering from the fixed end ABCD to the pointed end Ee. The beam possesses a bilateral symmetry along the plane EE_1e_1e. (b) Stress distribution along specimen thickness (1.15 mm) near specimen centerline (i.e. EE_1/ee_1 in Figure 3.1a) at 25N bending force as obtained by finite element simulation in ABAQUS©. (c) Stress distribution along specimen thickness (1.15mm) towards specimen edge (i.e. ad/bc in Figure 3.1a) at 25N bending force as obtained by finite element simulation in ABAQUS©.

Thus, for a bending fatigue sample, the tensile/compressive stress is highest at the sample surface and is zero at the mid-section (i.e. neutral plane). The shear stress (s_{13}) on the other hand is highest at the midsection, and is zero at the surface region. This fact can be utilized to study the effect of multiaxial stress states during fatigue. Here, it may be noted that the exact stress distribution will however vary significantly, depending upon the nature of load and sample dimensions used. A more accurate measure of the expected stress variation can be obtained by using the appropriate boundary conditions and sample dimensions in a finite element simulation. Fig. 1(b) and 1(c) show the stress distribution across thickness at different positions in the mini-fatigue specimen used in this work. The simulation results show that stress condition along the specimen centerline is similar to that of pure bending with s_{11} as the measurable stress. On the other hand, towards the specimen edge other than s_{11} and s_{13} an additional s_{12} component was predicted. These shear stresses will significantly affect the fatigue life as will be shown in the later part of this work.

In the preceding sections the sensitivity of fatigue property on the microstructural characteristics of Al-Li alloys has been highlighted. The development of new joining processes like friction stir welding/processing have introduced further complexities into this structure-property relationship. The current work explores the microstructural and stress state effects on the high cycle fatigue life of a latest generation Al-Li alloy and its friction stir processed variant.

2. EXPERIMENTAL DETAILS

The starting material was a 6.3 mm thick, rolled AA2098 alloy in T3 condition with base composition of Cu~3.5%, Mg~0.5%, Ag~0.4%, Li~1% and Zr~0.1% (hereafter called PA-T3). The original alloy plate aged at 160˚C for 19 hours (hereafter labeled PA-T8) and a friction stir welded (butt configuration) region (nugget portion only) of the PA-T3 alloy aged at 160˚C for 24 hours (henceforth referred as FSP-T5) were the two other microstructures used in this work. The three microstructures thus produced, were characterized using a combination of optical and orientation imaging microscopy (OIM). For OIM samples were mechanically polished to a final polish of 0.02 μm and examined with a hot field emission gun scanning electron microscope (FEI Helios Nanolab) equipped with Nordylys camera and HKL technology. Precipitate distribution assessment was done using scanning transmission electron microscopy (STEM) on focused ion beam lift-out samples. All fractography experiments in this study were conducted using a Hitachi 4700S cold field emission gun scanning electron microscope operated at 15 kV. To evaluate the tensile and fatigue properties of the three microstructures, in-house designed subsize test beds were used [11, 13]. Parallel slices from the plate surface (within 1.5 mm from the top) and central

region sectioned using a diamond saw were machined into subsize specimens using a computer numerically controlled milling machine. Similar subsize specimens were machined out from the nugget region of the friction stir welded plates (see Fig. 2). These subsize specimens were uniformly grinded and polished (1 μm finish) to 1 mm thickness for final testing.

3. RESULTS

3.1 Grain size and precipitates

The microstructure of the parent alloy reveals a typical pancake shaped rolled structure with grains elongated in the rolling direction. The transverse grain dimensions were significantly smaller compared to the longitudinal. Figure 2(a) represents the typical parent alloy microstructure (PA-T3 / PA-T8) in a three dimensional perspective. Another feature of the parent microstructure was the presence of occasional thick grains at regions near the surface (within one mm from plate surface). In Fig. 2(b) a typical OIM image of the friction stir nugget microstructure (FSP-T5) is shown. For the friction stir nugget sample (i.e. FSP-T5), grain size measurements were conducted at the mid-section of two different planes (A and B in Fig. 2(c)), one millimeter apart. No measurable grain size variation along this nugget depth was observed. In Table 1, a summary of grain size distribution for the three different microstructures as measured by linear intercept method is given.

To understand the nature of precipitates present, high angle annular dark field (HAADF) imaging of both PA-T3/PA-T8 microstructures were done (Fig. 3). The PA-T3 samples showed few circular precipitates. The PA-T8 microstructure on the other hand consisted of elongated needle shaped precipitates with incoherent equiaxed phases located at the grain boundaries. To ascertain the nature of precipitates, these micrographs were compared with an alloy of similar composition (Cu 3%, Li 1.6%, Mg.8%, Zr 0.2% and Al-balance) investigated by Crooks and Starke [14]. The PA-T3 structure in this work was analogous to the solutionized naturally aged structure reported by Crooks and Starke [14]. The circular precipitates in PA-T3 microstructure were thus identified as the β' (Al_3Zr) phase. The δ' precipitates however remained unresolved. Identically, the observed T8 microstructure (Fig. 3(b)) compared well with the T8 conditions of Crooks and Starke [14]. The needle shaped phase in Fig. 3(b) was therefore identified as the S' phase. The grain boundary phase observed in PA-T8 was probably a variant of the different T phases possible in Al-Li alloys [14].

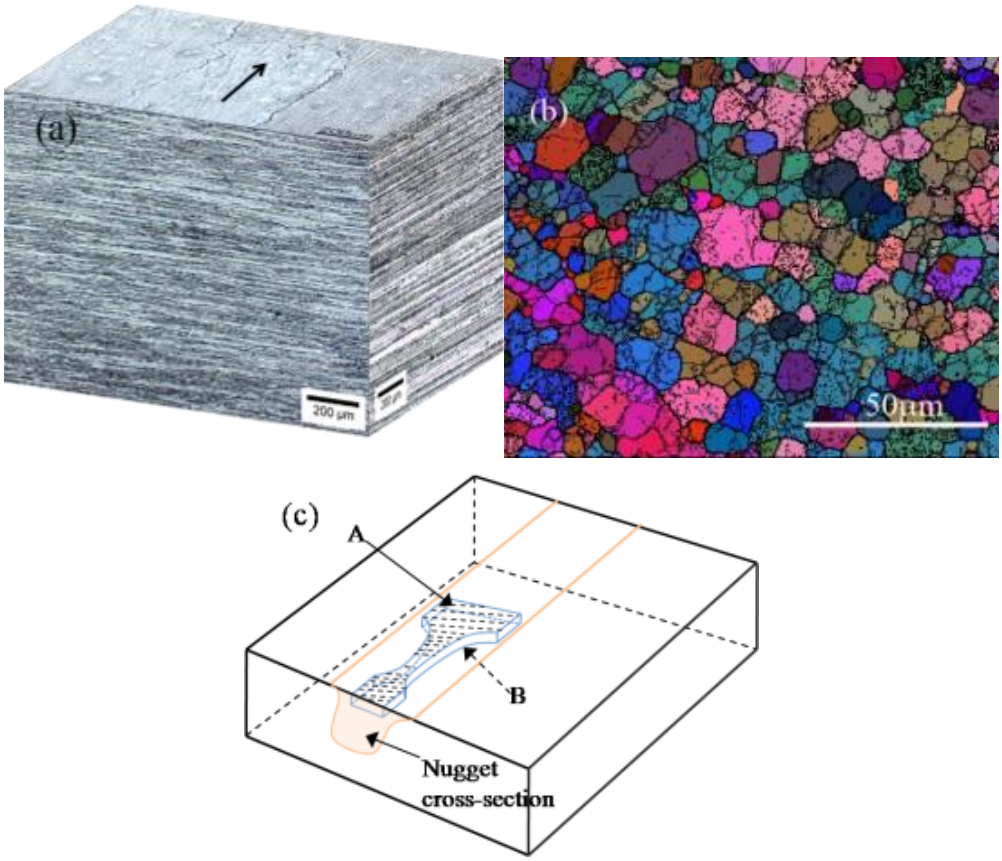

Fig. 2. (a) A three dimensional montage of the parent microstructure using optical microscopy; arrow shows the rolling direction. (b) Grain size distribution of the friction stirred microstructure as observed with orientation imaging microscopy using Euler angle coloring. Thick lines represents high angle grain boundaries (misorientation > 15˚) and the thin lines represents low angle grain boundaries (1˚< misorientation < 15˚). (c) Schematic illustration of friction stir processed zone, sampling plane positions A and B with respect to the weld surface.

Table 1 Grain size statistics for the three different microstructures of Al-Li used as measured by linear intercept method on OIM data.

Microstructure	Average grain size (μm)	Minimum grain size (μm)	Maximum grain size (μm)
PA-T3/ PA-T8	5.8	1.4	34.4
FSP-T6	6.05	0.5	29

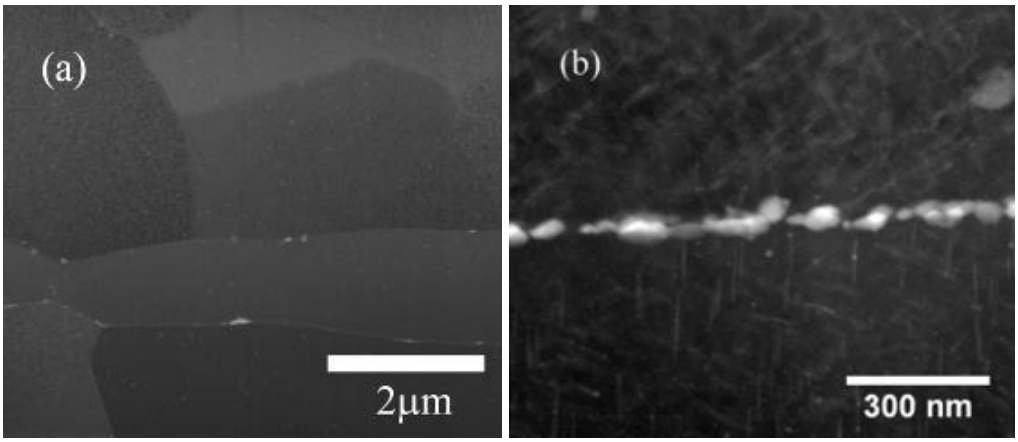

Fig. 3. HAADF-STEM images taken at 30 KV on FIB lift out samples (a) PA-T3 microstructure showing occasional small circular precipitates in the matrix along with sporadic precipitates at the grain boundaries. (b) PA-T8 microstructure with irregularly shaped particles on the grain boundaries and thin needle shaped precipitates located within the matrix.

3.2 Texture

The parent alloy (PA-T3/PA-T8) shows a strong rolling texture (Fig. 4), with the preferred orientation being a combination of different texture components including $\{112\}\langle 111\rangle(\text{Copper}-\text{type}), \{110\}\langle 112\rangle(\text{Brass}-\text{type})$ [15]. Thus, for both PA-T3 and PA-T8 microstructure a small fraction of the {111} poles were oriented at ~53˚ with the rolling direction (RD) while a higher fraction of the {111} poles were oriented at ~19˚with the RD (Fig. 4(a)). For the friction stir welded microstructure (FSP-T5) , texture data was obtained from a region parallel to the weld surface, the schematic position of which is shown (plane 'A') in Fig. 2(c). The results confirm a shear texture, similar to that reported earlier [16, 17]. The data obtained from parallel planes at different heights (at 1.0 mm difference) exhibited a similar pattern as shown in Fig. 4(b) indicating no change in texture within the friction stirred volume.

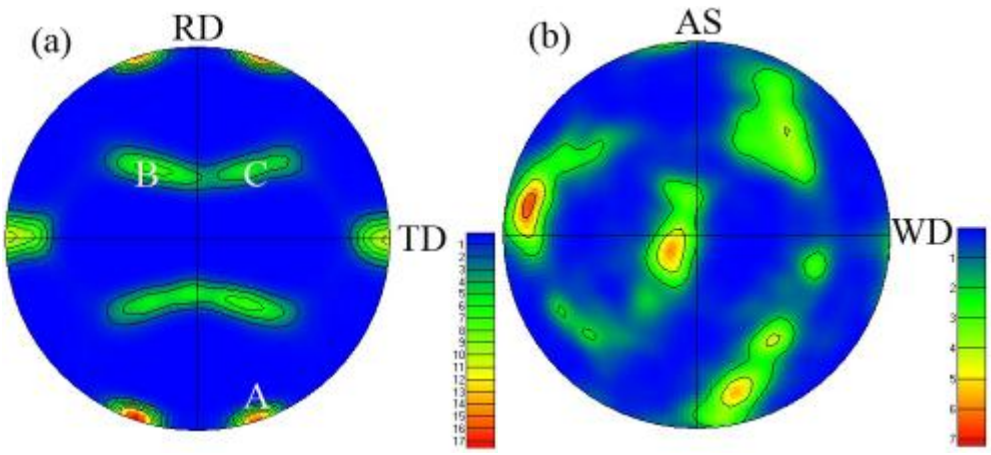

Fig. 4. (a) The 111 pole figure of the PA-T3/T8 microstructure, RD being the rolling direction and TD the transverse direction. (b) The 111 pole figure of FSP-T6 used, AS being the advancing side of tool and WD being the welding direction.

3.3 Tensile property

In Table 2 the strength and elongation values obtained from subsize tensile tests conducted on PA-T3, PA-T8 and FSP-T5 microstructures are summarized. No significant anisotropy in the tensile mechanical properties of FSP-T5 and PA-T8 microstructures was observed. However, for the PA-T3 microstructure a measurable directionality of strength and ductility was noted (Table 2). Another, remarkable feature of the PA-T3 microstructure was the absence of non-uniform elongation and necking for specimens oriented in the longitudinal direction (Fig. 5). This was unlike in PA-T3 samples of transverse orientation where a small, but definite non-uniform elongation was recorded (Fig. 5(a) and 5(c)). It may be added here that for both PA-T8 and FSP-T5 microstructure, an extended non-uniform elongation zone was observed.

3.4 High cycle fatigue life

As mentioned in Section 3.1, a significant heterogeneity in the PA-T3 and PA-T8 microstructures (occasional large grains near the surface of the rolled sheets) was observed. To accurately estimate the fatigue property, the parent sheet was therefore divided into two subcategories depending on the depth of sample location from the plate surface. In the first subcategory, fatigue samples in transverse or longitudinal directions were machined from the center region where grains were finest and had the distribution given in Table 1 (abbreviated as

PA-T3 and PA-T8, L/T where L/T indicates longitudinal /transverse orientation). The second subcategory constituted of samples machined from the top one mm region of the plate surface (PAS-T3 and PAS-T8 L/T) where larger grains were observed. Additionally, to understand the effect of stress multi-axiality on fatigue life, samples of thickness 1.15-1.2 mm (from both PA-T3 and PA-T8 microstructures) were also tested (abbreviated as PA/PAS – T3/T8 – thick). In Fig. 2(c) the location of fatigue samples for FSP-T5 microstructure is shown. A summary of the variation in fatigue life for the different microstructures used in this study is shown in Fig. 6. The fatigue life variation for PA-T3 microstructure shows a level of scatter typically observed in commercial aluminum alloys. Thus, an order of magnitude difference in fatigue life was observed at low stress amplitudes, the scatter decreasing at higher stress levels (Fig. 6(a)). Perceptible difference in fatigue life with PA-T3 sample orientation was also noted.

Table 2 Summary of tensile test property of the different microstructures measured using subsize specimens [12].

Microstructure	$\sigma_{YS}(MPa)$	$\sigma_{UTS}(MPa)$	$\varepsilon_u(\%)$
PA-T3, longitudinal	327 ± 2	457 ± 2	12 ± 1
PA-T3, transverse	294 ± 7	417 ± 1	14 ± 1.4
PA-T8, longitudinal	540 ± 14	575 ± 17	7 ± 2
PA-T8, transverse	528 ± 8	556 ± 7	7 ± 0.5
FSP-T5, longitudinal	371 ± 5	443 ± 1.5	8 ± 1
FSP-T5, transverse	382 ± 1.5	445 ± 1.4	9 ± 1

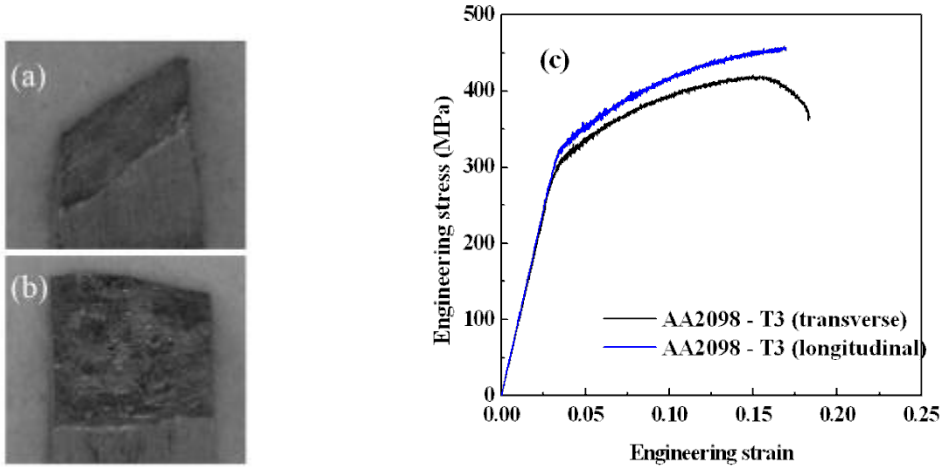

Fig. 5 (a) Fracture surface of 2098-T3 tensile specimen in transverse orientation. (b) Fracture surface of 2098-T3 tensile specimen in longitudinal orientation. (c) The tensile stress strain curves of 2098-T3 specimen in transverse and longitudinal orientations.

Thus, PA-T3 (T) samples showed a better fatigue life compared to PA-T3 (L) samples irrespective of the sample thickness tested. However, for PAS-T3 (T) samples a reduction in fatigue life at low stresses was observed. Compared to PA-T3 microstructure the overall scatter in fatigue life for PA-T8 microstructure was higher. The life varied approximately half an order of magnitude at high stresses to almost two orders at lower stress levels (Fig. 6(b)). Thus, PA-T8 (L) samples showed a better fatigue life irrespective of the sample thickness, while PA-T8 thick (T) samples showed a poor fatigue life. A maximum decrease in the fatigue life was observed for PAS-T8 (L), PAS-T8 thick (T) and PA-T8 thick (T) samples. Due to such high fatigue life scatter, a more effective representation of the S-N curve for PA-T8 microstructure can be given in terms of the two separate S-N curves as shown in Fig. 6(c). Thus, although the median fatigue life for PA-T8 microstructure was high, the overall fatigue performance of PA-T8 was comparable to that of PA-T3 and FSP-T5 microstructures.

3.5 Fracture surface morphology

The fracture surface morphology (Fig. 6) of the three different microstructures used in this study exhibits the characteristic three stage crack propagation typical of face centered cubic

metals [18]. However, subtle differences between the three different microstructures at each individual stage were visible. Consider the PA-T3 type of specimens first. The stage-I crack propagation of PA-T3 (L) samples was distinguished by extended inclined smooth fracture surfaces (Fig.6(a)) oriented at an angle of 30 ± 2˚ with the direction of rolling (Fig.6(e)). The fracture in PA-T3 (T) samples were however different, with the inclined smooth surface typical of PA-T3 (L) samples limited to a much smaller zone (Fig. 6(b)). The fracture surface corresponding to stage-I crack propagation in PA-T8 specimens on the other hand showed a crystallographic type of crack propagation with prominent ridges and plateaus (Fig. 6(c)). In some instances tire tracks pointing in the crack propagation direction were also observed (Fig. 6(f)). The stage-I crack propagation zone of FSP-T5 samples appeared different from both the PA-T3 and PA-T8 samples (compare Fig. 6(c) and 6d). The nature of crack propagation was more tortuous compared to the faceted structures appearing in the PA-T3/PA-T8 samples.

Another important aspect observed during fatigue fracture was the tendency towards extended de-lamination in both PA-T3 and PA-T8 microstructures (Fig. 7). The de-lamination cracks were oriented in a direction complementary to the loading axis. In all cases, these de-laminations occurred along the boundary of two fracture surface facets indicating a typical intergranular type of failure. Although such extended de-lamination cracking was not observed in the FSP-T6 specimens, small cracks in between the fracture facets were visible particularly in the stage-I region. An additional feature observed in PA-T8 samples, was the interlinking of de-lamination cracks at regions midway between surface and center of fatigue specimens (Fig. 7(b)). This feature was particularly noted in PAS-T8 thick (T), PA-T8 thick (T) and PAS-T8 (L) samples and was accompanied by a maximum reduction in fatigue life.

The stage-II crack propagation region in PA-T3 (L/T) samples showed coarse striation marks accompanied by extensive tears along crack propagation plane (Fig. 8). For PA-T8 specimens, the striation spacing however varied between both fine and coarse (compare Fig. 8(c) and 8d). Additionally, the extent of tearing on crack propagation plane for PA-T8 microstructure was significantly lower compared to the PA-T3 microstructure (compare Fig. 8a to 8d). In FSP-T5 specimens, the striations appeared to be more restricted and localized in nature (Fig. 8e) with reduced crack plane tearing. The stage-III crack propagation zone in all microstructures, were similar in nature and were typical of failure by void growth.

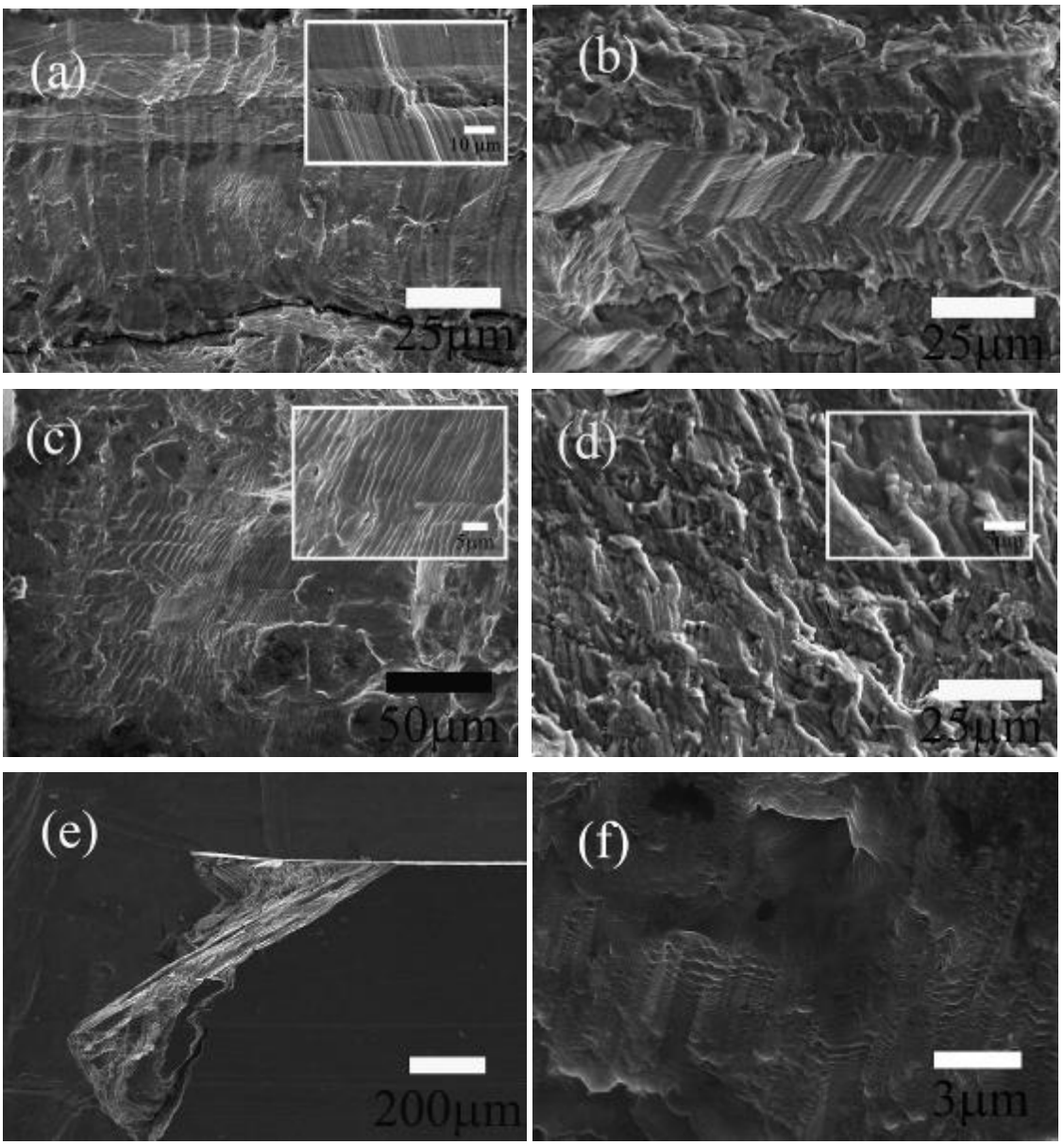

Fig. 6. Typical stage – I crack propagation characteristics for various specimens: (a) PA-T3 in longitudinal with inset showing the details. (b) PA-T3 in transverse direction. (c) PA-T8 longitudinal / transverse with inset showing regular shape ridge like features in details. (d) FSP-T5 in weld direction with irregular ridges formed. (e) The inclined stage –I crack propagation in PA-T3 samples oriented in longitudinal direction. (f) Tire tracks in a PA-T8 sample.

4. DISCUSSION

As already noted, the fatigue property of PA-T8 microstructure shows a wider scatter compared to PA-T3 samples. The FSP-T5 samples on the other hand show a mean fatigue life which is similar to the PA-T3 microstructure. Significant differences in the microstructure and fracture surface appearance were also noted. In the following sections the effect of microstructure and stress states on the fatigue life has been discussed in more details.

4.1 Fatigue crack propagation and nature of slip

As already discussed in Section 3.3, the PA-T3 tensile specimens oriented in longitudinal direction exhibited no non-uniform elongation. This was unlike the transverse orientation samples where a small but definite non-uniform elongation was observed. Non-uniform elongation in tensile specimens is associated with a tri-axial state of stress with slip occuring on multiple crystallographic planes [19]. Therefore, the lack of non-uniform elongation in longitudinal PA-T3 samples signifies a localization of dislocation movement in specific slip systems.

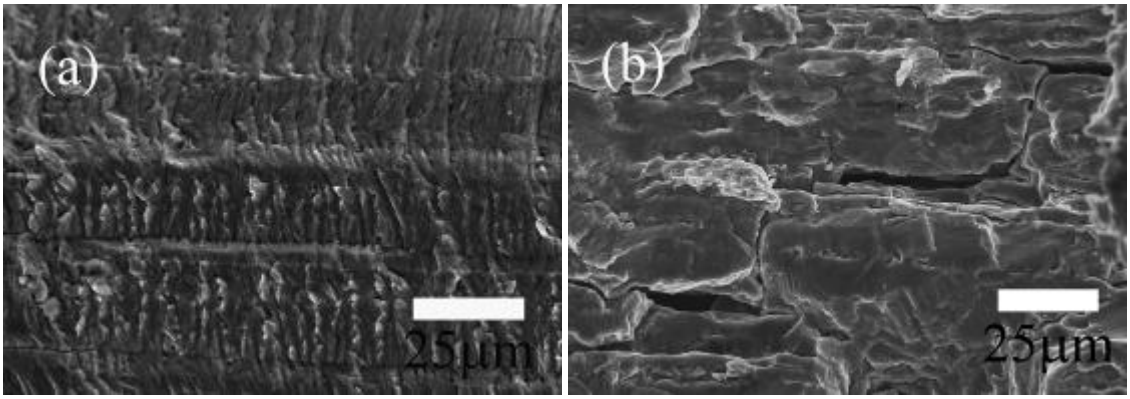

Fig. 7. De-lamination and the effect of stress amplitude on (a) PA-T3 microstructure in transverse direction at 170 MPa showing de-laminated region between the regularly spaced fracture surface facets. (b) PA-T8 (thick) microstructure in transverse direction at 209 MPa showing de-laminated regions which have joined together to form extended intergranular type of cracking.

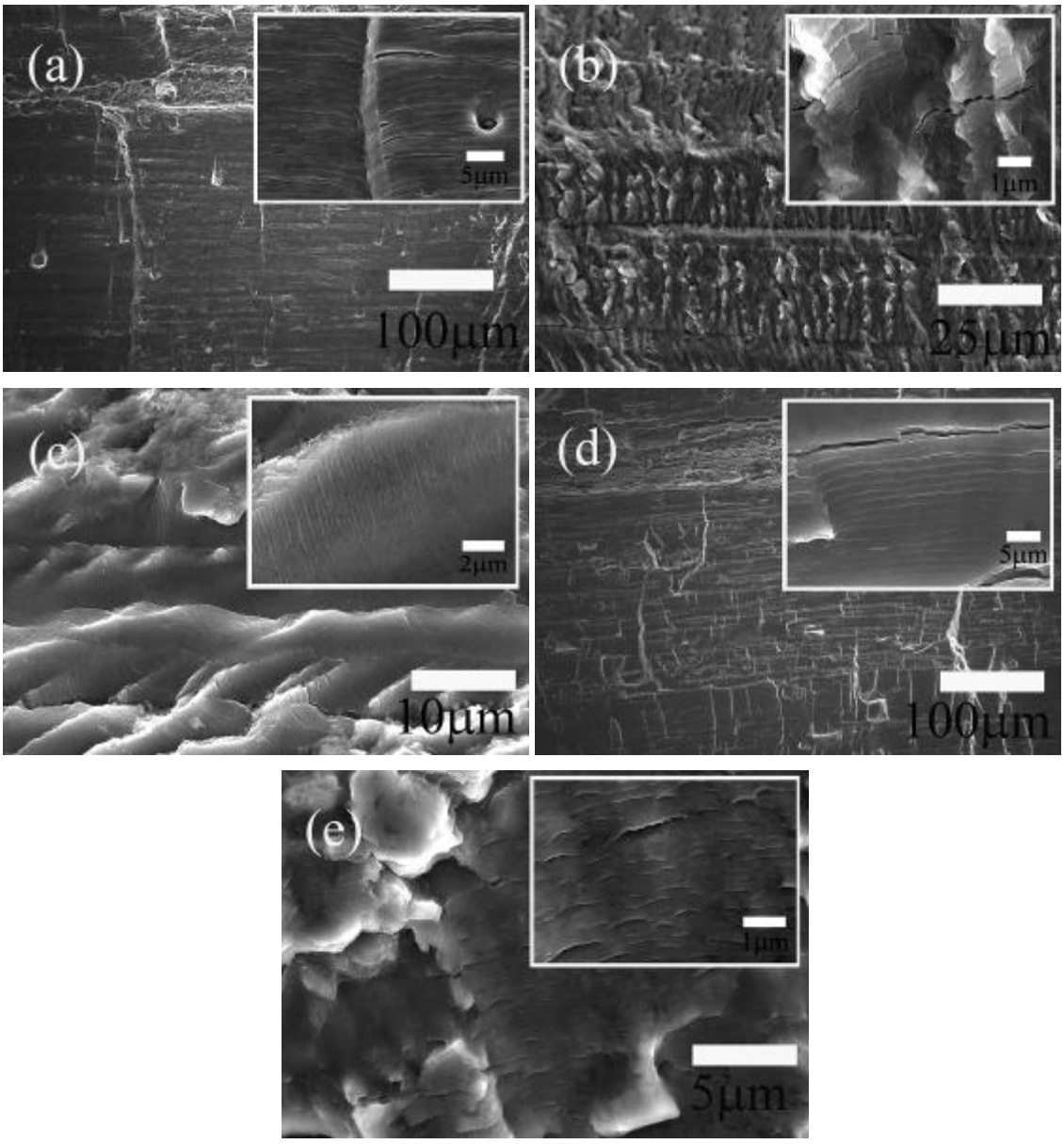

Fig. 8. Stage-II crack propagation in (a) PA-T3 sample in the longitudinal direction. (b) PA-T3 sample in the transverse direction. (c) PA-T8 sample in the transverse direction. (d) PA-T8 sample in longitudinal direction. (e) FSP-T6 sample.

In fact, such localization of slip occurred even in PA-T3 (L) fatigue samples in the crystallographic crack propagation regime. The smooth (Fig. 6(a)), inclined (Fig. 7(e)) crack propagation in PA-T3 (L) samples compared to the random crack propagation in PA-T3 (T)

samples (Fig. 7(b)) illustrates this differences in slip. To understand the issue further, the interaction between PA-T3/PA-T8 texture, precipitate and loading direction needs detailed consideration.

Considering {111}<110> as the active slip system, tensile forces acting along a given direction will cause shear stresses on the (111) plane. The magnitude of this shear stress is determined by its corresponding Schmid factor. For parent microstructure specimens with loading axis aligned in rolling direction, this Schmid factor value varied between 0.395-0.425 (Fig. 9). In contrast, for specimens in transverse orientation the Schmid factor value showed a uniform distribution varying between 0.285-0.45 (Fig. 9). The high Schmid factor value combined with continuous reduction in critical resolved shear stress (CRSS) of (111) planes due to shearing of coherent ordered δ' precipitates is expected to cause planar slip movement in PA-T3 (L) samples [6].

Consequently, crack propagation in PA-T3 (L) samples was expected to progress along (111) planes oriented at an angle of ~20˚ with the rolling direction (Fig. 6(e)). This crack plane inclination deviates by ~10˚ from the expected inclination for the (111) plane corresponding to pole position A (Fig. 4(a)). Such deviation (~3 to 10˚) from the close packed slip plane has previously been reported in the crystallographic studies on fracture surface facets for specimens in L-T orientation for Al-Cu-Li alloys with δ' precipitates [20]. On the other hand, the low Schmid factor values in PA-T3(T) specimens were expected to reduce the shearing of δ' phase substantially. Consequently, other {111}<110> slip systems gets activated resulting in a random stage-I crack propagation. An important point is that, despite having a texture similar to the PA-T3 microstructure, fatigue crack propagation in both PA-T8 (L/T) specimens remained random and homogeneous. This clearly indicates that precipitate nature (non-shearable) plays a key role in determining the crack propagation characteristics of the investigated Al-Li alloy [6]. The needle shaped S' phase present in PA-T8 specimens will promote a more uniform slip dispersion among the {111}<110> slip systems. Consequently PA-T8 (L/T) specimens exhibits, a random crack propagation irrespective of their orientation.

The wavy stage-I fracture surface characteristics of FSP-T5 samples can be ascribed to the effect of grain aspect ratio and precipitates present. The smaller effective grain size of FSP-T5 (Table 1) increases the nucleation stress required to generate dislocations from grain boundaries compared to the coarser parent microstructure [21]. The increased nucleation stress combined with resistance to slip due to precipitates present (similar to that of PA-T8) restricts the overall dislocation movement in FSP-T5 specimens. Consequently, a more tortuous crack movement in the stage-I regime was observed. Reverting back to the stage-II crack propagation characteristics;

an increased incidence of tearing on striation planes of PA-T3 (Fig. 8(a) and 8(b)) samples compared to both PA-T8 and FSP-T5 was observed. Considering the alternating slip model for stage-II crack growth [22], such crack plane tearing indicates a stress concentration on close packed slip planes. For PA-T3 (L/T) samples the ordered precipitates (δ') present will resist the to and fro dislocation movement equally during stress reversals. In the case of PA-T8/FSP-T5 samples the situation is however different. For both microstructures, S' the principal hardening phase strengthens the matrix by dislocation interaction with the stress fields [23]. Any dislocation movement across the particles (e.g. during tension cycle) destroys this stress field. Consequently, reverse dislocation movement (compressive cycle) becomes easier (Bauschinger effect) [18, 23]. Thus, localized stress concentration in PA-T3 samples is easier compared to the PA-T8/PA-T3 microstructure. The detailed fracture surface analysis presented above therefore indicates a close relationship between texture and precipitate nature on stage-I/II crack propagation. In the next section, the effect of crack propagation on fatigue life for the three different microstructures and their interaction with grain size is discussed in more detail.

4.2 Fatigue life: crack propagation and grain size effect

As already discussed in Section 3.4, fatigue life of PA-T3 samples oriented in longitudinal direction showed a reduced fatigue life compared to the transverse irrespective of sample thickness tested. To understand the reason behind this decrease, the nature of stage-I fatigue crack propagation for PA-T3 samples is now considered. As already indicated fatigue crack propagation in PA-T3 (L) samples was influenced by texture/precipitate and occurred along definite crystallographic plane. On the other hand, the PA-T3 (T) samples showed a rough fracture surface indicating crack propagation along multiple slip planes. The limited crack deflection and crack face asperities in PA-T3 (L) samples (compared to PA-T3 (T)) leads to a decreased roughness induced crack closure [18]. Consequently, a reduction in stage-I fatigue life for PA-T3 (L) samples was expected. The slight reduction in fatigue life for PAS-T3 (T) samples can be correlated to the effect of grain boundaries on the rate of crack growth. In high cycle fatigue, grain boundaries are known to act as a barrier to crack propagation particularly at the initial stages of crack propagation [18]. This retardation in crack growth rate results in improved fatigue endurance which is given as [24],

$$\sigma_{th} = \sigma^{*}_{fr} + \frac{K_c^{m}}{\sqrt{(\pi/2)d_g}} \qquad (2)$$

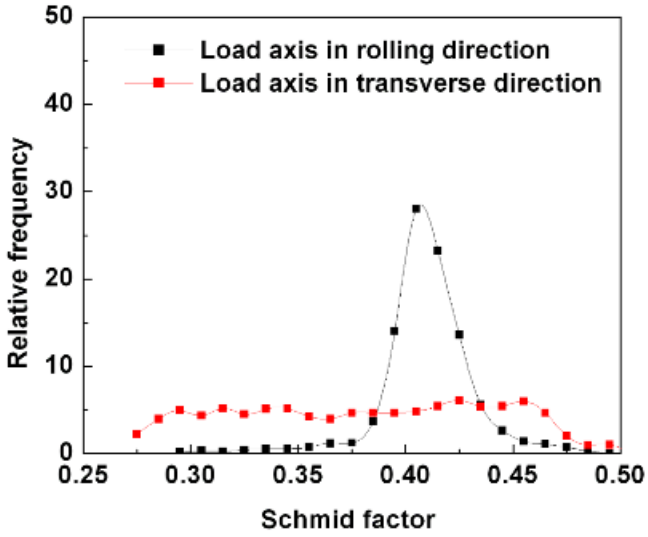

Fig. 9. The Schmid factor distribution for {111}<110> slip in PA-T3/PA-T8 specimen with load axis oriented in rolling/transverse direction. The results are from an OIM data acquired over an area of 660*525 μm^2.

where σ_{fr}^{*} is the friction stress for dislocation movement, K_c^m is the microscopic stress intensity factor and d_g is the grain size. Thus, for larger grained PAS-T3 (T) samples, the rate of crack propagation (Stage-I) will be higher compared to PA-T3 (T) specimens of smaller grain size as the sheet surface consisted of occasional large grains almost half an order of magnitude higher than the average grain size. Although the specific processing details of the Al-Li alloy used in this study is unknown, the microstructure clearly indicates the occurrence of abnormal grain growth near the surface. Abnormal grain growth is generally known to occur in metals where normal grain growth is suppressed [15, 25]. Considering the presence of Al_3Zr particles (to prevent grain growth/ recrystallization) abnormal grain growth can therefore be a matter of concern for the Al-Li alloy studied.

Unlike PA-T3, for PA-T8 samples fatigue life was highest for both PA-T8 (T)/PA-T8 (L) specimens irrespective of the sample orientation. In fact, considering the similar slip and stress-strain characteristics of PA-T8 samples (Table 2) a change in fatigue life with orientation was not expected. The improved fatigue life was therefore associated with an increase in crack deflection and fracture surface asperities due to the nature of precipitates present. On the other hand, a significant decrease in fatigue life was observed for PA-T8 thick (T) compared to PA-T8 thick

(L) specimens for stresses below ~250 MPa. The extensive intergranular cracking observed in PA-T3 thick (T) samples (Figure 3.8b) indicates that grain boundary weakness contributed to this decrease in fatigue life. Another interesting feature was the similarity in fatigue life for PAS-T8 (L) and PAS-T8 thick (T) specimens with PA-T8 thick (T) samples. The inherently weaker grain boundary of PA-T8 microstructure catalyzed by other microstructural features was therefore suspected to be a principal reason behind this fatigue life decrease. In the next section this broader role of microstructure and de-lamination effect on the HCF life of Al-Li alloys is discussed in more details.

4.3 De-lamination tendency

As already mentioned, in both PA-T8 and PA-T3 microstructures (Fig. 7a and 7b) a de-lamination tendency was observed, the severity being more apparent in PA-T8 microstructure. These de-laminations occurring at the grain boundary regions resulted in an inter-granular type of cracking for PAS-T8, PA-T8 (T) and PA-T8 thick (T) samples. To understand this issue further, the interaction between stresses in a displacement controlled bending fatigue test and microstructural features needs further consideration. As noted earlier, the PA-T8 microstructure consisted of extensive grain boundary precipitates which were incoherent in nature. These incoherent precipitates will act as regions of discontinuity and can significantly affect the stress distribution in a bending fatigue specimen. Depending on the grain orientation in specimen this crack like effect due to precipitate will vary considerably. Thus, for specimens with transverse orientation, the length of this discontinuity is longer compared to longitudinal specimens with corresponding increase in the stress concentration. An estimate of the stress can be made by assuming a continuous grain boundary precipitate along the grain surface. Such a grain can be approximated as elliptical holes of depth equal to grain intercept length across thickness. The dimension of the ellipse approximated to the longitudinal and transverse dimension of a grain. Thus, an elliptical hole of major axes length 250 μm and minor axes 100 μm, in a uniform rectangular solid can approximate the stresses generated in a PA-T8 specimen (Fig. 11 and 12). The distribution of forces on the rectangular solid was chosen such that, the resultant stress tensor on surface of interest (i.e. A_1) was similar to the stress generated inside the bending fatigue specimen. In Fig. 10, the forces applied on a sample without any hole and the corresponding stresses generated at the sample center along X (Path: 1) and Y (Path: 2) directions are shown. It can be noted that the stresses generated were similar to that predicted at the tension side of a 1.15 mm thick bending fatigue sample subjected to 25N load (Fig. 1(e)). In order to simulate the stress state in a PA-T8 (T) specimen, an elliptical hole was inserted on face A_1 as shown in Fig. 11(a).

The stresses generated around the elliptical hole in X (Path-1 values in Fig. 11b) and Y directions (Path-2 values in Fig. 12(c)), on application of forces similar to Figure 3.11a, are shown in Fig. 12(b) and 12(c). The results show that grain boundary precipitates in a sample with transverse orientation creates a s_{11} stress concentration which is 1.6 times higher than that in Fig. 10(b) and 10c). The corresponding stress distribution for a PA-T8 specimen with longitudinal orientation is shown in Fig. 12(b) and 12(c). As it may be noted, a significant difference in the distribution exists between transverse and longitudinal specimens. Thus, for PA-T8 (T) specimens a stress concentration is noticed at both the sharper (Point A in Fig. 12(a)) and flatter surface (Point B in Fig. 11(a)) of the ellipse. On the other hand, for PA-T8 (L) specimens the stress concentration is observed at the sharper surface (Point B in Fig. 12(a)) only. A significant increase in s_{13} magnitude is also noticed at position B for both the transverse and longitudinal specimens. The increased s_{11} stress concentration at A and B coupled with s_{13} increase at B for PA-T8 (T) sample is expected to cause easier crack propagation compared to PA-T8 (L) specimens. Consequently, for PA-T8 thick (T) specimens fatigue crack propagation due to intergranular cracking is easier than PA-T8 thick (L).

The absence of fatigue life difference for PA-T8 (T) and PA-T8 (L) specimens probably indicates that a criticality in terms of the stress concentrations exists. It may be mentioned here that for proportional forces applied according to equation (1), FEA simulations shows no difference in peak stress distribution for a 1 mm and 1.15 mm specimen. However, the stress distribution gradient in a 1.15 mm sample will be smaller. This will increase the sample volume under stress concentration. In other words, fatigue life difference between PA-T8 (T) and PA-T8 thick (T) is probably a sample size effect.

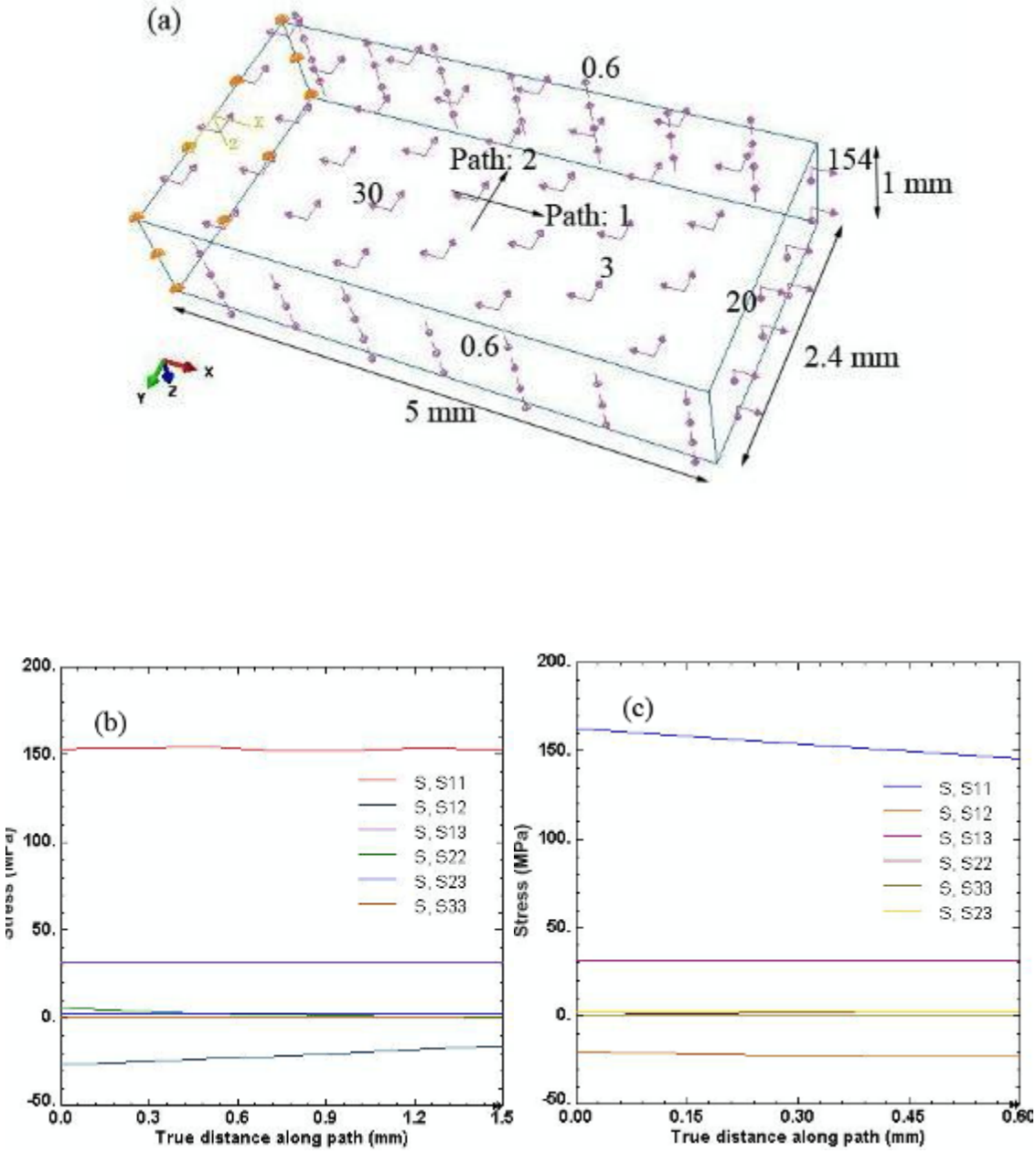

Fig. 10. (a)The forces applied on a rectangular cross-section simulating the stresses generated in the bending fatigue samples on the top surface. The in-plane arrows indicate shear forces while out of plane arrows indicate axial forces. The dimension of the solid section shown are in mm's. The numbers by the side of each arrow indicates the magnitude of force applied in Newtons. (b) The overall stress distribution along Path: 1 shown in Figure 10a. (c) The overall stress distribution along Path: 2 shown in Figure 10a.

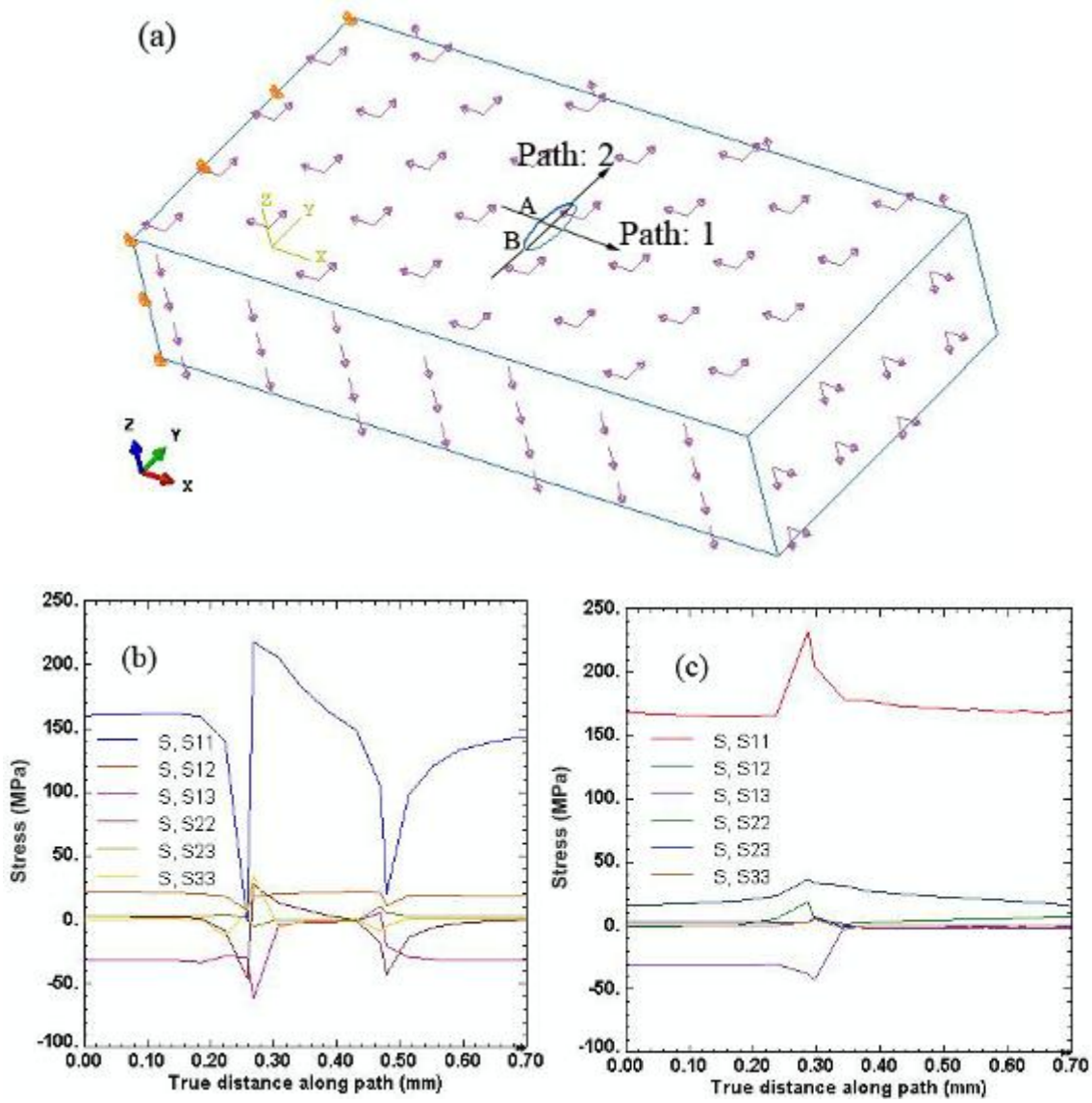

Fig. 11. (a) Simulation condition for PA-T8 bending fatigue specimen in transverse orientation. The forces applied are same as in Figure 10a. (b) The stresses generated along Path:1 in Figure 11a. (c) The stresses generated along Path: 2 in Figure 11a. Note, the stress concentration points generated compared to Figure 11b and 11c.

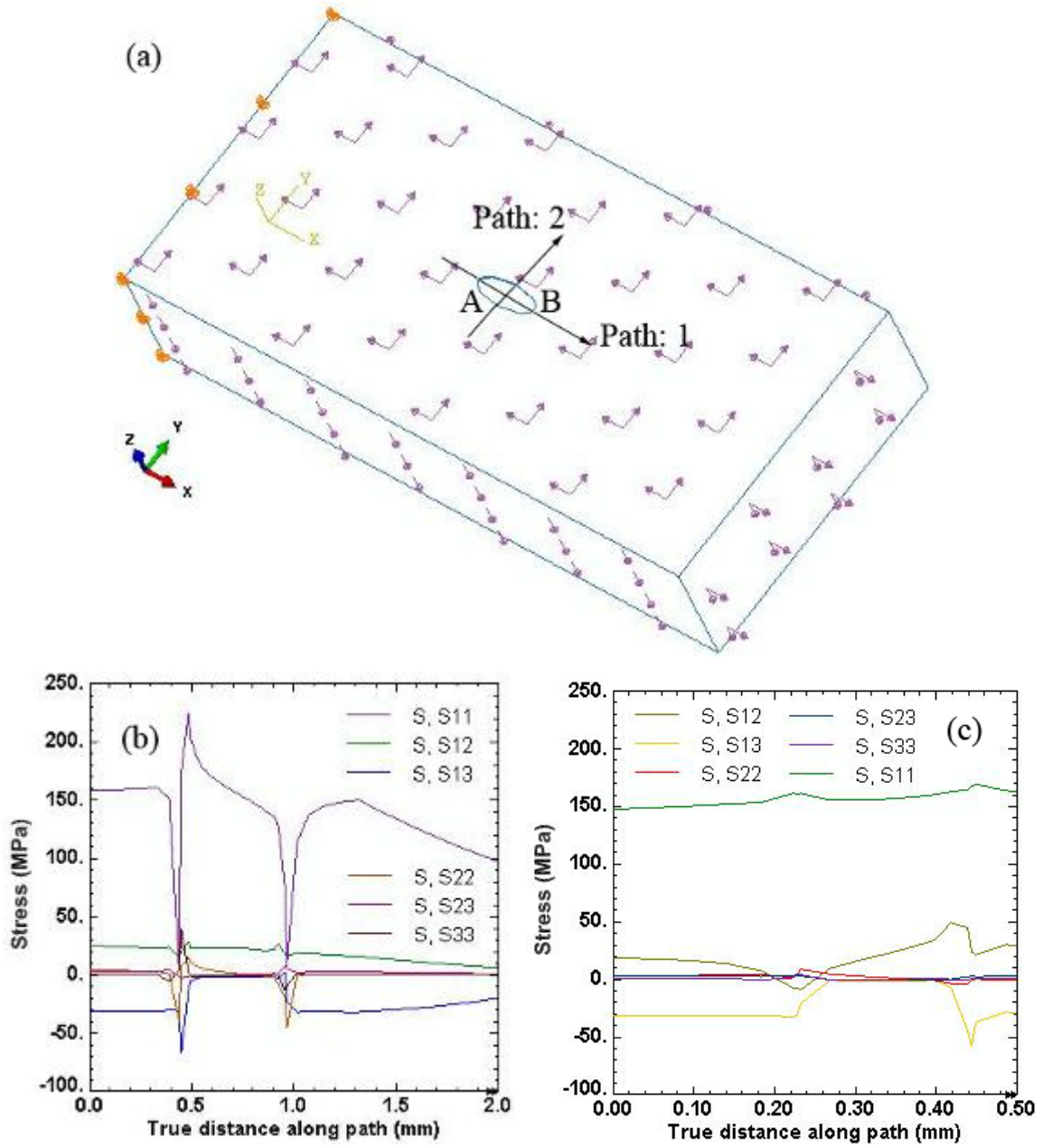

Fig. 12. (a) Simulation condition for PA-T8 bending fatigue specimen in longitudinal orientation. The forces applied are same as in Figure 11a. (b) The stresses generated along Path:1 in Figure 12a. (c) The stresses generated along Path: 2 in Figure 12a. Note, the stress concentration points generated compared to Figure 11b and 11c.

5. CONCLUSION

1. A rolled Al-Li-Cu-Mg-Zr-Ag system with Cu:Li ratio greater than 2.5 was studied. In T3 condition, tensile stresses in rolling direction causes planar slip. The effect being initiated by the presence of ordered coherent δ' phase coupled with a favorable rolling texture. This results in stage-I propagation where the fracture surface is parallel to the {111} planes.
2. For T3 alloy stressed in transverse direction the effect of planar slip on fracture surface orientation was nominal. Similarly, no effect of texture on crack propagation was observed for the T8 alloy. This has been ascribed to the slip dispersion caused by the needle shaped S phase precipitates accompanied with a Schmid factor effect. The FSP-T5 microstructure had a shear texture but do not show any texture effect on stage-I crack propagation
3. An effect of grain size on the high cycle fatigue life for both T3andT8 microstructure was observed. For T3 condition, at stresses below 200 MPa, samples from sheet surface containing large grains showed lower life. For T8 condition, the effect was observed up to 250 MPa. Above these stress limits, both T3 and T8 microstructure show limited effect of grain size on fatigue life. For samples from internal regions of the sheets the fatigue life was consistently high compared to the surface samples. The effect has been ascribed to the effect of grain size on crack propagation in stage -I. The FSP-T5 microstructure shows a fatigue life similar to that of the T3 heat treated condition.
4. A tendency for de-lamination was observed in both T3 and T8 conditions. The de-lamination led to intergranular type of fracture under multi-axial conditions. The effect was particularly noticeable in T8 samples. This has been attributed to the presence of grain-boundary second phase of Al-Cu-Li type, causing grains to behave as stress raisers. The fatigue life reduction in both T3 and T8 surface samples as discussed in point-3 is accentuated by this de-lamination tendency.

REFERENCES

[1] N.A.Belov, D.G. Eskin, A.A. Aksenov. Multicomponent Phase Diagrams: Applications For Commercial Aluminum Alloys, First ed., Elsevier, 2005.

[2] T.H.Sanders, E.A.Starke. Overview Of The Physical Metallurgy In The Al-Li-X Systems in: E.A. Starke, Jr., T.H. Sanders, Jr (Eds.). Proceedings of the Second International Aluminum-Lithium Conference sponsored by the Nonferrous Metals Committee of The Metallurgical Society of AIME at Monterey, California, April12-14, 1983.

[3] K.S.Kumar, S.A. Brown and J.R.Pickens, Acta Mater.1996;44:1899.

[4] M. Tiryakioglu and J T.Staley. Physical Metallurgy and the Effect of Alloying Additions in Aluminum Alloys, in: G.E. Totten and D. ScottMckenzie (Eds.). Handbook in Aluminum Vol.1, Physical metallurgy and Processes, New York, Marcel Dekker Inc. 2003.

[5] U.F. Kocks, H.Mecking, Prog. In Mater. Sci. 2003;48:171.

[6] V.Gerold and H.P. Karnthaler, Acta Metall. 1989;37:2177.

[7] T.H. Sanders Jr and E.A. Starke Jr, Acta Metall. 1982;30:927.

[8] S. Suresh, A.K. Vasudevan, M. Tosten and P.R. Howell, Acta Metall. 1987;35:25.

[9] K.T. Venkateswara Rao and R.O. Ritchie, Inter. Mater. Rev. 1992;37:153.

[10] D.Khireddine, R. Rahouadj and M. Clavel, Acta Metall., 1989;37:191.

[11] P.S.De, C.M. Obermark, R.S. Mishra, J. Test & Eval. 2008;36(4):JTE101669.

[12] S. Timoshenko, D.H. Young. Elements of strength of materials, Fifth ed., D. Van Nostrand Co., 1968.

[13] R.S. Mishra, S.R. Sharma, M.A. Mara, M.W. Mahoney: ASM International Joining of Advanced and Specialty Materials III, M. Singh et al eds.,2000:157.

[14] R.E. Crooks and E.A. Starke Jr, Metall. Trans. A 1984;15:1367.

[15] F.J.Humphreys andM.Hatherly. Recrystallization and related annealing phenomenon, First ed., Elsevier, 1995.

[16] D.P. Field, T.W. Nelson, Y. Hovanski and K.V.Jata, Metall. And Mater. Trans. A, 2001;32A:2869.

[17] G.R. Canova, U.F. Kocks and J.J. Jonas, Acta Metall. 1984;32:211.

[18] S.Suresh. Fatigue of materials, Second ed., Cambridge University Press, 1998.

[19] R.W. Hertzberg. Deformation and fracture mechanics of engineering materials, Fourth ed., John Wiley and Sons, 1996.

[20] Y.Ro, S.R. Agnew & R.P. Gangloff, Metall. And Mater. Trans. A, 2007;38A:3042.

[21] J.P. Hirth, J. Lothe. Theory of dislocations, McGraw- Hill Inc, 1968.

[22] P. Neumann, Acta Metall. 1969;17:1219.

[23] R.E. Stoltz, R.M.N. Pelloux, Metall. Trans. 1976;7A:1925.

[24] K. Tanaka, Y. Nakai, M. Yamashita, Inter. J. of Frac. 1981;17:519.

[25] F.J. Humphreys, Acta Mater.199745: 5031.

III. EFFECT OF MICROSTRUCTURE ON FATIGUE LIFE AND FRACTURE MORPHOLOGY IN AN ALUMINUM ALLOY

P. S. De, R. S. Mishra and C. B. Smith

[1]Center for Friction Stir Processing and Department of Materials Science and Engineering, Missouri University of Science and Technology, Rolla, MO 65409, USA

[2]Friction Stir Link, W227 N546 Westmound Dr., Waukesha, WI 53186, USA

ABSTRACT

The effect of grain refinement on fatigue life of 7075Al alloy was evaluated using sub-size fatigue specimen. High cycle fatigue of fine-grained 7075Al showed substantial improvement over the parent 7075-T6 material. This improvement in fatigue life is ascribed to retardation of crack propagation caused by grain boundary acting as barriers and a crack closure effect due to crack deflection.

Keywords: High cycle fatigue; Microstructure; Sub-size fatigue sample; Small crack propagation; 7075-T6

The fatigue life of newly developed or existing materials is of particular interest to the diverse materials science and engineering research community. However, testing using ASTM standard size specimens is often limited by the non-availability of a sufficient volume of material. Furthermore, components that are smaller than standard specimen cross-sections impose further constraints on the use of standard testing methods. This has led to sub-size fatigue sample testing becoming prevalent in failure-critical industries such as nuclear and power generation [1], where it is used to estimate the remaining fatigue life of existing components in use. Apart from such direct commercial and safety applications, such non-standard tests can also be applied as a research tool for developing an understanding of the fatigue properties of new materials. Keeping this broad objective in view, the present authors have used a non standard sub-size bending fatigue sample [2] to study the fatigue life and fracture surface characteristics of a 7075-T6 aluminum alloy.

In this study, the influence of microstructural refinement on the fatigue life of 7075Al alloy was evaluated. A non-traditional approach was adopted to obtain fine-grained 7075Al

fatigue samples. Recently, friction stir processing (FSP) [3] has been used as a method for microstructural modification of cast aluminum alloy [4]. This was further applied to study the fatigue crack growth behavior in A356 alloy [5]. In this study, single pass FSP trials were made on 7075-T6 plates (6.2 mm thick) using a - range of FSP parameters, FSP tool designs, and FSP tool materials. Some of the process zone (nugget) samples comprising recrystallised fine grain structure were subjected to T6 aging heat treatment at 120ºC for 24 hours. The processed zone samples were machined into subsize fatigue samples (henceforth designated as 7075–FSP), the details of which have been reported earlier [2]. A mini-CNC end milling machine was used to machine the fatigue samples. For the sake of comparison, the fatigue properties of parent 7075–T6 were also tested using the same subsize samples with their flat surfaces in as-received condition and milled faces in as–machined condition; all 7075-FSP specimens were finish polished with 3μm lapping film, with their milled surfaces retained in as-machined condition. Thickness uniformity of each sample was maintained accurately to within 0.01 mm.

In order to compare the fatigue life and fracture surface of 7075-T6 and 7075-FSP samples on a common basis the static tensile properties of 7075–T6 sheet and 7075-FSP alloy were first evaluated using a mini-tensile specimen geometry reported previously [6]. The FSP alloy was not solution treated to avoid any abnormal grain growth [7] while the aim of aging after FSP was to retain the fine grain size and obtain as much strengthening from re-precipitation as possible. The static tensile results are summarized in Table 1 and show a reduction in yield strength and ultimate tensile strength (UTS) of 7075-FSP compared to 7075-T6 condition and a substantial improvement in ductility. The tensile data was further used to determine the stress levels at which the fatigue samples were to be tested. Since the objective of this study was to compare the bulk material property, it was essential to eliminate any possibility of anisotropy due to the small sample dimensions used. In a recent study on pure single phase aluminum sheets of different grain sizes, Janssen et al. [8] have shown that specimen size has negligible effect on flow stress for $t/d>3$, where t is the specimen thickness and d the grain size. Considering the average grain size of 35 μm in longitudinal rolling direction for 7075 T-6 sheets (Fig. 1a) and a sample thickness of 1 mm used in this study, the calculated t/d ratio is >>3. On this basis, it was therefore expected that the fatigue life for 7075–T6 measured in this work would be representative of the bulk material property and was further validated by the results obtained (as presented later). The microstructure of 7075-FSP sample (Fig. 1b and c) as observed by optical and transmission electron microscopy shows grain size in the range of 1-3 μm.

Table 1. Summary of tensile test results for the 7075–T6 sheet and 7075-FSP alloy.

Sample	Yield Stress (MPa)	UTS(MPa)	Elongation (%)
7075–T6 Sheet	502±25	545±34	12±1
7075-FSP	461±27	514±21	16±1

The experiments on fatigue life were then conducted at R=-1 ($R=\sigma_{min}/\sigma_{max}$) under a sinusoidal loading pattern. All tests were continued until the samples fractured and severed completely. The maximum bending stress encountered in the sample was calculated using Euler–Bernoulli beam formula:

$$S = \frac{6PL}{bd^2} \tag{1}$$

where, S is the bending stress encountered once the loading cycle has stabilized (at ~50% of measured life), P is the applied point load, L is the distance between axis of point load application and axis of stress calculation, b is the sample width at the section where stress is calculated, and d is the sample thickness.

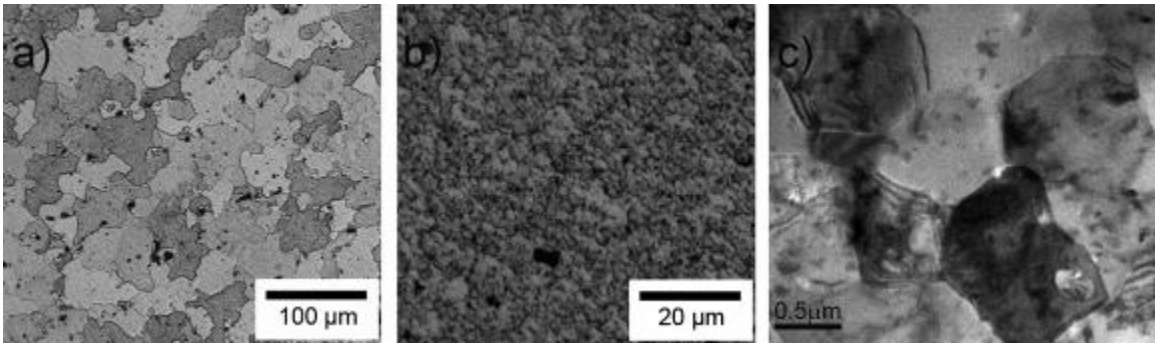

Figure 1. (a) Optical microstructure in the longitudinal direction of as-received 7075–T6 sheet. (b) Optical microstructure of the 7075-FSP sample. (c) Bright-field transmission electron microscopy image of the 7075-FSP sample showing the fine grain size.

Figure 2a shows a comparison of the fully reversed bending fatigue life for 7075–T6 sheet with the handbook data [9]. The first point to note is that the failure life of specimens machined with 4-flute cutting tool matches the handbook data. The previously published 2-flute data [2] indicated a lower fatigue life. Examination of the milled faces of fatigue samples prepared in this study using a 4-flute end milling tool showed that the machined surfaces were much smoother compared to those obtained with a 2-flute end-milling tool in the previous instance [2]. Both the tools were of the same diameter (~0.79 mm), difference being the number of flutes and the length of the shank. Considering the sensitivity of fatigue life to surface finish, this indicates that the choice of milling tool is an important experimental variable that can significantly alter the measured fatigue life of sub-size fatigue specimens. The 7075-FSP specimens were milled using the 4-flute tool and therefore the comparison with 7075-T6 and the handbook data is not influenced by any other factors.

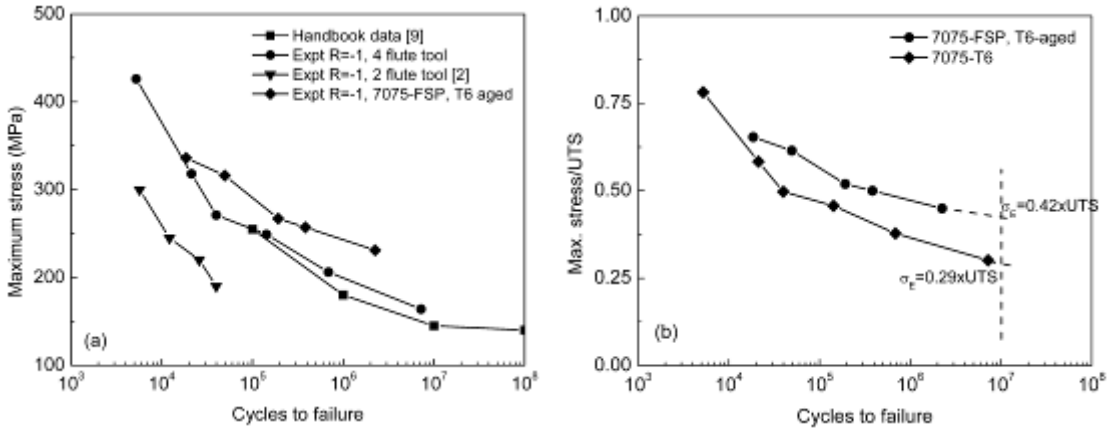

Figure 2. (a) Comparison of fatigue life at R =-1 for 7075Al alloy. For this study, a 4-flute tool was used for 7075-T6 and 7075-FSP alloys. For additional comparison, the data for 7075-T6 from aluminum alloy handbook [8] is included. (b) Normalized S-N curve for 7075-T6 and 7075-FSP. The trend is extrapolated to $1x10^7$ cycles to highlight the increase in the normalized endurance limit for fine-grained 7075-FSP alloy.

The fatigue life of 7075-FSP (Fig. 2a and b) shows an interesting trend. At higher stresses the S-N curve approaches the 7075-T6 S-N curve but as the maximum stress decreases a significant improvement in fatigue life is observed. This is even clearer from Figure 2b where the maximum stress is normalized with the UTS. Further, by extrapolating the trend line in Figure 4.2b to $1x10^7$ cycles the value of the endurance limit (σ_E) obtained was ~0.29 times the UTS value for the coarse-grained 7075-T6. This is in line with conventional aluminum alloys. On the other hand, the value of σ_E is ~0.42 times of the UTS value for the fine-grained 7075-FSP alloy. The above mentioned trend has been further rationalized on the basis of microstructural differences between 7075–T6 and 7075–FSP. At this point, it is worth noting that considering the thickness of samples tested, and the definition of a small crack in ASTM E647 [10], fatigue cracking in 7075-T6 and 7075-FSP samples is in the microstructurally small crack (MSC) and physically small crack (PSC) regime.

The observed improvement in fatigue life with microstructure refinement can be interpreted in terms of interaction of slip band-grain boundary (BSB) model proposed by Tanaka et al. [11] for short cracks. According to the BSB model, the threshold stress for crack growth can be expressed as:

$$\sigma_{th} = \frac{K_c^m}{\sqrt{\pi b}} + \frac{2}{\pi}\sigma_{fr}^* \cos^{-1}\left(\frac{a}{b}\right) \tag{2}$$

where K_c^m is the microscopic stress intensity factor at the tip of the slip band, *b* is the crack length *a* plus the size of the blocked slip band zone w_o, and σ_{fr}^* is the friction stress for dislocation movement in the band. For the small fatigue flaws considered in this work, the threshold stress can be further expressed as:

$$\sigma_{th} = \sigma_{fr}^* + \frac{K_c^m}{\sqrt{\pi w_o}} = \sigma_{fr}^* + \frac{K_c^m}{\sqrt{(\pi/2) d_g}} \tag{3}$$

where w_o is one half of the grain size d_g. In this study, the grain size of 7075-FSP is smaller by an order of magnitude than that of 7075-T6 specimen. The corresponding decrease in friction stress (which equals the yield stress) for 7075-FSP compared to 7075-T6 (~10%) is not significant.

Thus the threshold stress for small crack propagation in 7075-FSP is expected to increase compared to 7075-T6.

In order to justify the perceived role of microstructural refinement on fatigue crack growth, the fractured ends of both 7075-T6 and 7075-FSP samples were investigated with a field emission gun electron microscope (Hitachi S4700). Fatigue fracture for any microcrystalline ductile metal like 7075-T6 (Fig. 3) can be sub-divided into three distinct zones. The crack initiation area (marked by black arrow in Fig. 3a) followed by zone 'A' of stage-I crack propagation, which in turn is followed by zone 'B' of stage –II crack propagation with prominent striation marks, and a final fracture zone 'C' exhibiting failure by void nucleation, coalescence and growth. The typical fracture surface of 7075-FSP (Fig. 4) can similarly be demarcated into three different zones 'a', 'b' and 'c '. Despite this gross similarity in crack growth phases of 7075-FSP and 7075-T6, a closer look at the individual stages reveals subtle differences in the underlying mechanisms at each stage.

Considering the stage-I crack propagation zone first, a high magnification image of region 'A' (Fig. 3b) shows ridges and plateaux with occasional particle pullout and innumerable traces of fine slip. On the other hand region 'a' of 7075-FSP (Fig. 4b) shows a smooth surface with occasional smeared out traces of slip. Two fundamental differences between the stage-I crack propagation zones for 7075-FSP and 7075-T6 can thus be described as follows: (a) the spread of zone-I in 7075-FSP is much smaller (<100 μm) compared to that in 7075-T6 (~500 μm), and (b) the numerous fine slip marks in 'A' typical of micro-crystalline aluminum are absent in zone 'a' of 7075-FSP. The first observation can be explained on the basis of the fact that stage-I crack growth region extends only a few grain diameters for a material [12]. Hence, lower grain size of 7075-FSP is associated with a much smaller extent of stage-I crack growth compared to 7075-T6. The second observation can be attributed to plastic crack closure effect associated with crack deflection (in this instance from grain boundary barriers) in 7075-FSP [12 – 15]. In this context, it may be noted that the effect of plastic crack closure is considered to be most significant during stage-I crack growth [13]. In fact, the evidence suggests that an increase in threshold stress for crack initiation (Eq. (3))) in the BSB model can also encompass the effect of plastic crack closure on microscopic stress intensity.

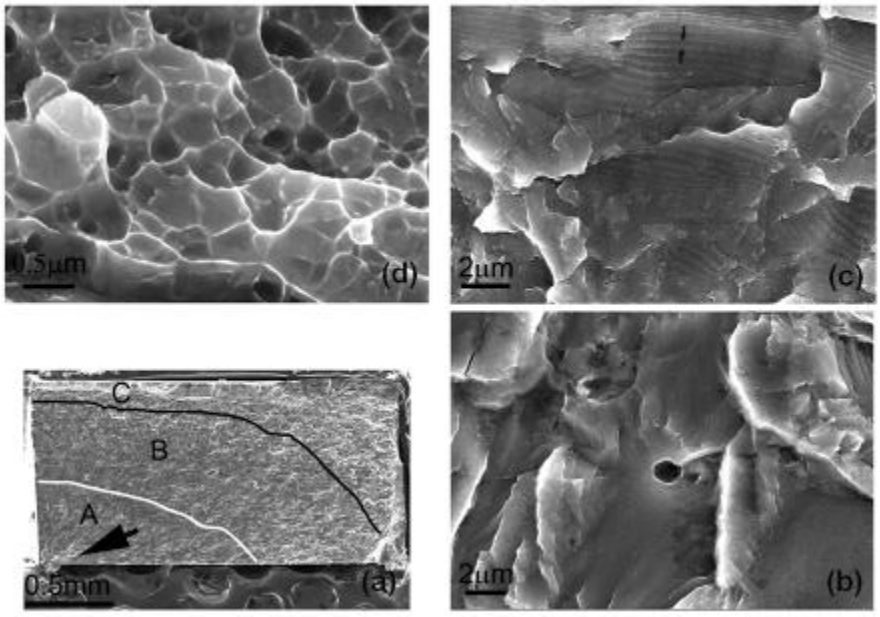

Figure 3. Fracture surfaces of failed 7075 –T6 fatigue sample. This sample failed at 39922 cycles and was tested at R=-1 at a stress amplitude of 428 MPa.

A detailed look at the stage–II crack propagation zone ‘B’ in 7076-T6 (Fig. 3c) shows prominent striation marks. Comparing this to zone ‘b’ (Fig. 4c) reveals important differences in the morphology and distribution of striations in 7075-FSP. The striation marks in 7075-FSP are shallow (white arrows pointing towards each other in Fig. 4c) and less uniform (compared to 7075-T6) and lie alongside areas where irregular slip (black arrow, Fig. 4c, magnified in Fig. 4e) has occurred. Considering the plastic blunting/resharpening model for striation formation by Laird [16], duplex slip is the primary criterion for striation formation in ductile face-centred cubic materials. In coarse-grained 7075-T6 sheet specimen, this would thus involve to and fro dislocation movement within grains. However, with decreasing grain size two aspects begin to differ: (a) dislocation movement becomes more difficult due to the higher stresses required to move them; and (b) the increase in interfacial area/volume leads to smaller planar slip distances. Thus striation formation in finer grains becomes more difficult, resulting in striation marks with a shallow and non-uniform spacing. The existence of neighboring regions with no apparent striation marks (Fig. 4e) leads to more than one possible explanation. Judging by the extent of the ridge and plateaux, these represent grains in the size range of 1-2 µm which is considerably smaller than the average grain size for 7075-FSP. Duplex slip leading to striations in such fine

grains will be more difficult – this would further suggest that a critical grain size exists at which crack movement tends to be planar-type depending on grain size, composition and precipitate distribution. Alternatively, the crack closure effect can also be responsible for this phenomenon. A comparison of Figure 3c with Figure 4c shows that crack deflection is much higher in the case of 7075-FSP compared to 7075-T6. Such crack deflection can lead to a plastic closure effect resulting in smearing of the striation lines and associated decrease in crack growth rate. The final fracture zone 'C' (Fig. 3d) and 'c' (Fig. 4f) shows equiaxed distribution of voids, indicating a predominantly Mode-I type failure.

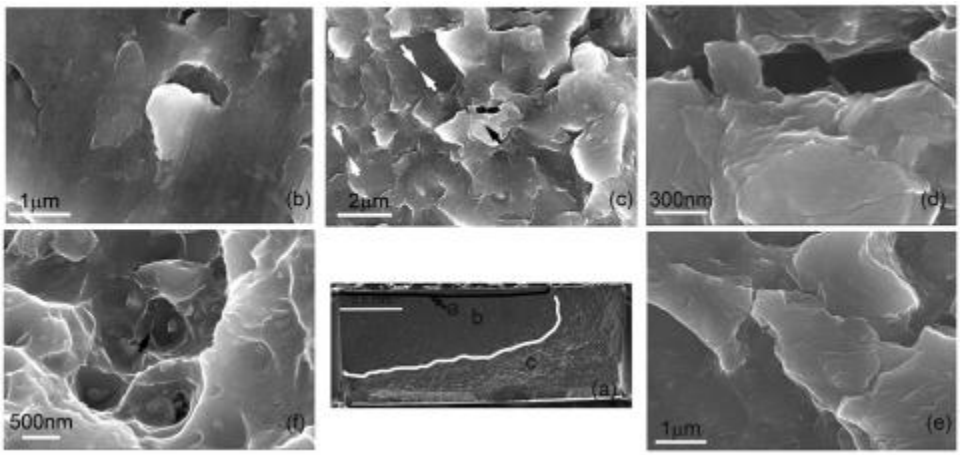

Figure 4. Fracture surface of failed 7075–FSP fatigue sample. This sample failed at 49629 cycles and was tested at R = -1 at a stress amplitude of 311 MPa.

Interestingly, a similar improvement in fatigue life of friction stirred nugget region over parent material has been observed in AZ-91 magnesium alloy produced by high pressure die casting [17]. Cavaliere et al [17] friction stir processed AZ-91 base alloy to obtain a fine recrystallized structure with a grain size of ~4 μm. The friction stirred material was then used to study the fatigue property and crack growth rate using a flat specimen 12 mm long, 2 mm wide and 2 mm thick. Compared to the base material, friction stirred material shows a lower fatigue crack growth rate and higher threshold stress. In their experiments, the nugget region showed a

higher yield strength and elongation over the parent material both in as-friction stirred and in friction stirred and heat treated conditions, unlike in the current 7075-FSP, where the yield strength and UTS decreased while total elongation increased in comparison to the parent alloy. From this it appears that the fine grain size resulting from the friction stir process is primarily responsible for the improvement in fatigue life. However, as a note of caution it maybe added that the fundamental difference between friction-stirred 7075-T6 and AZ-91 alloy in terms of crystal structure will lead to differences in deformation micromechanisms which can affect the fatigue life.

From this study, the following concluding remarks can be made:

1. Grain refinement combined with a relatively dislocation-free microstructure improves the fatigue life of friction stir processed 7075Al in the high cycle fatigue regime.
2. On the basis of fracture surface morphology evaluation, this improvement can be ascribed to reduced crack propagation rates in both the MSC and PSC regimes.
3. In the MSC regime, this is due to the barrier effect of grain boundaries, while in PSC regime this is probably due to either an increased crack closure effect caused by crack deflection or increased difficulty in slip due to the smaller grain sizes.

Acknowledgment: This paper is based upon work supported by the AFOSR under Contract No. FA9550-080C-0027 and the experimental help of Jeff Rodelas is greatly appreciated. Any opinions, findings and conclusions or recommendations expressed in this paper are those of the authors and do not necessarily reflect the views of the AFOSR.

[1] T.H. Hyde, W.Sun and J.A. Williams, International Materials Review, 52 (2007) 213.
[2] P.S.De, C.M. Obermark, R.S,Mishra, J. Testing and Evaluation, 36, (2008) 402.
[3] R.S. Mishra and Z.Y. Ma, Materials Science and Engineering: R, 50 (2005) 1.
[4] Z.Y.Ma, S.R. Sharma, R.S.Mishra, M.W. Mahoney, Mater. Sci. Forum 289 (2003) 426.
[5] S.R.Sharma, R.S.Mishra, Scripta Materialia 59 (2008) 395.
[6] R.S.Mishra, S.R.Sharma, M.A.Mara, M.W.Mahoney, ASM International Joining of Advanced and Specialty Materials III (2001) 15.
[7] I. Charit, R.S. Mishra, Scripta Materialia, 58 (2008) 367.
[8] P.J.M Janssen, Th.H.de Keijser, M.G.D. Geers, Mater. Sci. Eng A 419 (2006) 238.

[9] J. G. Kaufman, Properties of Aluminum Alloys, ASM International, Materials Park, OH, 1999, p.297.

[10] Standard test methods for measurement of fatigue crack growth rates, ASTM E647-08, V 03.01, ASTM, 2008.

[11] K.Tanaka, Y.Nakai, M. Yamashita, Int. J. of Fracture, 17(1981) 519.

[12] K.J. Miller, Mat. Sci. Tech. 9 (1993) 453.

[13] S. Suresh, Fatigue of Materials, 2nd edn, Cambridge University Press, 1998.

[14] X.P. Zhang, C.H. Wang, L.Ye and Y.W. Mai, Fatigue Fract. Eng. Mater. Struct. 25 (2002) 141.

[15] P.Lukas, L. Kunz, International J. Fatigue, 25 (2003) 855.

[16] C. Laird, Fatigue Crack Propgation, STP 415, American Society for Testing and Materials, p131.

[17] P. Cavaliere, P.P. De Marco, Mat. Characterization, 58(2008) 226.

IV. MICROSTRUCTURAL EVOLUTION DURING FATIGUE OF ULTRAFINE GRAINED ALUMINUM ALLOY

P.S. De and R.S. Mishra
Center for Friction Stir Processing, Department of Materials Science and Engineering
Missouri University of Science and Technology, Rolla, MO 65409

ABSTRACT

A comparative study of the surface microstructural changes during fatigue of a precipitation hardened (PH) aluminum alloy in ultrafine grained (UFG) and microcrystalline conditions was done using orientation imaging microscopy (OIM). With increase in applied stress amplitude, the fatigue life of fine grained PH alloy deteriorated. On the other hand, at lower stress amplitudes an improvement in fatigue life was noted. This trend was reversed for the coarse grained PH alloy. In UFG alloy, the fatigue life improved at all stress amplitudes. The variation in fatigue life response between coarse, fine and ultrafine grain PH alloy was due to the increased interaction between low angle and high angle boundaries with grain size decrease. Both, conservative and non-conservative dislocation movement during fatigue controls this process. In UFG alloy, additional interaction with the dispersed second phase causes an overall improvement in fatigue life. A direct evidence of room temperature recrystallisation during fatigue in UFG alloy was also observed.

Keywords: Aluminum alloys; Ultrafine grain; fatigue; Recrystallization; EBSD

1. INTRODUCTION

The role of microstructure in high cycle fatigue life of metals has been the subject of continuing research for the past few decades. Conventionally, most of these research efforts were confined to single crystal and microcrystalline (MC) metals and alloys (grain size>10μm). However, the ongoing research on nanocrystalline (NC) and ultrafine grained (UFG) metals and consequent length scale changes demand a fresh understanding of the microstructural effects on fatigue micromechanisms.

The most comprehensive studies on the fatigue micromechanisms have been with respect to single crystal metals grown in particular slip orientations (single/multiple slip) [1-4]. However, the absence of grain boundary effects and the microstructural length scale differences (3 -4 orders

of magnitude with UFG materials) thereof, prevents their extension into the UFG regime. The grain boundary effects on fatigue life, on the other hand, are no less complicated. A noteworthy example of this is observed in the variability of crack growth rate in the small/long crack domain [5]. Thus, although grain size reduction leads to an increased crack propagation resistance for small cracks, the reverse is true for long cracks. In fact, these apparently conflicting effects of crack length on fatigue crack propagation continues to be an area of active research [6-7].

Theoretically, a grain boundary constitutes a surface separating two regions of the same crystal structure in definite spatial orientation relationships (e.g., in terms of the Euler angles (φ_1, Φ, φ_2)) with respect to a pre-defined reference frame. A comprehensive grain boundary characterization therefore includes the misorientation between the two regions along with the nature of their grain boundary plane. An alternative and a more familiar description of grain boundary is given in terms of the angle (θ)/axis misorientation [8]. This misorientation-based classification leads to the coincidence site lattice (CSL) framework of grain boundaries in specific angle/axis combinations. A more generic approach is, however, based on the misorientation (θ) with $\theta<15^\circ$ defined as low angle grain boundary (LAGB) and $\theta>15^\circ$ termed as high angle boundary (HAGB) [9].

Thus, a rational approach in understanding the microstructural effects on the fatigue life of UFG metallic materials will require a consideration of the individual grain boundary components. The underlying hypothesis being: the smaller grain size of UFG metallic materials changes the dynamics of LAGB formation and dislocation/HAGB interactions during fatigue. Consequently, this work highlights the difference in the surface microstructural changes during high cycle fatigue of an UFG and a MC material using orientation imaging microscopy (OIM). The difference was further interlinked with the variation in fatigue life with a change in the microstructural length scale. In the next section a brief introduction of the current state of knowledge in fatigue damage accumulation with respect to MC and UFG metals is presented.

2. FATIGUE DAMAGE: A BACKGROUND

The fundamental concepts for crack initiation and fatigue damage in MC metals were developed from the studies conducted on single crystal copper [1-4]. This approach consisted of cyclically deforming a crystal, in definite slip orientation, under plastic strain-controlled condition. The above methodology leads to the concept of fatigue as a measure of the damage accumulation capacity of a metal by irreversible dislocation movement [5]:

$$\gamma_{pl}^{R} = 4N \sum_{i=1}^{n} \gamma_{pl,i}^{R} \quad (1)$$

where γ_{pl}^{R} is the cumulative plastic strain, and $\gamma_{pl,i}^{R}$ is the plastic shear strain resolved in the active slip system for i'th cycle. The above definition, however, ignores the damage caused by reversible dislocation movements. The general trend emerging from such studies, along with the accompanying microstructural evolution, is summarized in Fig. 1. Thus, for a low stacking fault energy (SFE) face centered cubic (f.c.c) metal like Cu, at the low plastic strain amplitude levels (ε_{pl} <10^{-4}) of Region A (Fig. 1b), vein and labyrinths composed of edge dislocation dipoles are observed [1,4]. A further increase in the plastic strain amplitude (ε_{pl} >10^{-4} but <10^{-2}, Region B) is characterized by a constant saturation stress with persistent slip band (PSB) formation [1,4]. At the plastic strain amplitude levels of region C (ε_{pl} >10^{-2}) dislocation cell structures [1,4] are observed.

The cyclic loading response of a high SFE metal-like aluminum however differs from that of copper in certain aspects. Thus, in pure single crystal aluminum (99.998%), a hardening–softening trend followed by a secondary hardening has been observed [10]. The fatigued microstructure consisting of densely packed dislocation walls separated from each other by ~2μm with occasional cell and subgrain formation [10]. Identical experiments on polycrystalline single phase aluminum (99%) results in a dislocation cell structure development, with cell size in the range of 1.4–1.8 μm; the cell dimensions varying inversely with the plastic strain amplitude [11]. A similar study by Feltner [12] on 5N polycrystalline Al, yielded a cell size ranging from ~1.5μm (at 78K) to >5μm (at 300K). Thus, no definite dependency between purity of Al and cell size was observed. In fact, CSS experiments conducted on Al-4.9 wt%Zn-1.2wt% Mg [13] notched single crystals in peak-aged condition show a dislocation band spacing of ~1μm; the PSBs formed, having a width of ~200 nm and lacked the ladder like structure typical of a copper crystal. In another study on polycrystalline Al-5 wt% Zn-2.5 wt% Mg, PSBs with a width of ~1μm was observed [14]. Thus, an overall similarity in the fatigue damage accumulation process of MC aluminum and single crystal is evident.

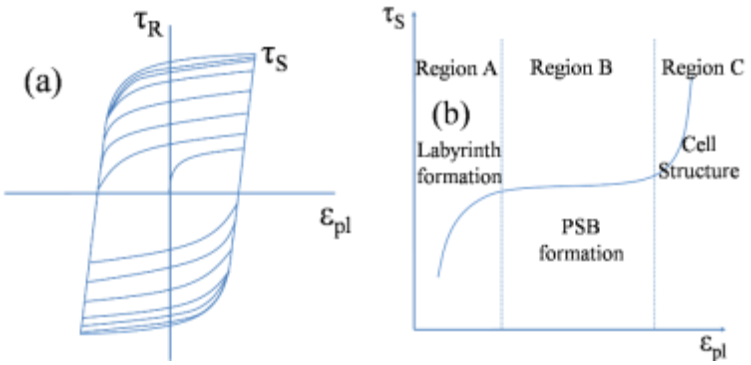

Fig. 1. (a) A generic cyclic stress strain (CSS) curve in plastic strain-controlled test showing hardening, followed by stress saturation and (b) microstructural features at saturation stress in CSS for different levels of plastic strain amplitude imposed [1].

In context with UFG alloys the situation however changes in the following two respects:

(a) the sub-micron grain sizes of UFG metals are similar or smaller in length scale than the cell size observed in single crystal or microcrystalline aluminum alloys; and

(b) UFG grain sizes have dimensions which are comparable to the typical PSB width and wall thickness combined together.

Consequently, significant difference in the fatigue damage evolution of a UFG metal as compared to a corresponding MC metal is expected. An example of this is observed in the microstructural changes of a UFG single phase Cu during fatigue. The principal features of which can be summarized as:

(a) persistent shear band formation on surface [18];

(b) occurrence of coarsened cell structure with typical MC fatigue features of vein and PSB within the cell structures [15-17]; and

(c) recrystallization during fatigue [16-17].

Similar experiments conducted on single phase UFG aluminum (ECAP route) by Hoppel et al. [19] indicated a tendency towards grain coarsening with shear band development. Quite contrarily, the microstructural investigation by Wong et al. [20] on ECAP-processed UFG aluminum (99.5%), revealed no grain coarsening/damage due to fatigue. In fact, in only five out of the three hundred transmission electron microscope (TEM) specimens investigated by the authors, shear bands extending through the grain boundaries were observed. Similar work on UFG AA5083 alloy (processed by cryomilling) was accompanied with the development of slip

band type of structures within the coarsened microstructure [21]. These results lead to some interesting questions:

- How is fatigue damage accommodated in UFG metals?
- With a grain size in the range of the fatigue damage structures of MC/single crystals, what will be the role of grain boundaries vis-à-vis matrix?

The current study clarifies the above questions by using a comparative characterization approach on an aluminum alloy of two different grain sizes (MC and UFG). The importance of grain boundaries on fatigue damage accumulation and their role in determining the fatigue life has also been dealt with.

3. MATERIAL AND EXPERIMENT DETAILS

The base material used in this work was a AA7075-T6 alloy with a nominal composition (in weight percent) Cu 1.2-2.0, Mg 2.1-2.9, Cr 0.18-0.28, Zn 5.1-6.1, balance Al. Commercially available AA7075 T6 sheets of ~3.2 mm thickness were machined in to 50×150 mm rectangular blocks, which were resolutionized (753 K for 55 min), water quenched and then friction stir processed (FSP) [22] to obtain a UFG AA7075 microstructure. A friction stir welding (FSW) tool of shoulder diameter 11 mm, pin base diameter 5.6 mm and a pin height 2.7 mm was used for this purpose. This FSP material was further categorized into three different regions, (a) initial plunge affected zone (20 mm of post plunge region), (b) the steady state processed zone, and (c) tool retraction zone (20mm of pre-retraction zone). The steady state processed UFG AA7075 material, stabilized at 373K for 24 h, was used in subsequent experiments. It may be clarified here that, only a portion of the nugget comprising of a uniformly recrystallised microstructure was utilized. This was done to ascertain a similar grain size distribution within the entire specimen volume. In addition to the UFG AA7075 microstructure, a coarse grained variant of the AA7075-T6 was also generated. A portion of the UFG AA7075 material, coarsened by grain growth [23], was water quenched and aged (393K for 24 hours) to obtain a coarse grained 7075 in T6 (CG AA7075-T6) heat treated condition. Apart from these two principal microstructures, a 1 mm thick, rolled sheet of AA7075 in T6 heat treated condition (AA 7075-T6) and a fine grained 7075 (FG AA7075) obtained from a previous work [24] was taken into consideration.

Subsequently, a detailed microstructural characterization of UFG AA7075 and CG AA7075-T6, using optical microscopy (OM), scanning transmission electron microscopy (STEM) and OIM was performed. All mechanical characterization (tensile and fatigue tests) in this study were conducted at room temperature on custom designed sub-size bending fatigue and

tensile test beds [25,26]. Fig. 2 schematically illustrates the location of the corresponding subsize specimens with respect to the friction stir processed material volume.

One of the principal objectives of this study was to evaluate the surface microstructural changes occurring during fatigue. To accomplish this, OIM of the subsize fatigue samples were performed. The OIM investigations were carried out at a fixed sample location, both before and after fatigue. For CG AA7075-T6 this was achieved by using the microscope stage axis origin as the principal reference point. In case of UFG AA7075, since the mapped area was much smaller, the approach used for CG AA7075-T6 proved difficult to implement. The problem was overcome by using a fiduciary marker (dimension: 0.5 micron deep, 5 micron long) focused ion beam milled into the sample. All OIM investigations in this work were conducted using a field-emission gun scanning electron microscope (FEGSEM) operated at 10 KV acceleration voltage with an emission current of 5.5 nA. A Nordylys imaging system interfaced with HKL technology software was used for data acquisition and analysis. It should be noted here that only the aluminum phase was identified using OIM. The second phase particles in UFG AA7075, showed up as unresolved regions. In order to locate the grain boundary positions of different misorientations, these OIM images were further processed using the image analysis tools in MATLAB®.

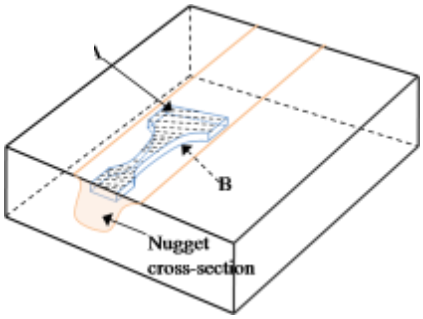

Fig. 2. Position of the subsize sample (fatigue sample schematic displayed here) in the steady state zone of the friction stir processed material. Sampling was done in such a way so that the grain size within the specimen volume remained uniform.

4. RESULTS

4.1 Microstructural details

The principal microstructural variables applicable for this study were: (a) grain size, and (b) dispersed phase size and distribution. In Fig. 3, typical image of the three different microstructures are shown. Thus, in CG AA7075-T6, a bimodal grain distribution (mean sizes of 40 and 100μm), with occasional large grains of size ~200μm, was observed. The UFG AA7075 exhibited an equiaxed grain morphology, quite unlike the pancake shaped grain structure in AA7075-T6 alloy. In addition, the UFG AA7075 microstructure showed a log-normal grain size distribution with a maximum grain size of approximately 2.5 μm. The fraction of grains greater than 1μm in UFG AA7075 was less than 5% of the total distribution. In Table 1, the mean grain size and respective standard deviation (except for CG AA 7075-T6) for the different microstructures used in this work are summarized. Since the tensile stresses applied during fatigue were in the direction of rolling, the stated grain size for AA7075-T6 is that for the longitudinal–thickness direction.

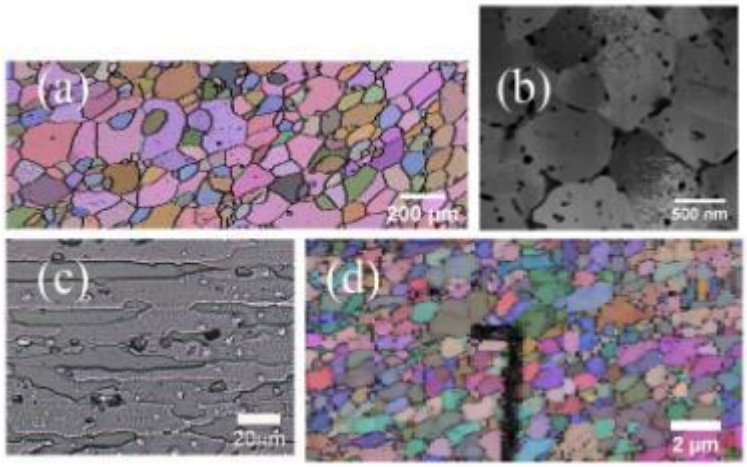

Fig. 3. (a) OIM image of CG AA7075 in T6 condition with 3 μm step size. (b) Bright field STEM image of UFG AA7075. (c) Optical image of AA7075-T6 sheet. (d) OIM image of UFG AA7075 with focused ion beam milled marker for locating the same location after fatigue with 0.05μm step size. The STEM image has been gamma corrected (γ=1.3).

An analysis of the second phase in CG AA7075-T6 reveals that GP zone constitutes the principal hardening phase [28]. The UFG AA7075 microstructure on the other hand, was characterized by extensive grain boundary precipitates with size in the range of 50-300 nm. Occasionally, circular phases of dimensions ≤50 nm within grains were also observed. To identify the composition of this dispersed phase, a simultaneous OIM-EDS mapping was performed. Mg and Zn were found to be the principal constituent elements. Considering the composition of the alloy used, the dispersed second phase in the UFG AA7075 was therefore predicted to be a variant of the $MgZn_2$ (η) phase typical of AA7075 alloy [29]. The total volume fraction (measured by area analysis using ImageJ [30]) of the dispersed phase in UFG AA7075 was calculated to be ~9±3 %.

Table 1 Mean grain size (G.S) of the different microstructures, measured using linear intercept method [27] and their corresponding standard deviations.

Condition	UFG AA7075	FG AA 7075	AA7075-T6 sheet
G.S (μm)	0.5±0.1	1.2 ± 0.4	10 ± 5

4.2 Tensile properties

In Table 2 the monotonic tensile test results of the four different microstructures are summarized. All tensile tests in this study were conducted at a constant crosshead velocity with an initial strain rate of 10^{-3} s^{-1}. The yield stress values reported here for FG AA7075, CG AA7075-T6 and AA7075-T6 are the 0.2% offset strengths. In UFG AA7075, the tensile curve displayed a distinct yield point phenomenon with dynamic strain aging. The yield stress value reported for UFG AA7075 therefore corresponds to its lower yield point. Also, the dynamic strain aging characteristics similar to that of UFG AA7075 have been previously reported for UFG aluminum processed using hot deformation techniques [30-32].

Table 2 Averaged tensile test results (samples 5 or more) of the four different microstructures with their respective yield stress, ultimate tensile stress and uniform elongation.

State	UFG AA7075	FG AA7075 [24]	CG AA7075-T6	AA7075-T6 sheet
σ_{YS}(MPa)	343 ± 7	461 ± 27	474 ± 5	502 ± 11
σ_{UTS}(MPa)	409 ± 11	514 ± 21	541 ± 12	564 ± 4
$\varepsilon_{uniform}$(%)	12.6 ± 1	16 ± 1	8 ± 0.5	7 ± 3

4.3 Fatigue properties

In Fig. 4a the S-N fatigue curves for the four different microstructures with respect to their absolute stress amplitudes are presented. For UFG AA7075 and CG AA7075-T6, the fatigue life below ~250 MPa were almost identical; both being lower than that of AA7075-T6 sheet. The maximum fatigue life at low stresses was however exhibited by FG AA7075. Their values exceeding that of AA7075-T6 sheet specimens by almost an order of magnitude.

Since the UTS values of the four microstructures were different, a convenient way of comparing the fatigue life would be to normalize the S-N curves. In Fig. 4b the normalized S-N curves for the four microstructural variants are compared. The normalization process performed, with respect to the corresponding ultimate tensile stresses. In the normalized scale, both FG AA7075 and UFG AA7075 reveals an order of magnitude improvement in fatigue life over CG AA7075-T6 and AA7075-T6 at the low stress amplitudes ($<0.4\ \sigma_{UTS}$). This positive trend was continued for UFG AA7075 even up to $\sim 0.8\ \sigma_{UTS}$. The fatigue life of FG AA7075 on the other hand demonstrated a decreasing trend, ultimately merging with that of CG AA7075-T6 and AA7075-T6 sheet at $\sim 0.6\ \sigma_{UTS}$.

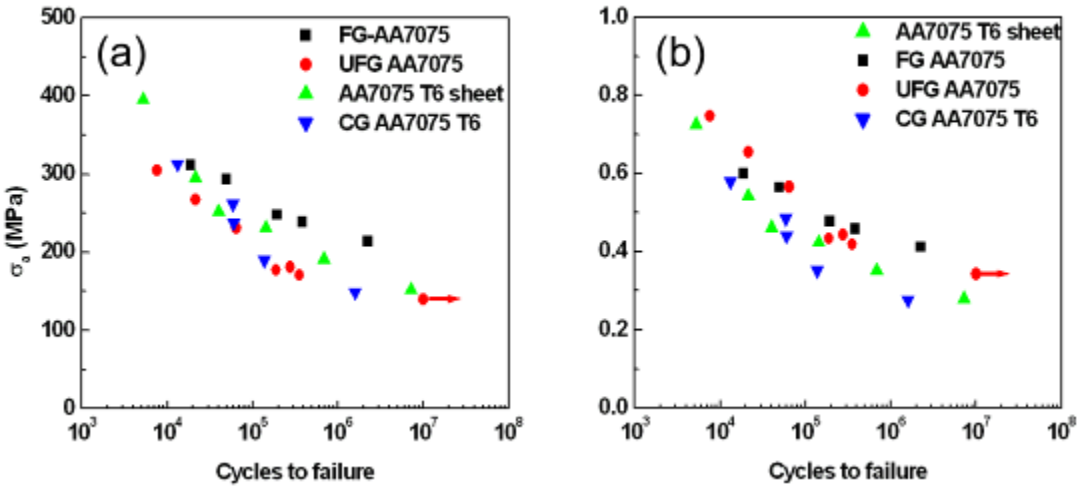

Fig. 4. (a) S- N curves for CG 7075-T6, FG-7075 and UFG-7075 in bending fatigue conditions at R=-1. (b) S-N curves for CG-7075-T6, FG-7075 and UFG-7075 with normalized stress.

4.4 Microhardness change at different stress amplitudes

The hardness of any metal is related to its yield stress [33]. Hence, hardness measurement, before/after testing, gives an indication of the work hardening occurring during fatigue. In Fig. 5, the change in surface micro-hardness for CG AA7075-T6 and UFG AA7075 specimens tested at different stress amplitudes are presented. The hardness values were an average of the measurements conducted over 10-20 random points selected over the entire specimen gage length. During this experiment a region of ~0.5 mm from the fracture surface was avoided to eliminate crack tip plasticity effects. The base hardness values were measured from the specimen grip (unstressed area) regions. For UFG AA7075, the hardness value after fatigue increases with an increase in the applied stress amplitude. The CG AA7075-T6, on the other hand, exhibits an opposing trend. The maximum hardness increase being observed at the lower stress amplitude with little/no change at the higher stress levels.

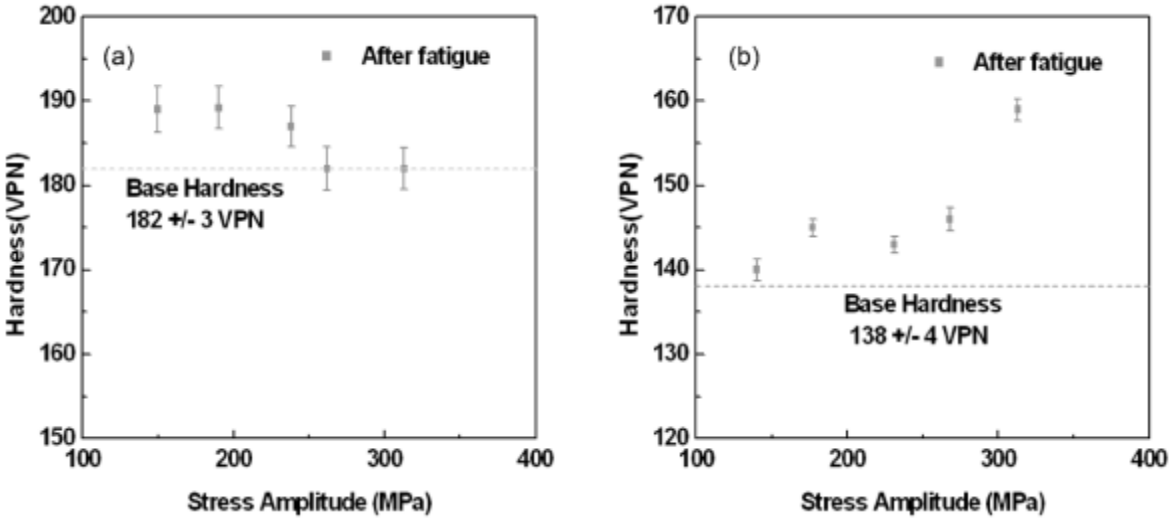

Fig. 5. Change in hardness of (a) CG AA7075-T6 and (b) UFG AA7075 after fatigue at different stress amplitudes.

4.5 LAGB misorientation change during fatigue

The strain accommodated in a metal during fatigue and the resultant dislocation activity leads to the introduction of lattice dislocations with consequent LAGB formation. These LAGBs accounts for a very significant part of the energy stored in a metal during straining. In fact, much of the grain and subgrain boundaries in a deformed metal fall into this LAGB category. A measurement of the change in LAGB distribution is therefore an indicator of the strain energy (fatigue damage) accommodated during fatigue. In Fig. 6, the change in LAGB fraction for UFG AA7075 and CG AA7075-T6 during fatigue, as measured using OIM is presented. The highlights of these observations are:

(a) A frequency increase for misorientation less than 2.5˚ (henceforth low misorientation LAGB (LMLAGB)), for both CG AA7075-T6 and UFG AA7075, was observed;

(b) The increase in LMLAGB for UFG AA7075 (23.3%) was significantly higher compared to CG AA7075-T6 (7.6%)and

(c) a frequency decrease for misorientation between 2.5 and 14.5˚ (henceforth high misorientation LAGB (HMLAGB)) for UFG AA7075 was observed; whereas in CG AA7075-T6 no specific trend was noted.

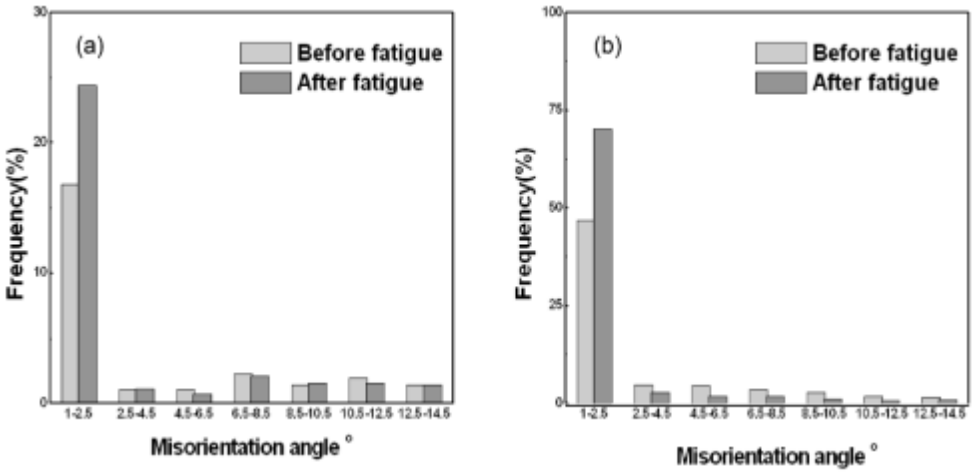

Fig. 6. Change in area misorientation before and after fatigue in the same area of fatigue sample for: (a) CG AA7075 T6 (σ_a =240 MPa). (b) UFG AA7075 (σ_a =180 MPa). The minimum misorientation considered in all cases was 1˚.

To understand the underlying process further, the microstructural distribution of different LAGB fractions in UFG AA7075 (both in a fatigued and non-fatigued sample) were investigated. In Fig. 7a–d the typical distribution of LMLAGB/HMLAGB boundaries in UFG AA7075 were plotted on an inverse pole figure map of the OIM image. For UFG AA7075, the HMLAGBs were located principally along the boundary of different grain orientations (as delineated by the change in grain colors). The distribution of LMLAGB in UFG AA7075 was however different; some lying within the matrix, the majority projecting from the unresolved regions into the matrix.

In Fig. 8a–d the distribution of LMLAGB and HMLAGB in CG AA7075-T6 (both before and after fatigue) are shown. Unlike in the case of UFG AA7075, the LMLAGB in CG AA7075-T6 (both before and after fatigue) resides mainly within the matrix (see Fig. 8a and c). The HMLAGB's on the other hand were located along the boundaries of different grain orientations as shown by the change in grain colors (Fig. 8b and d).

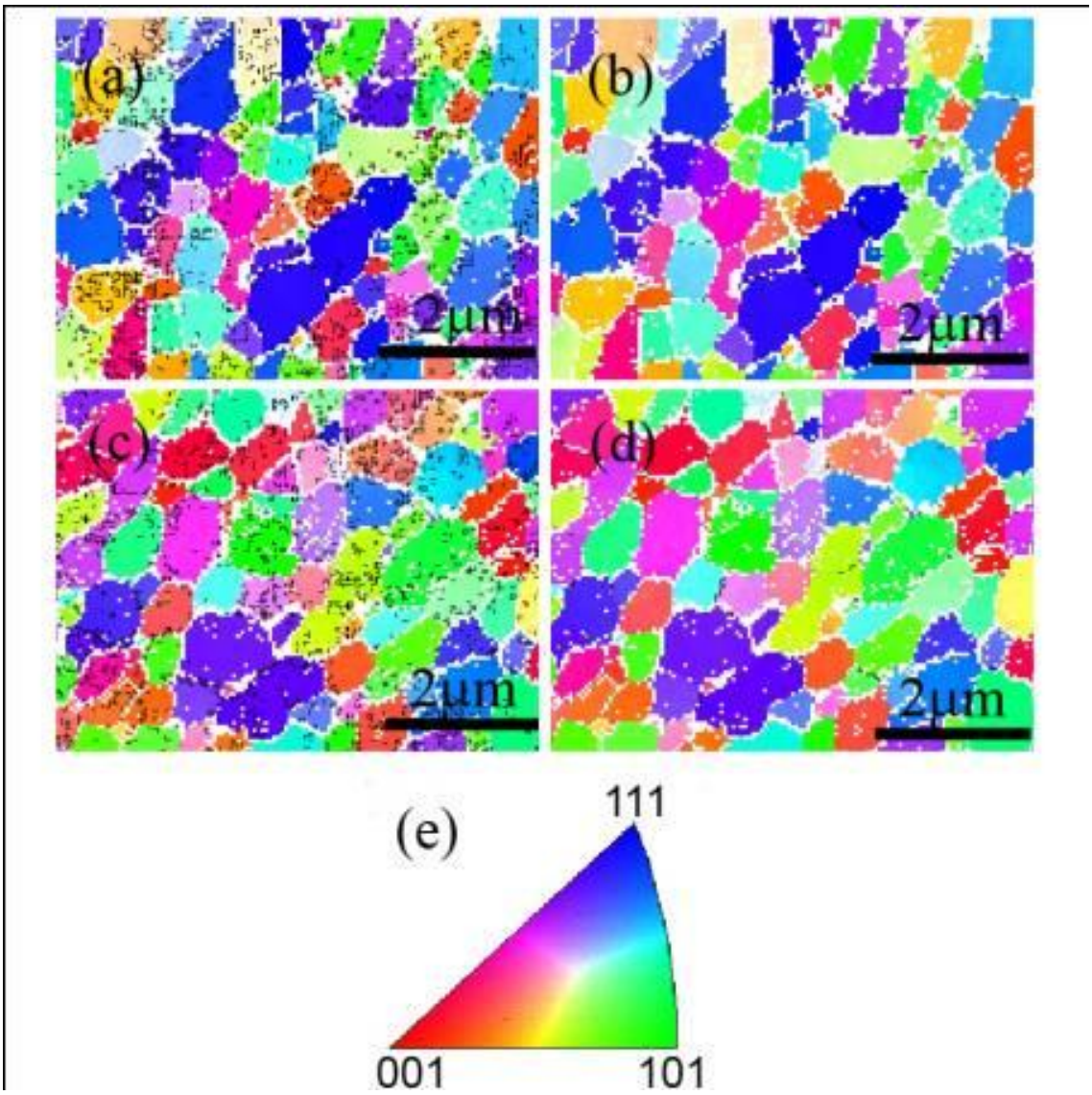

Fig. 7. (a) The distribution of LMLAGB in UFG AA7075 after fatigue (σ_a = 313 MPa). (b) The distribution of the HMLAGB in UFG AA7075 after fatigue (c) The LMLAGB distribution in UFG AA7075 before fatigue. (d) The distribution of HMLAGB in UFG AA7075 before fatigue. The black lines/dots indicate the LAGB positions in each case. The locations of LMLAGB/HMLAGB were superimposed with the help of MATLAB based image analysis. (e) Legend of pole figure coloring.

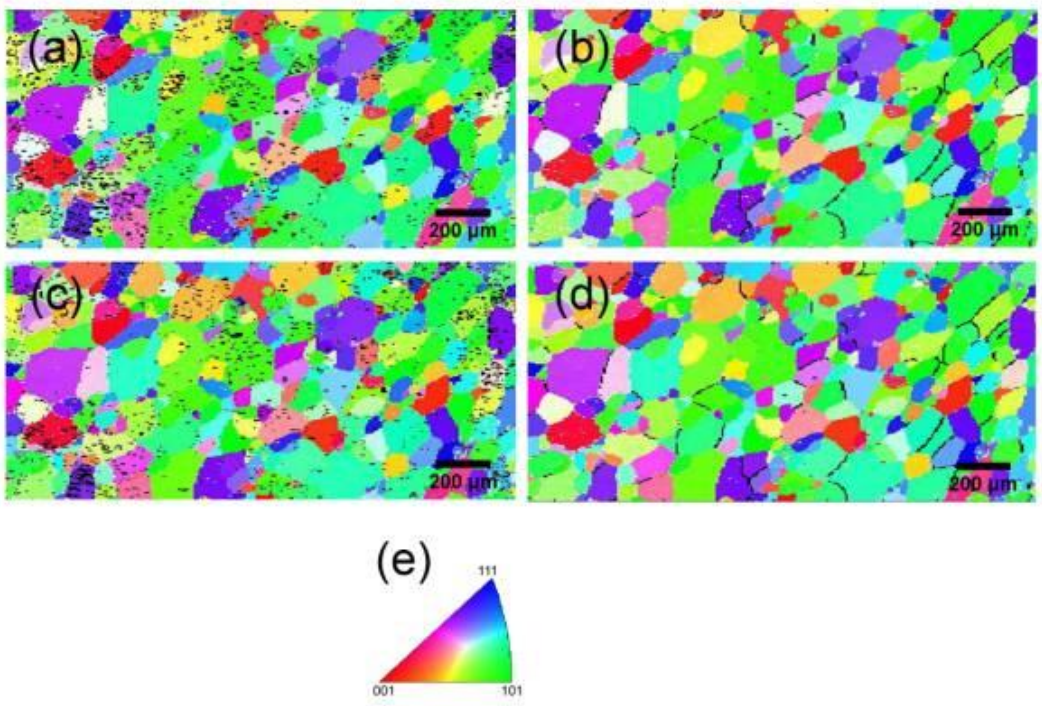

Fig. 8. (a) The LMLAGB distribution in CG AA7075-T6 after fatigue. (b) The distribution of the HMLAGB in CG AA7075-T6 after fatigue in the same sample as Fig. 5.6a. (c) The LMLAGB distribution in CG AA7075 T6 before fatigue. (d) The distribution of HMLAGB in CG AA7075 T6 in the same sample as Fig. 6a. The black lines/dots indicate the LAGB location in each case. The locations of LMLAGB/HMLAGB were superimposed with the help of MATLAB based image analysis. (e) Legend of inverse pole figure coloring.

4.6 Recrystallization during fatigue

As already mentioned, till date no definite evidence of recrystallization in UFG aluminum during room temperature fatigue has been reported. To investigate this issue further, an OIM based characterization of the fatigue samples was conducted. In the case of UFG AA7075, this resulted in a direct evidence of recrystallization during room temperature fatigue. As an example, consider the grain ‘A’ marked in Fig. 9a. After room temperature fatigue, this particular grain sub-divided into a multiple numbers of smaller grains (Fig. 9b). The process is illustrated more clearly, by plotting the misorientation change in grain ‘A’ (Fig. 5.9a) across line CD (Fig. 9b) with respect to the orientation of initial point C (Fig. 10a).

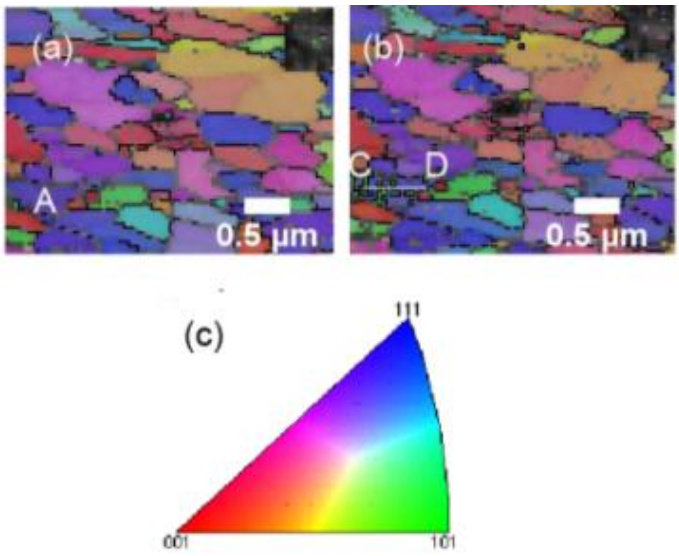

Fig. 9. (a) OIM of sample before fatigue with grain ‘A’ with a combination of inverse pole figure (IPF) and band contrast (BC) coloring. (b) OIM of sample after fatigue with grain A in recrystallized state with IPF and BC coloring. In both (a) and (b) the black lines indicate HAGB (>15˚) which are interspersed with areas of high band contrast (grey) due to dispersed phases. The dark areas were unresolved due to low band contrast. (c) Legend for the inverse pole figure coloring used.

The plots clearly indicates that the initial single grain ‘A’ had subdivided in to multiple grains, each separated from the other by HAGB. The corresponding area misorientation change of grain ‘A’ has been presented in Fig. 10b. It may be added here that the observed recrystallization tendency did not lead to any grain coarsening.

The salient features observed during this recrystallization process can be summarized as:

(a) The recrystallization phenomenon occurred within one single grain whose original HAGB has remained unchanged. No other surrounding grains / dispersed phases were affected during this phenomenon (Fig. 9a and 9b).

(b) The Kikuchi pattern for all points except one central point within the original grain were resolved to be as that of aluminum.

(c) The original grain sub-divided itself into a number of smaller grains, all of which were of similar orientation (Fig. 9b). The remaining portions of grain ‘A’ had however retained their original orientation.

(d) A net decrease in the LMLAGB fraction after recrystallization has occurred (Fig. 10b).

(e) The HAGB of the recrystallized grains were mainly comprised of Σ29a boundary.

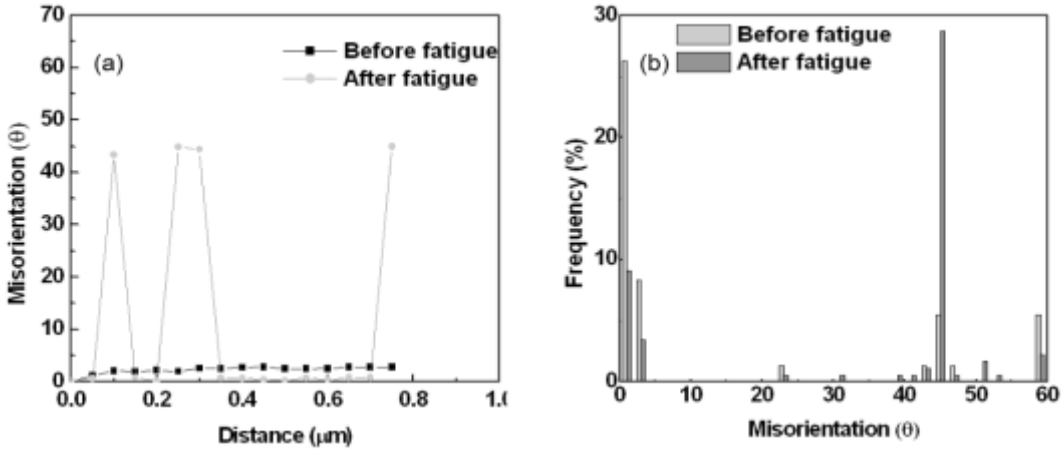

Fig. 10. (a) Misorientation plot across line CD (Fig. 9b) before and after fatigue. (b) Misorientation angle distribution in Grain 'A' region of Fig. 9a before and after fatigue.

4.7 Stages in crack propagation- fractography

The UFG AA7075 shows the typical three stage crack propagation observed in microcrystalline aluminum alloys. However, the fracture surface topography was distinctly different compared to that observed in the microcrystalline. In Fig. 11 the typical fracture surface during the three stages of crack propagation in UFG AA7075 is shown. The stage –I fracture surface typical at low stress amplitudes is shown in Fig. 11a. The stage-I fracture surface showed tortuous crack propagation and was wavy in nature with slip plane tearing. At higher magnifications (see inset in Fig. 11a) small cracks were noted. However, no interlinking of cracks typical of intergranular crack propagation was observed. At high stress amplitudes the stage-I fracture surface exhibited tire track marks typical of two phase alloys. In Fig. 11c the striation marks typical of stage-II crack propagation can be seen. The striation marks were ill-formed and interspersed with crack plane tearing (see inset) and were observed only in the high stress

amplitude samples. The final stage-III crack propagation showed the typical void coalescence type failure where void size was similar to the average grain size with precipitates located within the voids.

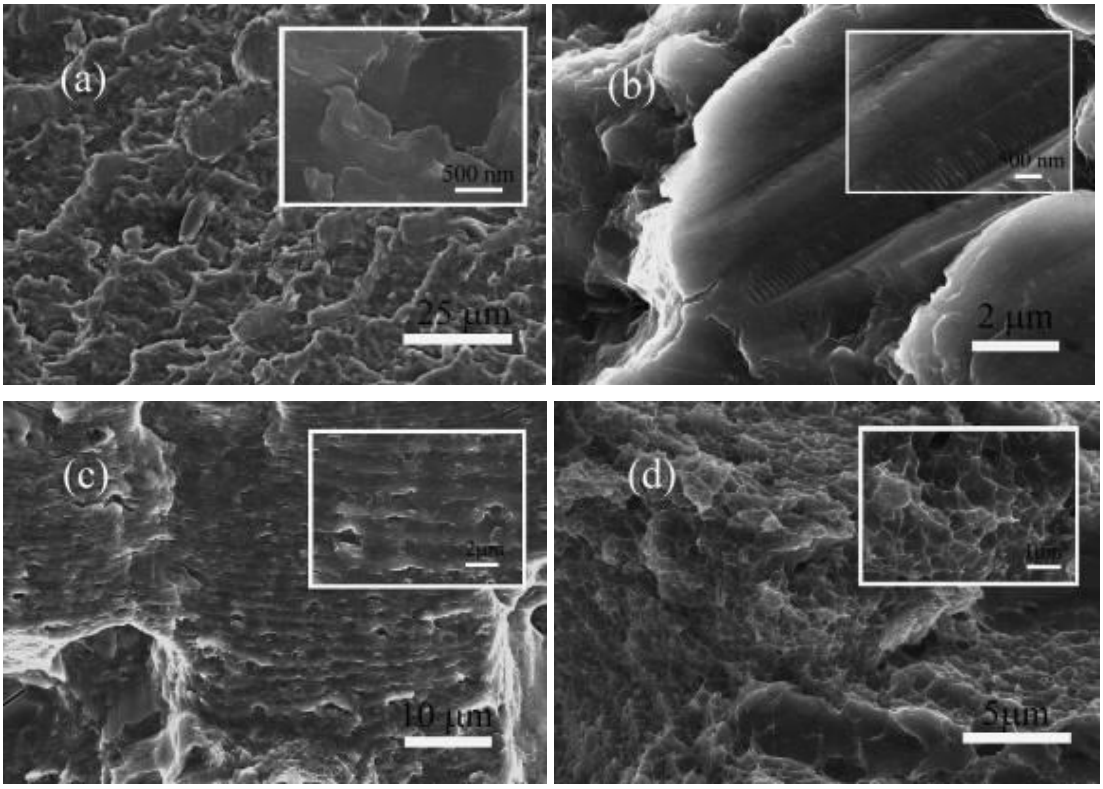

Fig. 11. The different stages of crack propagation during fatigue failure of UFG AA7075. (a) Typical stage-I crack propagation at low stress. (b) Tire track marks in the stage-I region at high stress. (c) Stage-II crack propagation with striation marks at high stress. (d) Stage-III failure by void coalescence and growth.

5. DISCUSSION

The principal difference in the microstructural evolution during fatigue of UFG AA7075 as compared to CG AA7075-T6 was with respect to their grain boundary stability. In fact, the differences in LAGB/HAGB stability justify our initial hypothesis of increased boundary

interactions in the UFG regime. The room temperature recrystallization phenomena occurring during fatigue provided supplementary evidence to these dynamics. In the following section the influence of grain boundary and second phase particles on fatigue micromechanisms are discussed in details.

5.1 Role of LAGB during UFG fatigue

The work-hardening phenomenon in a monotonically loaded f.c.c metal is classified into two main stages. This includes a short span of stage II associated with multiple slip which is followed by a prolonged stage III of dynamic recovery. Nes [34] has modeled this phenomenon as a dynamic balance between dislocations created during deformation and annihilated due to cross-slip. Kocks and Mecking [35], in their stage III work hardening model, explained dynamic recovery as a thermally assisted phenomenon, with recovery by pure mechanical means happening only at 0 K.

Compared to the monotonic stress-strain tests, stress reversals during fatigue cause a fundamental change in the dislocation dynamics. The to and fro dislocation movements during cyclic stresses results in a localized increase in vacancies [36]. Essman and Mughrabi's [2,3] analytical model on PSB formation, have highlighted this role of vacancies during fatigue. Repetto and Ortiz [37] further developed this model using a finite element based technique. A further confirmation of these vacancy effects, during fatigue, can be seen in the positron annihilation lifetime spectroscopy experiments [38]. The proximity of LAGB to HAGB in UFG metals as compared to MC counterpart, combined with the elevated vacancy concentrations is expected to stimulate conservative and non-conservative dislocation activities. Consequently, a difference in the fatigue response of UFG and MC metals is expected. An example of this was found in the electron channeling experiments on fatigue specimens of high strength low alloy steels by Keller et al [39]. In this comparative work Keller et al [39] observed a diminishing trend in the frequency of low energy dislocation structures for a fine grained (6 μm) microstructure as compared to its coarse grained (85 μm) variant.

Addressing the issue of LAGB activity in UFG AA7075 further, the principal differences observed were in the stability and mobility of LAGB with a change in the microstructural length scale. Thus, in both UFG AA7075 and CG AA7075-T6 a conspicuous increase in LMLAGB after fatigue loading was observed. However, unlike in CG AA7075-T6, the HMLAGB fraction in UFG AA7075 exhibited a decreasing trend (Fig. 6a and b). Considering the increase/decrease of different LAGB fraction in more details; logically, the change in LAGB fraction is a function of two counteracting effects a) formation of new LAGB, and b) annihilation of existing LAGB.

For the new LAGB formation; the energy of a LAGB is a function of the boundary misorientation and is expressed as [40]:

$$\gamma = \frac{\mu b}{4\pi(1-\nu)}\theta \ln\left(\frac{e\alpha}{2\pi\theta}\right) \quad (2)$$

where b is the burgers vector of dislocation, α the factor for dislocation core energy and *v* the Poisson's ratio. Consequently, an increase in the LAGB misorientation (θ) will result in an increase in the grain boundary energy. This is in contrast with the energy of a HAGB, which is virtually independent of θ (except for the special Σ boundaries with low index grain boundary planes). Thus, from the energy aspect, LMLAGB formation is favorable compared to HMLAGB.

The annihilation of a LAGB on the other hand is controlled by a) overall grain boundary mobility, and b) dislocation mobility. Addressing the issue of grain boundary mobility further, the boundary velocity (v_b) of a LAGB is expressed as [9]:

$$v_b = \frac{2c_1 MGb\theta}{R} \quad (3)$$

where M is the boundary mobility, G the shear modulus and R the radius of curvature of the boundary. A decrease in the misorientation of a LAGB is therefore accompanied by a reduction in mobility. In fact, a plot of the measured boundary mobilities with misorientation (temperature range of 473 – 723 K) displayed a sigmoidal relation between M and θ [41]. The boundary mobility decreased to a very low value for $\theta <\sim 3^{\circ}$ [41]. As a result the low energy and mobility, of LMLAGB makes them intrinsically stable. Conversely, the higher energy and mobility of HMLAGB, coupled with both conservative and non-conservative dislocation movements during fatigue, makes them inherently unstable. It may be noted that dynamic interaction effect of a low angle tilt boundary with HAGB has already been reported [42]. Thus, Jones et al. [42] in their TEM investigations on the recrystallization behavior of polycrystalline aluminum clearly demonstrated a decrease in the low angle tilt boundary misorientation (increase in individual dislocation spacing) near HAGB. This stability issue is particularly relevant for UFG metals where the proximity of HMLAGB to HAGB is an order of magnitude (or more) smaller compared to MC metals. Thus, dislocation absorption from HMLAGB to a HAGB/LMLAGB accompanied by HMLAGB disintegration is an active microstructural process in the UFG regime. The principal damage accumulation process in UFG aluminum is therefore accomplished by the

formation of LMLAGB type of boundaries. In MC metals, the LMLAGB plays a similar role by constituting the subgrain boundaries. Additionally, the HMLAGB stability in MC metals due to the length scale issues (as compared to UFG metals) provides an additional advantage with respect to dislocation storage.

The overall situation in UFG AA7075 is however expected to be somewhat more complicated. The grain boundary/matrix second phase present in UFG AA7075 will cause an additional dislocation/particle interaction effect. The consequence of this effect can be further analyzed with reference to Ashby's [43] discussion on dislocation loop and cell structure formation around dispersed particles. Thus, the preferential accumulation of LMLAGB near the unresolved regions of UFG AA7075 (Fig. 7), in both before/after fatigue conditions, clearly indicates dislocation trapping at the precipitate/particle interface. This is in contrast to the LMLAGB accumulation near the grain centers of CG AA7075-T6 (Fig. 8). To confirm this effect further, a change in the hardness of UFG AA7075 matrix after fatigue was measured (Fig. 5b). The experimentally measured values were compared with the estimated increase in hardness obtained from the Orowan-Ashby equation, which is given as [43]:

$$\Delta\sigma = \frac{0.15Gb}{\lambda}\ln\frac{r}{b} \tag{4}$$

where λ is the interparticle spacing and r the effective particle size. For the UFG AA7075 microstructure, considering λ=0.25 μm, r=0.3 μm and G=24 GPa, the maximum increase in yield strength was therefore expected to be in the range of ~25 MPa. This approximates to ~9 VPN increase in the hardness. The ~8-10 VPN increase in hardness of UFG AA7075 after fatigue at the lower stress amplitudes (up to ~270 MPa) (Fig. 5b) conforms to this expectation. The little or no change in hardness, at higher stresses for CG AA7075 T6, was typical of a precipitation hardened microstructure with shearable precipitates [5].

5.2 Recrystallization during fatigue

The phenomenon of recrystallization at high temperatures (e.g., annealing) has been broadly divided into two categories, a) static and b) dynamic. The dynamic recrystallization phenomenon is again subdivided into continuous/discontinuous types. Consider the case of static recrystallization first. Unlike in recovery, static recrystallization is a discontinuous process involving nucleation and growth. The nucleation sites being generated, by a discontinuous growth of subgrains, according to their strain energy and orientation gradients [9].The energy stored

during deformation provides the driving force for growth. In discontinuous dynamic recrystallization, the HAGB acts as nucleation sites; the dislocation density difference provides the driving force for growth. As already noted, no preexisting orientation gradient (Fig. 10a) within grain A was observed. Thus, nucleation site development for static recrystallization process is not expected. In a similar note, the occurrence of recrystallization within one single grain with no change in the original HAGB of grain 'A' indicates that the nucleation conditions for discontinuous dynamic recrystallization doesn't exist. Thus, the possibility for any discontinuous recrystallization process (static/dynamic) during fatigue of UFG AA7075 is discounted.

As already discussed (Section 5.1), a conspicuous increase in the dislocation/grain boundary interactions for UFG AA7075 was observed. This was associated with an overall decrease in HMLAGB and an increase in the LMLAGB fraction. The LMLAGB's accumulating preferentially near the dispersed second phases. The presence of such second phases (Fig. 9) would normally suggest an extended recovery type mechanism [9]. This possibility is, however, contradicted by the decrease in LMLAGB fraction from ~25% to ~ 9% accompanied by a sharp increase in HAGB of the Σ29a type (from ~5% to ~28%). This sharp transition in area misorientation from a bimodal distribution to a single peak distribution (Fig. 10b) indicates a dislocation movement, larger in scale, than that expected during dynamic recovery. Another possible argument would be to suggest the movement of LMLAGB — which however is not expected. In fact, the retained portion of LMLAGB after recrystallization (Fig. 10b) was found to be a portion of the original LMLAGB structure in grain 'A'. Additionally, the overall trend of increase in LMLAGB fraction (Fig. 6b) after fatigue, also, indicates otherwise. Thus, the possibility of a continuous dynamic recrystallization type of process is also not envisaged.

The above conflicting evidence suggests that the recrystallization phenomenon observed is probably due to some new mechanism. Alternatively, the recrystallisation observed can be a result of multiple mechanisms — possibly dynamic recovery, and subgrain rotation, all acting simultaneously. The recrystallization phenomena described here is representative of the overall UFG AA7075 microstructure. As already mentioned, no grain growth tendency was observed. This can be ascribed to the Zener pining effect of the second phases present. This lack of grain growth is in accord with Wong et al's observation [20] but is in contrast with the experiments of Walley et al [21] in UFG AA5083 alloy. The difference is of significance since the coarsening observed in UFG AA5083 alloy was accompanied with slip band formation as a damage accumulation mechanism [21]. In this context, it may be reiterated that damage accumulation in microcrystalline metals can result from both reversible and irreversible dislocation movements.

Thus, veins and cell structures formed are a consequence of reversible dislocation movement, while PSB formation is caused by irreversible motion [2]. Such irreversible dislocation motion results in crack initiation leading to failure. Although, the nature of slip bands in UFG AA5083 alloy [21] was not discussed (i.e. persistent/non-persistent), considering the low cycle fatigue (LCF) conditions these bands are expected to be a consequence of irreversible type dislocation motion. Such irreversible damage accumulation mechanism will be relevant at the late stages of life in the high cycle fatigue conditions.

5.3 Fatigue crack propagation- precipitate effect

At low stress amplitudes of testing, crack propagation in UFG AA7075 was typical of the stage-I type seen in Fig. 11a. The wavy stage –I crack propagation with tear marks (Fig. 11a inset) indicate a matrix resistance to slip characteristic of refined grain sizes [24]. The small cracks of grain size dimension (Fig. 11a inset) signify a preferential stress concentration at the grain boundary regions probably due to the presence of second phases at the grain boundaries (Fig. 3b). However, no interlinkage of cracks typical of intergranular crack propagation was observed. Therefore, such microscopic cracks are not expected to affect the fatigue life of UFG AA7075 microstructure. Considering the plastic blunting model of striation formation [44], the tear marks in the stage-II striated region indicates a difficulty in duplex slip. This is in accord with the features observed in the stage-I region and indicates an overall resistance to crack propagation in UFG AA7075 with consequent fatigue life improvement. In the final stage-III region the failure by void coalescence with precipitate particles located within the voids is typical of overload failure. In this context, it may be mentioned that a method to determine slip inhomogeneities during fatigue test is through a measurement of the tension-compression stress asymmetry [21, 45, 46]. Experiments done on AA7075-T6/T651 alloy showed a considerable tension-compression stress asymmetry [46]. The asymmetry was attributed to non-uniform slip distribution caused by a combination of inhomogeneous precipitate nucleation and the shearable nature of precipitates present in AA7075-T6/T651 microstructures [46]. Quite expectedly, no such tension-compression stress asymmetry was noted for microcrystalline AA5083 alloy at saturation due to the solid solution nature of its strengthening [21]. On the other hand, a slight tension-compression asymmetry at saturation was observed for the UFG AA5083 alloy [21]. Although, the reason for such asymmetry was not discussed by the authors, the occurrence of slip bands (possibly of persistent type) is expected to be a possible reason for such non-uniformity in slip behavior. In the current study, measurement of such tension/compression asymmetry was however not possible as the experiments were of the bending fatigue type. However, the

fractographical evidence discussed above indicates that such non-uniformity of slip will be limited for UFG AA7075. Moreover, the incoherent precipitates of ~ 50-300 nm size in UFG AA7075 were much larger than the coherent/semicoherent precipitates in AA7075 T6/T651 alloys and are of non-shearable nature [47]. This also justifies the inconsequential effect of precipitates on slip localization in the UFG AA7075 alloy as noted from the fracture surface investigation.

5.4 Role of grain size during UFG fatigue

Ever since the discovery of variability in small crack growth [48-50], the grain size effect on fatigue crack propagation has remained much debated. The complexity can be appreciated by the fact that the linear elastic fracture mechanics approach commonly used in long crack propagation studies do not apply in the short crack regime [51]. This limitation has been linked to the lack of crack tip similitude in small/long cracks [51]. It has further led to the development of a two-parameter based approach towards fracture mechanics [52-54]. Alternatively, based on the observation that grain boundaries act as a barrier to crack propagation, microstructure-based crack propagation models have also been proposed [6-7]. This microstructure-based approach leads to an inverse square root dependence of endurance limit on the grain size. To understand this effect of grain boundaries on fatigue better, the variation in fatigue life of the four different microstructures is now considered (obtained by Basquin's equation fit of data points in Fig. 3) with respect to their grain boundary strengthening (σ_{GBS}) (Fig. 12). The grain boundary strength contribution in each microstructure being obtained using the Hall-Petch relationship [55-56], which is expressed as:

$$\sigma_{GBS} = \sigma_f + k_i d^{-1/2} \tag{5}$$

where σ_f is the yield strength of aluminum single crystal (~16 MPa) and k_i the Hall-Petch constant (~0.065 MPa $m^{-1/2}$) for aluminum [57].

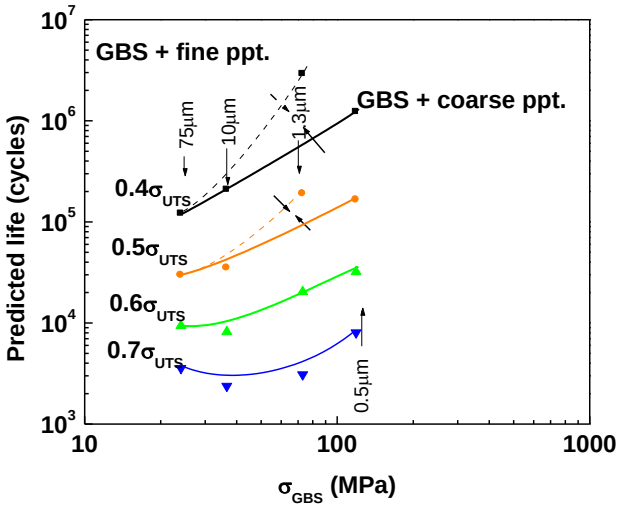

Fig. 12. The effect of grain boundary strengthening on fatigue life in a completely reversed displacement controlled test at different stress amplitude levels normalized with respect to their ultimate tensile stresses.

The key deductions from Fig. 12 can be summarized as follows:

(a) At low stress levels ($<0.5\sigma_{UTS}$), a decrease in grain size results in an improvement of fatigue life. The extent of improvement at lower stress levels ($<0.5\sigma_{UTS}$) being dependent on the nature of additional strengthening mechanisms in play. Thus, for a microstructure with fine coherent precipitates (as in GP zone hardened AA7075 T6, CG AA7075 T6 and FG AA7075) the improvement is considerably more (dotted black/orange line in Fig. 12) as compared to a microstructure with coarser precipitate like UFG AA7075. (solid black/orange line in Fig. 12).

(b) With decreasing grain size, the beneficial effect of coherent fine precipitates on fatigue life however diminishes at high stresses. This is evident in the gradual merging of the dotted orange/solid orange line at $0.4\sigma_{UTS}$ (compare with $0.5\sigma_{UTS}$) to the continuous line at $0.6\sigma_{UTS}$ (indicated by arrows in Fig. 12). Thus, the fatigue life of CG AA7075-T6 is in fact superior to AA7075-T6 and FG AA7075 at ~$0.7\sigma_{UTS}$.

(c) For a microstructure like UFG AA7075, with coarser precipitates, the improvement in fatigue life is however retained even at $0.7\sigma_{UTS}$ (see Fig. 12).

This different response of UFG AA7075 compared to CG/FG/AA 7075 –T6 heat treated

microstructure is now further rationalized with respect to the grain boundary behavior discussed in Section 5.1. The absolute difference in grain size between FG AA7075 and UFG AA7075 is in the range of ~0.7μm.Considering the length scale of dislocation movements during fatigue (as evident from the dimensions of cell sizes formed in Al).no substantial difference in their boundary behavior is therefore expected.

However, unlike in FG AA7075 the presence of dispersed second phases in UFG AA7075 makes a considerable difference. This difference was evident in the hardness increase (see Fig. 5b) with the dispersed second phases acting as preferred site for dislocation storage. The lack of coarser precipitates and the smaller grain sizes of FG AA7075 on the other hand reduced its dislocation storage capacity. Thus, beyond $0.5\sigma_{UTS}$ the fatigue life of FG AA7075 is in fact inferior compared to UFG AA7075. In fact, dislocation absorption in the grain boundary regions has been considered to be a key deformation mechanism in the ultrafine-grain regime [58, 59]. On the other hand, the large grain size of CG AA7075-T6 and resultant length scale increase (compared to AA7075-T6 / FG AA7075) is expected to reduce dislocation interactions with the grain boundary. Consequently, at the high stress levels ($0.7\sigma_{UTS}$) an improvement in fatigue life of CG AA7075-T6 with respect to AA7075-T6 /FG AA7075 is noted. It may be mentioned here that extrinsic microstructural features can significantly influence fatigue life [5]. However, such a possibility is disregarded here since all the microstructures compared (except for AA7075-T6 sheet) were processed in a similar fashion. Another potential source of fatigue life improvement for UFG microstructures at high stresses (low cycle fatigue life) is through the introduction of bimodal grain distribution [60]. However, such a possibility is disregarded for UFG AA7075 since the grain size distribution was unimodal. Also, the maximum grain size (2.5 μm) observed in UFG AA7075 was much smaller than that typically observed in microcrystalline metals. Moreover, any such life improvement at high stresses will be associated with an increased stage-I crack propagation rate and this will result in decrease of fatigue life at low stresses. The consistent fatigue life improvement of UFG AA7075 at all stress ranges therefore, rules out any possible effect from the grains with size greater than 1μm. Consequently, dislocations and their interaction with low angle boundaries and precipitates were considered to play a controlling role in determining the high cycle fatigue life of UFG aluminum.

6. SUMMARY AND CONCLUSIONS

(a) Low misorientation low angle grain boundaries ($\theta < 2.5^{\circ}$) have low mobility and low energy; as a result, an increase in the fraction of LMLAGB, for both coarse and ultrafine grain AA7075 alloy, was observed after fatigue. The LMLAGB in CG AA7075 were formed

mostly within the grain interior. In UFG AA7075, the LMLAGB accumulated near the dispersed grain boundary phases. Therefore, in UFG Al fatigue damage accumulation is accomplished principally through LMLAGB formation.

(b) Higher misorientation low angle grain boundaries ($\theta > 2.5^{\circ}$ but $< 15^{\circ}$) (HMLAGB) have high energy and higher mobility; in UFG AA7075 alloy, this results in an increased interaction between HMLAGB with the dispersed second phase and HAGB. The interaction is due to the non-conservative/conservative movement of dislocations along with the increased proximity of HMLAGB to the grain boundaries and dispersed phase. In CG AA7075-T6, the effect is not observed due to the order of magnitude increase in HAGB/HMLAGB distance.

(c) The increased activity of LAGB in UFG AA7075 is also reflected in the room temperature recrystallization phenomenon occurring during fatigue. The mechanism of recrystallization was possibly a combination of multiple processes like dynamic recovery, subgrain rotation acting together. No grain coarsening during fatigue was observed. This was due to the Zener pining effect caused by the distributed second phase.

(d) With increase in applied stress amplitude, the interaction between LAGB and HAGB increases in a precipitation hardened microstructure. In FG AA7075 and AA7075-T6, this resulted in a lowering of fatigue life; the effect was not observed in CG AA7075 due to the larger grain size. In UFG AA7075, the dispersed phase acts as a site for dislocation storage and prevents dislocation absorption by grain boundaries. Consequently, a higher fatigue life for UFG AA7075 was observed in the normalized stress amplitude scale.

Acknowledgement

The encouragement and guidance of Prof. F.S. Miller and Dr. M. Zhang in using the OIM and electron microscopes at the AMCL facility is acknowledged. Additionally, the helpful discussions on MATLAB based image processing with Mr. S. De, Ph.D candidate in electrical engineering department at Missouri S&T, is gratefully acknowledged.

REFERENCES

[1] H. Mughrabi, H. Mater. Sci. Eng. 33 (1978) 207 – 223.

[2] U. Essmann, H. Mughrabi, Phil. Mag. A 40 (1979) 731 – 756.

[3] U. Essmann, H. Mughrabi, Phil. Mag. 44 (1981) 405 – 426.

[4] Z.S. Basinski, S.J. Basinski , Prog. Mater. Sci. 36 (1992) 89 – 148.

[5] S. Suresh, Fatigue of Materials, 2nd Edn., Cambridge Univ. Press, 1998.

[6] K. Tanaka, Y. Nakai, M. Yamashita, International Journal of fracture 17 (1981) 519 – 533.

[7] A. Navarro, E.R. De Los Rios, Phil. Mag. A 57 (1988) 37 – 42.

[8] V. Randle, O. Engler, Introduction to texture analysis Macrotexture, Microtexture and Orientation Mapping: Gordon and Breach Science Publishers, 2000.

[9] F.J. Humphreys, M. Hatherly, Recrystallization and Related Annealing Phenomenon, 1st Edn.: Elsevier Science, 1995.

[10] O. Vorren, N. Ryum, Acta Metall., 36 (1988) 1443 – 1453.

[11] Y. El-Madhoun, A. Mohammed A, M.N. Bassim, Mater. Sci. Eng. A 359 (2003) 220 – 227.

[12] C.E. Feltner, Acta Metall. 11 (1963) 817 – 828.

[13] W. Vogel, M. Wilhelm, V. Gerold, Acta Metall. 30 (1982) 21 – 30.

[14] D.J. Duquette, P.R. Swann, Acta Metall. 24 (1976) 241 – 248.

[15] S.R. Agnew, J. Weertman, Mater. Sci. Eng. A 244 (1998) 145 – 153.

[16] S. Hashimoto, Y. Kaneko, K. Kitagawa, A. Vinogradov, R.Z. Valiev, Mater. Sci. Forum 312-314 (1999) 593 – 598.

[17] H.W. Hoppel, Z.M. Zhou, H. Mughrabi, R.Z. Valiev, Phil. Mag. A 82 (2002) 1781 – 1794.

[18] S.R. Agnew, A.Y. Vinogradov, S. Hashimoto, J.R. Weertman, J. Electron Mater. 28 (1999) 1038 – 1044.

[19] H.W. Hoppel, C. Xu, M. Kautz, N. Barta-Schreiber, T.G. Langdon, H. Mughrabi, In: M.J. Zehetbauer, R.Z. Valiev editors. Proceedings of second international conference on nanonmaterials by severe plastic deformation. Winheim: Wiley-VCH (2004) 677 – 683.

[20] M.K. Wong, W.P. Kao, J.T. Lui, C.P. Chang, P.W. Kao, Acta Mater. 55 (2007) 715 – 725.

[21] J.L. Walley, E.J. Lavernia, J.C. Gibeling, Metall. & Mater. Trans 40A (2009) 2622- 2630

[22] R.S. Mishra, M.W. Mahoney, S.X. Mcfadden, N.A. Mara, A.K. Mukherjee, Scripta Mater. 42 (1999) 163 – 168.

[23] I. Charit, R.S. Mishra, Acta Mater. 53 (2005) 4211 – 4223.

[24] P.S. De, R.S. Mishra, C.B. Smith, Scripta Mater. 60 (2009) 500 – 503.

[25] P.S. De, C.M. Obermark, R.S. Mishra, J. Test & Eval. 36 (2008) JTE101669.

[26] R.S. Mishra, S.R. Sharma , M.A. Mara, M.W. Mahoney, ASM International Joining of Advanced and Specialty Materials III 2001; 157.

[27] G.F. Vander Voort, Metallography principles and practice, McGraw-Hill, New York, 1999.

[28] J.E. Hatch, Aluminum Properties and Physical Metallurgy, ASM, 1984.

[29] M.D. Abramoff, P.J. Magelhaes, S.J. Ram, Biophotonics Inter. 11 (2004) 36 – 42.

[30] D.J. Lloyd, L.R. Morris, Acta Metall. 25 (1977) 857 – 861.

[31] D.J. Lloyd, Met. Sci. 14 (1980) 193 – 198.

[32] R. Mahmudi, Mater. Lett. 19 (1994) 243 – 246.

[33] G.E. Dieter, Mechanical Metallurgy, SI Edn., McGraw-Hill Publishing, 1988.

[34] E. Nes, Prog. Mater. Sci. 41 (1998) 129 – 193.

[35] U.F. Kocks, H. Mecking, Prog. Mater. Sci. 49 (2003) 171 – 273.

[36] J.G. Antonopoulos, L.M. Brown, A.T. Winter, Phil. Mag. 34 (1976) 549 – 563.

[37] E.A. Repetto, M. Ortiz, Acta Mater. 45 (1997) 2577 – 2595.

[38] T.L. Grobstein, S. Sivashankaran, G. Welsch, N. Panigrahi, J.D. McGervey, J.W. Blue, Mater. Sci. Eng. A 138 (1991) 191 – 203.

[39] K. Keller, W. Zielinski, W.W. Gerberich, Mater. Sci. Eng. A 113 (1989) 267 – 280.

[40] J.P. Hirth, J. Lothe, Theory of dislocations, McGraw-Hill Book Company, 1968.

[41] F.J. Humphreys Acta Mater. 45 (1997) 4231 – 4240.

[42] A.R. Jones, B. Ralph, N. Hansen, Proc. R. Soc. Lond. A 368 (1979) 345 – 357.

[43] M.F. Ashby, In: Editors. Proceedings Second Bolton Landing Conf. on Oxide Dispersion Strengthening: Gordon and Breach, science publishers Inc. (1968) 143-205.

[44] Laird C.: Fatigue Crack Propagation, ASTM-STP 415 (1967) 131-168.

[45] B.T. Ma, Z.G. Wang, A.L.Radin, C. Laird, Mater. Sci. Eng. A 129 (1990)197-206.

[46] J.M. Meininger, S.L. Dickerson, J.C. Gibeling, Fatig. Fract. Engng. Mater. Struct. 19 (1996) 85-97.

[47] R.E. Stoltz, R.M. Pelloux, Metall. Trans. A 7 (1976) 1295-1306.

[48] S. Pearson, Eng. Fract. Mech. 7 (1975) 235 - 247.

[49] W.L. Morris, Met. Trans. A 11 (1980) 1117 – 1123.

[50] J. Lankford, Fatig. Of Eng. Mater. Struc. 5(1982) 233 – 248.

[51] S. Suresh, Met. Trans. A 14 (1983) 2375 – 2385.

[52] A.K. Vasudevan, K. Sadananda, N. Louat, Scripta Metall. Mater. 28 (1993) 65 – 70.

[53] A.K. Vasudevan, K. Sadananda, N. Louat, Mater. Sci. Eng. A 188 (1994) 1 – 22.

[54] K. Sadnanda, A.K. Vasudevan, Int. J. Fatig. 26 (2004) 39 – 47.

[55] E. Hall, Proc. Phys. Soc. Lond. B 64 (1951) 747 – 753.

[56] N.J. Petch, J Iron Steel Inst. 174 (1953) 25 – 28.

[57] M. Dixit, R.S. Mishra, K.K. Sankaran, Mater. Sci. Eng. A 478 (2008) 163 – 172.

[58] F.Tang, J.M. Schoenung, Mater. Sci. Eng. A 493 (2008) 101 – 103.

[59] W.Blum, X.H. Zheng, Acta mater. 57 (2009) 1966 – 1974.

[60] H. Mughrabi, H.W. Höppel, Inter. J.of Fatig. 32 (2010) 1413–1427.

V. A STRESS-STRAIN MODEL FOR A TWO PHASE ULTRAFINE GRAINED ALUMINUM ALLOY

P.S. De, J.Q. Su and R.S. Mishra

Center for Friction Stir Processing, Department of Materials Science and Engineering

Missouri University of Science and Technology, Rolla, MO 65409

ABSTRACT

Two phase ultrafine grained (UFG) aluminum alloy with different precipitate and low angle boundary distributions were examined for their monotonic stress-strain behavior. Precipitates in combination with low angle grain boundaries were found to determine the deformation micromechanism. It is proposed that thermally activated vacancy movement plays a central role in this regard. The experimental stress-strain curves matched well with the trend predicted by a modified Blum-Zheng model based on vacancy assisted dislocation annihilation mechanism.

Keywords: Ultrafine grained microstructure, Ductility, Orientation imaging microscopy (OIM), Grain Boundaries.

Ultrafine grained aluminum alloys are generally characterized by unique stress strain features. Thus, in one of the earliest works on extruded/extruded-cold worked UFG-Al (grain size 0.5 – 2 μm), a small yield point (YP) phenomena was reported [1, 2]. More recently UFG Al alloys, processed using the severe plastic deformation (SPD) technique, have been found to possess a low uniform ductility [3]. Exceptions to this trend were also reported e.g. a reduction in the applied strain rate (from 10^{-2} $s^{-1}$to less than 10^{-4} s^{-1}) resulted in increased uniform ductility (from 1% to ~20%) [4,5]. This increase was, however, accompanied by a decrease in the ultimate tensile strength. In contrast, fine grained Al-Mg [7] and AA7075 [8] alloys produced using friction stir processing (FSP) showed an improved uniform elongation even at normal strain rates of testing. Thus in UFG-Al, a pronounced variation in ductility with processing and microstructural variation is observed. This paper reports on the effects of grain boundaries and precipitates on the ductility of a two phase UFG Al alloy from a micro-mechanical viewpoint.

The starting material for this work was a commercially available AA7075-T6 sheet approximately 3.2 mm thick, which was solutionized and processed using a friction stir tool. The processed material (nugget region only) was air cooled to obtain a UFG AA7075 microstructure

(henceforth UFG-NHT), a portion of which was further aged at 423 K for 24 hours to produce a second microstructural variant (henceforth UFG-423K). At this point, it should be recalled that aging of a precipitation hardened material is associated with recovery and second phase coarsening [9]. Therefore, although both UFG-NHT/UFG-423K were similar in grain size (0.6 μm), a significant difference in precipitate and low angle grain boundary (LAGB) distribution was expected. Accordingly, considerable differences were observed in the orientation imaging microscopy (OIM) images for UFG-NHT and UFG-423K (Fig. 1). Thus, unlike UFG-423K, in UFG-NHT apart from the grain boundary precipitates, an intragranular precipitate distribution was noted (unindexed black spots in Fig. 1). These distributed precipitates were associated with a dense LAGB network of misorientation < 3˚ (henceforth Low Misorientation (LM) LAGB). On the other hand, the lack of intragranular precipitates in UFG-423K resulted in a matrix which was relatively free of LMLAGBs. All mechanical characterization in this work was conducted using a computer controlled, screw-driven tensile testing machine at constant crosshead velocity. A mini-tensile specimen, with gage length 2.3 mm, thickness 1 mm and width/thickness ratio of 1.16, at two different initial strain rates (10^{-2} s^{-1} and 10^{-4} s^{-1}) were used. In Table 1 the stress-strain properties of the two microstructures at two different average strain rates are summarized. One of the remarkable features of the stress-strain curves was the presence of YP with a dynamic strain aging tendency. The trend was prominent in UFG – NHT, and decreased to a nominal extent in UFG-423K. It may be added here that Mg atoms in Al have been associated with a dynamic strain aging effect. Therefore, the decreased YP/dynamic strain aging of UFG-423K indicates a reduction in Mg concentration within the matrix.

Another highlight of the stress-strain experiments was the extended uniform ductility of UFG-NHT with a decrease in the strain rate (see Table 1). However, unlike ECAP Al/Al alloy [4-5], no strength decrease with an increase in ductility was noted. In this context, the effect of LMLAGB on the properties of UFG-Al properties needs further elucidation. The influence of LMLAGB on UFG-Al is expected to be twofold: (i) on strengthening mechanism, and (ii) on diffusion behavior. Considering the strengthening effects first, depending on boundary mis-orientation, grain boundary strengthening in metals is classified into two types: (i) due to boundary spacing (i.e. Hall-Petch type strengthening); or (ii) due to dislocations within boundary (i.e. proportional to the square root of dislocation density within the boundary) [6]. In UFG Al, grain boundaries with misorientation greater than 2-3˚, were found to provide a strengthening effect of the Hall-Petch type (i.e. proportional to $d^{-1/2}$ where d is the boundary spacing) [6]. Boundaries with misorientation less than 2-3˚ (i.e. LMLAGB) impart a strengthening effect of the second type [6]. Thus, despite a similarity in grain size, the LMLAGB present in UFG-NHT

resulted in a higher yield strength compared to UFG-423K (Table 1). The corresponding flow stress increase due to LMLAGB can be expressed as [6, 12],

$$\tau = \alpha' Gb\sqrt{\rho_{LM}} \quad (1)$$

where α' is the effective dislocation interaction constant [12], G the shear modulus, b the Burgers vector and ρ_{LM} the density of dislocations in LMLAGB. Here, it may be recollected that application of strain results in two possibilities: (i) creation of new dislocations; and (ii) annihilation of dislocations produced (as discussed later). The new dislocations created (which move and form LMLAGB) increase the flow stress, resulting in a work hardening effect. The second phases present (as in UFG-NHT/UFG-423K) here acts as pinning points for these LMLAGB structures. The effect was clearly observed in the OIM image of Figure 1 where LMLAGB structures clustered around the unresolved points. An alternative estimate of dislocation density in LMLAGB structures can be obtained from the standpoint of geometrically necessary dislocations (GNDs). Thus, shear stress in a material containing non-shearable particles can result in the creation of GNDs of the edge dislocation type (Fig. 2). Here, it may be mentioned that, depending on the particle location (i.e. grain boundary/matrix) and slip plane orientations, other dislocation arrangements can also exist. A rough estimate of this increase in GND with strain was given as [13]

$$\rho_{GND} = \frac{4 \cdot f \cdot \gamma}{b \cdot r} \quad (2)$$

where f is the precipitate volume fraction, r the precipitate radius and γ is the applied strain. Therefore, for the purpose of this work, the increase in dislocation density at LMLAGB (i.e. ρ_{LM}) has been equated with the increase in ρ_{GND} with straining.

Next, let us consider the influence of LMLAGB on diffusivity. At room temperature, bulk diffusion is the primary rate controlling process in microcrystalline aluminum. However, the increased fraction of LMLAGB and high angle grain boundaries (HAGBs) in UFG-Al causes a substantial change in diffusivity. An example of this change was observed in the increased inter-diffusivity of Mg in Al of a UFG Al-Mg alloy [10]. Similar work on ECAP copper at ~$0.36T_m$ exhibited grain boundary diffusion in the Harrison's C regime [11], indicating an active diffusive path along the grain boundaries [11]. Consequently, for UFG-NHT/UFG-423K an increased

vacancy diffusivity was expected. It should be emphasized that migration of vacancy was considered as the diffusion rate controlling step here. In this context, the thermal activation based deformation model for single phase UFG metals by Blum and Zheng [12] needs special mention (referred to as Blum-Zheng model). According to their hypothesis, edge dislocation dipole annihilation constitutes the principal UFG deformation micromechanism [12].

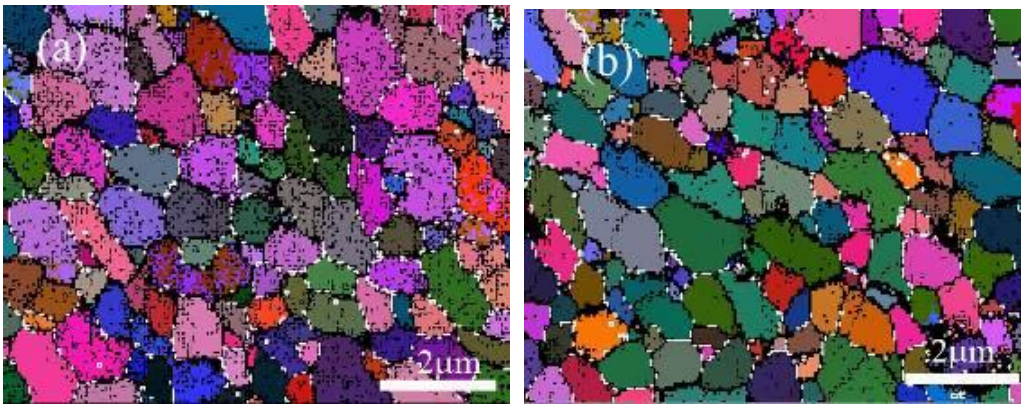

Figure 1. (a) OIM image of UFG-NHT in Euler angle coloring (EAC) showing extensive grain boundary and matrix second phase (thick black lines and dots). The LMLAGB (thin dark lines) are mostly trapped near the matrix second phase. (b) OIM image of UFG-423K in EAC showing grain boundary precipitates with occasional matrix second phase. The frequency of LMLAGB is much reduced compared to UFG-NHT.

Table 1. Summary of tensile results showing the variation of yield stress (σ_{ys}), ultimate tensile stress (σ_{uts}) and uniform ductility (ε_u) with strain rate of testing ($\dot{\varepsilon}$). Two specimens were tested for each condition.

Microstructure	$\left(\dot{\varepsilon}\right)_{s^{-1}}$	**σ_{ys} (MPa)**	**σ_{uts} (MPa)**	**ε_u (%)**	**ε_t(%)**
UFG-NHT	0.01	360±25	441±22	17±1	26.2±0.0
	0.0001	374±24	461±20	20.4±0.0	32.4±1
UFG-423K	0.01	311±28	366±19	10.5±1	28.5±1
	0.0001	305±31	365.5±15	10.6±1	31±2

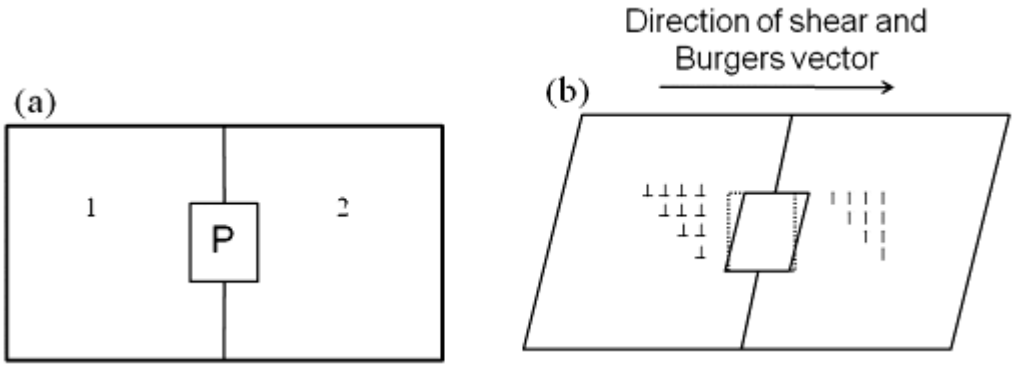

Figure 2. (a) A non-deformable particle (P) sitting at the boundary of two grains 1 and 2 (adapted from [13]). (b) The grain shape after an applied deformation. Note the expected shape change of the hole accommodating particle (P) in bold. The possible combination of edge dislocations restoring the matrix to accommodate P (shown in dots) is shown (adapted from [13]).

Any edge dislocation dipole annihilation process is accompanied by the formation of vacancies. Therefore, in UFG-Al generation of vacancies is not expected to be a rate limiting factor. This would, however imply a dynamic equilibrium between localized vacancy excess regions at edge dislocation dipole annihilation sites and grain boundaries/matrix. Consequently, in UFG-Al the influence of vacancy formation on diffusivity was considered to be of secondary importance. In the remaining part of this paper, the Blum-Zheng model (with some modifications) was used to explain the stress-strain behavior of UFG microstructure in more detail.

According to the Blum-Zheng model, edge dislocation dipole annihilation in UFG metals is a consequence of, (i) spontaneous annihilation, and (ii) thermally activated annihilation [12]. Intragranular dislocation storage was considered to be negligible [12]. However, spontaneous annihilation, though valid for cyclically loaded metals (as evidenced by localized vacancy supersaturation), was not expected to be significant during monotonic loading. Hence, for this work, only thermally activated dislocation dipole annihilation was considered. It may be clarified here that such edge dislocation dipoles were assumed to form even in the proximity of second phases. Thus, dislocation loops with opposite Burgers vector interact with the precipitate stress fields, forming low energy structures. The pre-existent as well as the LMLAGB network created during straining promotes dislocation dipole annihilation both within the grain as well as at the

interfacial regions. Another modification with respect to the Blum-Zheng model was with regards to their dislocation storage hypothesis. As already mentioned, in the current work dislocation storage near second phase was incorporated by using the GND estimates obtained from Eq. (2). Thus, for UFG-NHT application of strain results in a dynamic balance between dislocations created (as LMLAGB) and annihilated both within grains and at the grain boundaries. However, in UFG-423K specimens the deformation process is localized at the grain boundary regions only. At this point, it may be mentioned that strain localization at the grain boundary second phase results in triaxial stresses with consequent failure. Accordingly, for UFG-423K no variation in uniform ductility with strain rate was observed. Conversely, a more homogeneous strain distribution in UFG-NHT resulted in an increased uniform ductility with a decrease in strain rate, similar to Refs. [4,5]. The observed increase, was however lower compared to Refs. [4,5], since the substantial amount of grain boundary precipitate in UFG-NHT ultimately leads to a strain localization effect. Approximately similar total uniform elongation in UFG-NHT and UFG-423K specimens provides additional support to the above explanation (Table 1).

Similar to microcrystalline metals, the dislocation generation rate of UFG metals can be expressed as [12, 14]:

$$\frac{d\rho}{d\gamma} = \frac{2}{bd} \tag{3}$$

where γ is the applied strain and d is the grain size. Considering edge dislocation dipole formation and annihilation as the primary deformation mechanism, the density of dislocation dipoles formed at boundaries/interfaces (ρ_{dip}) may be expressed as [12]:

$$\rho_{dip} = f_{dip} \cdot \rho; \text{ where } 0 < f_{dip} \leq 1 \tag{4}$$

where f_{dip} is a fraction of total dislocation density ρ. The rate of thermally activated annihilation of dislocation dipoles ($\dot{\rho}^{-therm}$) is then given as [12],

$$\dot{\rho}^{-therm} = \rho_{dip} \cdot \nu_{c,b} \tag{5}$$

where $\nu_{c,b}$ is the dipole dissolution frequency at the boundaries/interfaces, and is specified as [12],

$$\nu_{c,b} = \frac{V_{dc}}{s_b} \tag{6}$$

where s_b is the dislocation dipole distance, while V_{dc} is the velocity of dislocation climb and can be expressed as a product of vacancy mobility (M_v) and the pressure acting ,

$$V_{dc} = M_v \cdot \sigma_c \cdot b \cdot s_b \tag{7}$$

where M_v equals D_b/kT (D_b is the vacancy diffusivity), and σ_c is the attractive stress between two opposite edge dislocations in a dipole and is calculated as [12]

$$\sigma_c = f_{rel} \cdot \frac{G \cdot b}{2\pi \cdot (1-\nu) \cdot s_b} \tag{8}$$

Combining equations (5 – 8) we get,

$$\dot{\rho}^{-therm} = \frac{f_{dip} \cdot f_{rel} \cdot G \cdot D_b \cdot b^2}{2\pi(1-\nu) \cdot k \cdot T \cdot s_b} \cdot \rho \tag{9}$$

At steady state, the net dislocation generation rate is equivalent to the balance between the rate of mobile dislocations annihilated and stored and is given as,

$$\dot{\rho} = \dot{\rho}^{-therm} - K_s \tag{10}$$

where K_s is the dislocation storage rate term. Assuming a uniform dislocation accumulation rate with strain, K_s can then be estimated by dividing the total dislocations accumulated (from Eq. 2) with the total time of straining. Equating the total straining time, with the testing time ($\varepsilon_u/\dot{\varepsilon}$), the estimated value of K_s is,

$$K_s = \frac{4 \cdot f \cdot \gamma \cdot \dot{\varepsilon}}{b \cdot r \cdot \varepsilon_u} \tag{11}$$

Combining equations (4) (10) and (11), and replacing ρ (the total dislocation density) with an expression in terms of τ from equation (1):

$$\dot{\gamma} = f_{dip} \cdot \frac{\tau^2}{\alpha'^2 \cdot G \cdot M^2} \cdot \frac{b}{s_b} \cdot \frac{D_b}{k \cdot T} \cdot f_{rel} \cdot \frac{d}{4\pi \cdot (1-\nu)} - \frac{2 \cdot f \cdot d \cdot \gamma \cdot \dot{\varepsilon}}{r \cdot \varepsilon_u} \tag{12}$$

Substituting, γ with ε ($\gamma = M\varepsilon$) and τ with σ ($\sigma = M\tau$) [15], in equation (12), we get,

$$\varepsilon = \theta \cdot \sigma^2 - \lambda \tag{13}$$

where θ and λ are material constants and is expressed as,

$$\theta = \frac{f_{dip} \cdot b \cdot D_b \cdot f_{rel} \cdot r \cdot \varepsilon_u}{8\pi \cdot s_b \cdot M^3 \cdot \alpha'^2 \cdot k \cdot T \cdot (1-\nu) \cdot G \cdot f \cdot \dot{\varepsilon}} \tag{14}$$

$$\lambda = \frac{r \cdot \varepsilon_u}{2 \cdot f \cdot d} \tag{15}$$

To determine the theoretical θ and λ values (Table 3) the estimates of individual variables in Eqs. (14) and (15) (see Table 2) can be used. A further validation of the model was then done by fitting the stress data for UFG-NHT and UFG-423K using a non-linear multiple regression technique.

In Figure 3, the fitted stress-strain curves along with the experimental results for UFG-423K and UFG-NHT are plotted. The general trends of the fitted stress-strain curves match well with the experimental stress-strain curves. The parameter θ measures the extent of dislocation annihilation; therefore, the similarity in fitted values with theoretical range indicates that the basic premise of the model is correct. On the other hand, the fitted values of λ are consistently lower as compared to the theoretical values. This probably indicates a systematic error, due to the nature of approximations used in Eq. (2).

Table 2. Value of different parameters used in Eqs. 14 & 15 in SI units.

Parameter (Unit)	Approx. magnitude
D_b (m^2/s)	~$6*10^{-20}$ [16]
b (m)	$2.58*10^{-10}$ [16]
d (m)	~$0.5*10^{-6}$
f_{rel}	0.5 [12]
M	2.5
α’	~0.3 [12]
r (m)	$100*10^{-9}$
f	0.06
G (N/m^2)	$25.4*10^{10}$ [16]
S_b (m)	10^{-6} to 10^{-8}*
f_{dip}	0.5*
ν	0.3
k (J/mole.K)	$1.38*10^{-23}$

* these are estimates.

Table 3. Summary of A, B and C for the different experimental conditions used in this work.

Microstructure	Strain rate	Θ	λ
UFG NHT	0.01	$1.369*10^{-18}$	0.152
	0.0001	$1.462*10^{-18}$	0.160
UFG-423K	0.01	$1.041*10^{-18}$	0.147
	0.0001	$9.993*10^{-19}$	0.151
Theoretical range		$3.7*10^{-17}$ to 10^{-21}	0.25

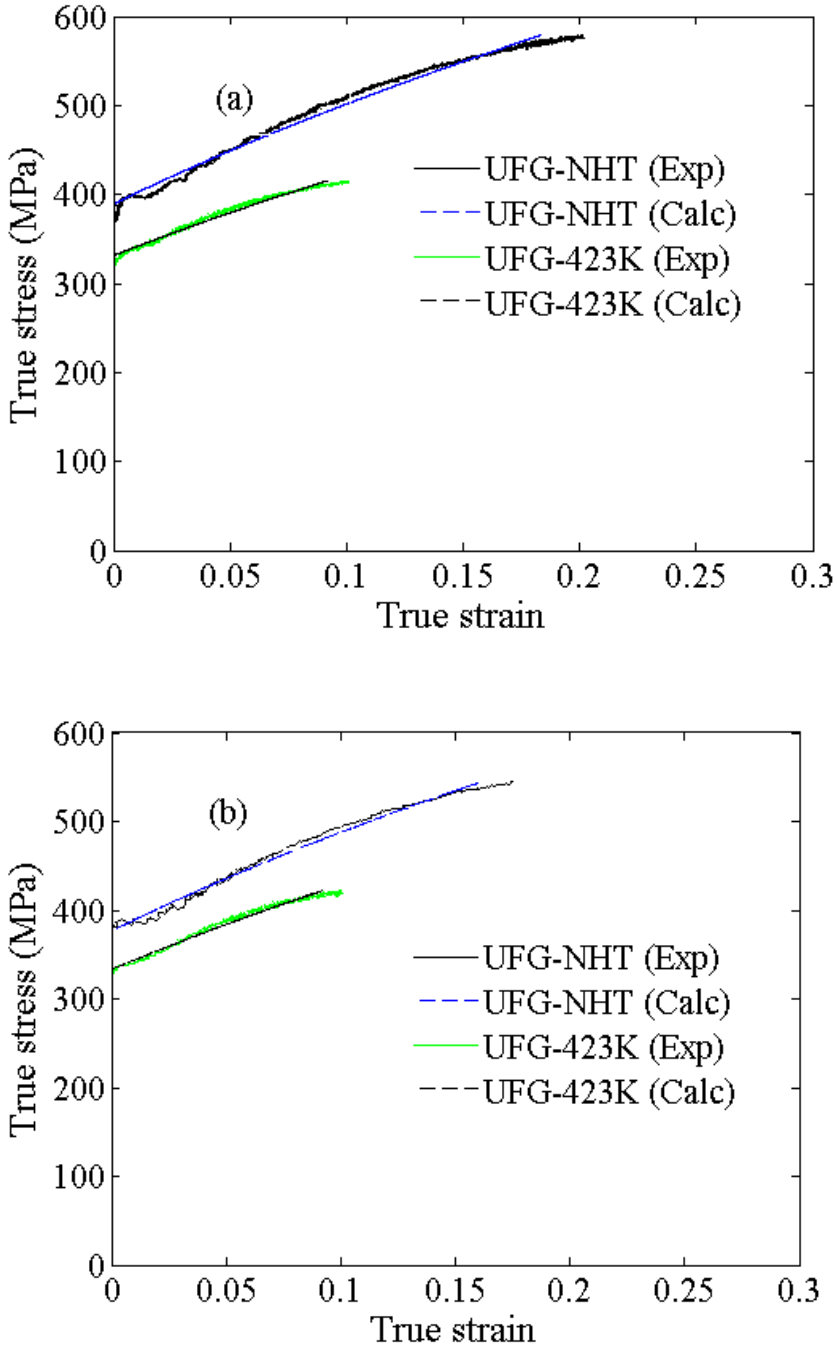

Figure 3. Plot of calculated versus experimental stress-strain curve using str**e**ss-time data: (a) UFG-NHT and UFG-423K at strain rate 0.0001 s^{-1}. (b) UFG-NHT and UFG-423K at strain rate 0.01 s^{-1}.

In summary, a vacancy based model based on the Blum-Zheng model for two phase UFG-Al deformation has been proposed. The key issues in UFG deformation mechanism are therefore presented as follows:

1. In two phase UFG-Al alloys, thermally activated vacancy movement and consequent dislocation annihilation along with dislocation storage near second phases plays a significant role during the deformation process.
2. Such dislocation annihilation can occur both at the grain boundaries and near intragranular second phases, depending on the inherent microstructural characteristics. Thus, a pre-existing low angle boundary network will promote dislocation annihilation uniformly throughout the matrix and vice-versa.
3. Dislocation annihilation and storage near the matrix second phase due to a pre-existing low angle boundary network causes a simultaneous increase in ductility without any reduction in strength.
4. The strain (ε), stress (σ) and time (t) for the UFG Al alloy tested at constant strain rate monotonic tests are related by a simple model of the form, $\varepsilon = \theta \cdot \sigma^2 - \lambda$, where θ, and λ are microstructural constants.

[1] G. Deep and A. Plumtree, Metall. Trans. A 6A (1975) 359.

[2] D.J. Lloyd, L.R. Morris, Acta Metall. 25 (1980) 857.

[3] R. Kapoor, P.S. De, R.S. Mishra, Mater. Sci. for. 633-634 (2010) 165.

[4] J. May, D. Amberger, M. Dinkel, H.W. Hoppel, M. Goken, Mater. Sci. Eng. A 483-84 (2008) 481.

[5] I. Sabirov, Y. Estrin, M.R. Barnett, I. Timokhina, P.D. Hodgson, Scripta Mater. 58 (2008) 163.

[6] N. Kamikawa, X. Huang, N. Tsuji, N. Hansen, Acta Mater. 57 (2009) 4198.

[7] R. Kapoor, N. Kumar, R.S. Mishra, C.S. Huskamp, K.K. Sankaran, Mater. Sci. Engg. A doi. 10.1016/j.msea.2010.04.086.

[8] P.S.De, R.S.Mishra, C.B.Smith, Scripta Mater. 60 (2009) 500.

[9] F.J. Humphreys, M. Hatherly, 1st Edn., Recrystallization and related annealing phenomena, Elsevier Science Ltd. 1995.

[10] T. Fujita, Z. Horita, T.G. Langdon, Mater. Sci. Eng. A 371 (2004) 241.

[11] Y. Amouyal, S.V. Divinski, L. Klinger, E. Rabkin, Acta Mater. 56 (2008) 5500.

[12] W. Blum, X.H. Zheng, Acta Mater. 57 (2009) 1966.

[13] J.W. Martin, Micromechanisms in particle hardened alloys, Cambridge University Press 1980.

[14] U.F. Kocks, H. Mecking, Prog. in Mater. Sci., 48(2003) 171.

[15] G.E. Dieter, Mechanical metallurgy, 3rd Edn., McGraw-Hill Book company 1986.

[16] H.J. Frost, M.F. Ashby, Deformation –mechanism Maps, Pergamon Press 1982.

SECTION

2. CONCLUSIONS

Development of light weight, high strength metals continues to be a particular thrust area for materials scientists. Consequently, research on ultrafine grain aluminum with high strength and ductility has assumed special significance. This work, evaluated the ductility and high cycle fatigue life of a friction stir processed ultrafine grain aluminum alloy at the microstructural level to identify the structure-property correlations.

The primary challenge in evaluating the properties of friction stir processed ultrafine grained alloy was to have a suitable testing system. Standard mechanical testing methods require a considerable volume of material and are therefore not suitable for testing friction stir processed metals. Consequently, a sub-size fatigue testing procedure was developed. The development process comprised of understanding the stress states existing within the specimen and its effect on fatigue life. This was followed by a sensitivity check of the overall testing system.

To understand the nature of stresses in the subsize fatigue specimen, a three-dimensional finite element analysis under elastic conditions was done. Under the given loading and boundary conditions, the stress state was found to be a combination of uniaxial and plane stress. The specimen was then used to determine the fatigue life of a AA7075-T6 alloy sheet which was then compared with the standard bending fatigue specimen data obtained from literature. The results indicated that the subsize testing setup and the plane stress state of the specimen did not significantly alter the bending fatigue life. To further evaluate the testing system, an Al-Li alloy with different heat treatment conditions (T3, T8) was examined. The results indicated that depending on grain size, precipitate nature and texture, the subsize fatigue life changed as expected. This demonstrated the sensitivity of the subsize fatigue specimen to microstructural changes.

Subsequently, the testing method was used to assess the fatigue life and microstructural damage evolution in an ultrafine grained aluminum alloy. A comparative approach was adopted, where a material of the same composition (AA7075 alloy) but different grain sizes were analyzed. To evaluate the surface microstructural changes during fatigue, orientation imaging microscopy was done. The results showed that in the ultrafine grain regime low angle grain boundaries with misorientation $\leq 2.5°$ were stable irrespective of grain size. This correlated with the low energy and mobility of such boundaries. Conversely, low angle grain boundaries with misorientation $\geq 2.5°$ showed a definite instability. The effect was ascribed to the higher energy and mobility of such boundaries. The fatigue damage due to reversible dislocation motion was

therefore accommodated primarily by the low misorientation low angle grain boundaries. Similarly, recrystallization phenomenon occurring during fatigue indicated that high angle grain boundaries were also unstable. However, due to Zener pining effect of second phase particles, no grain growth during fatigue was observed. An overall improvement in high cycle fatigue life was noted. This was attributed to the increased dislocation storage at second phase particles which counteracted the effect of grain size decrease.

Finally, the relation between monotonic ductility and microstructure in ultrafine grained aluminum was investigated. The ductility was observed to depend on the density of low misorientation ($\leq 2.5°$) low angle grain boundary along with the size and distribution of second phase particles present. Increased low misorientation low angle grain boundary density resulted in an improved uniform elongation. Additionally, intragranular second phase particles resulted in an improved work hardening behavior. However, second phase particles present at the grain boundaries, reduced the uniform elongation. From these results, the deformation micromechanism was inferred to be controlled by a dynamic balance between annihilation of edge dislocation dipoles and geometrically necessary dislocations stored. A stress-strain model proposed on the above basis followed the experimental trends. This demonstrated that the basic assumptions about ultrafine grain metal deformation micro-mechanisms were valid.

2.1 DISSERTATION CONTRIBUTIONS

The objective of this dissertation was to develop a comprehensive understanding of friction stir processed ultrafine grained aluminum alloy. The salient contributions of this work are:

a) A comprehensive subsize fatigue testing bed was developed. The testing system accurately detected the variations in cyclic loading properties of metals subject to subtle microstructural changes. Consequently, this has provided an ideal platform to determine fatigue life of newer metals and materials at a laboratory scale from small sample volumes.
b) An in-depth understanding of the grain boundary behavior during high cycle fatigue in a two phase ultrafine grained aluminum alloy was accomplished. The factors necessary to improve high cycle fatigue life in an ultrafine grain aluminum alloy were identified.

c) The role of grain boundary and second phase in ultrafine grain aluminum monotonic ductility was ascertained. A model to predict the stress-strain curve of two phase ultrafine grain aluminum alloys was proposed.

2.2 FUTURE WORK

The present dissertation has focused on the fundamental deformation aspects of ultrafine grained aluminum alloys. The results indicate that microstructure - mechanical property interaction in ultrafine grain aluminum is a function of both slip and diffusion based processes. The additional topics needing further investigation in future can therefore be categorized into three groups:

1. Diffusion related: Vacancy diffusion has been predicted to be an important part of ultrafine grained aluminum alloy deformation micro-mechanisms. Therefore, a comprehensive measurement of diffusivity in different ultrafine grain alloys needs to be done. Further, depending on the processing route substantial differences exist in the low angle boundary density of ultrafine grain aluminum alloys. This is expected to cause changes in the net diffusivity. Similarly, presence of internal cracks in ultrafine grain metals can create time dependent diffusivity. Therefore, the factors controlling diffusion in ultrafine grain aluminum needs a more thorough and consistent investigation.
2. Grain boundary related: Low angle grain boundaries beyond a certain misorientation angle were found to be unstable in ultrafine grain aluminum during cyclic loading. This aspect of grain boundary stability needs to be further analyzed since it will profoundly influence cyclic and monotonic loading conditions by affecting cell structure formation. Another perceived effect will be on the crack tip plasticity of metals particularly through its influence on the plastic constraint conditions present. Similarly, instability of high angle grain boundaries as observed in the recrystallization behavior opens up a new research domain. In fact, a controlled recrystallization without grain growth leading to strain energy release can be used to reverse fatigue damage due to reversible dislocation movement. Therefore, further study about grain boundary stability in ultrafine grained aluminum is of both fundamental and technological importance.
3. Second phase related: In the ultrafine grain aluminum alloy studied, the second phase particles present were mostly in the size range of 50 -300 nm and were equiaxed in shape. A precipitate shape change will however change the strain and strain gradient distributions. This is expected to cause changes in the ductility behavior. Again, considering that second phases improve the ductility by storing dislocations, an optimum size distribution of precipitates will

be critical to achieve the highest strength and ductility. Thus, precipitate shape and size distribution effect on mechanical property is another area which needs a more detailed study. Lastly, current ultrafine grained aluminum alloys used are compositionally similar to conventional microcrystalline aluminum alloys. However, a better understanding of the microstructure mechanical property interrelation will facilitate newer alloy designs. Such newer designs can potentially overcome the limitations of current alloys in terms of their ductility and low cycle fatigue behavior.

VITA

Partha Sarathi De was born in Durgapur, West Bengal (India) on the March 7th 1972. He received his Bachelor of Engineering degree in Metallurgical Engineering, First Class with Distinction, from Jadavpur University, Calcutta in 1999. From 1994 to 2006 he worked in Steel Authority of India Limited as a quality control engineer at different capacities. During this period, he completed his Master of Technology degree in Materials and Metallurgical Engineering degree from Indian Institute of Technology, Kanpur in 1999. He obtained his Doctor of Philosophy degree in Metallurgical Engineering from the Missouri University of Science and Technology (Formerly University of Missouri–Rolla) in 2010.